

**MINERAL IDENTIFICATION ON MARTIAN SURFACE
USING SUPERVISED LEARNING APPROACH FROM
CRISM HYPERSPECTRAL DATA**

Thesis

Submitted in partial fulfillment of requirements for the degree of

DOCTOR OF PHILOSOPHY

BY

PRIYANKA KUMARI
(Reg. No. 187065AM004)



DEPARTMENT OF WATER RESOURCES AND OCEAN ENGINEERING

NATIONAL INSTITUTE OF TECHNOLOGY KARNATAKA

SURATHKAL - 575025

May 2024

**MINERAL IDENTIFICATION ON MARTIAN SURFACE
USING SUPERVISED LEARNING APPROACH FROM
CRISM HYPERSPECTRAL DATA**

Thesis

**Submitted in partial fulfillment of requirements for the degree of
DOCTOR OF PHILOSOPHY**

BY

**PRIYANKA KUMARI
(Reg. No. 187065AM004)**

UNDER THE GUIDANCE OF

Prof. Amba Shetty

&

Prof. Shashidhar G Koolagudi



**DEPARTMENT OF WATER RESOURCES AND OCEAN ENGINEERING
NATIONAL INSTITUTE OF TECHNOLOGY KARNATAKA
SURATHKAL - 575025**

May 2024

DECLARATION

By the Ph.D. Research Scholar

I hereby declare that the thesis entitled “**Mineral Identification on Martian Surface Using Supervised Learning Approach from CRISM Hyperspectral Data**”, which is being submitted to the **National Institute of Technology Karnataka, Surathkal**, in partial fulfillment of the requirements for the award of Degree of **Doctor of Philosophy in Department of Water Resources and Ocean Engineering** is a *bonafide report of the work* carried out by me. The material contained in this research thesis has not been submitted to any university or institution for the award of any degree.

Priyanka Kumari

187065AM004, Priyanka Kumari

(Registration Number, Name & Signature of the Research Scholar)

Department of Water Resources and Ocean Engineering

Place: NITK Surathkal

Date: May 15, 2024

CERTIFICATE

This is to certify that the research thesis entitled "Mineral Identification on Martian Surface Using Supervised Learning Approach from CRISM Hyperspectral Data" submitted by Priyanka Kumari (187065AM004) as a record of the work carried out by her, is accepted as the research thesis submission in partial fulfillment of the requirements for the award of the degree of **Doctor of Philosophy**.



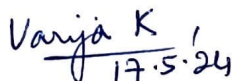
Prof. Amba Shetty
Research Guide

Department of Water Resources and Ocean Engineering
(Signature with Date and Seal)



Prof. Shashidhar G Koolagudi
Research Guide

Department of Computer Science and Engineering
(Signature with Date and Seal)



Chairman - DRPC

(Signature with Date and Seal)

Chairman (DRPC)
Dept. of Water Resources & Ocean Engineering

I dedicate this thesis

to **my husband**

Dr. Sampriti Soor

to **my parents**

Mr. B.K. Singh & Mrs. Kamla Devi

to **my sister and brother**

Ms. Pinky Kumari and Mr. Saket Kumar

to **my in-laws**

*Mr. Netra Mohan Soor, Mrs. Dipti Soor,
Mrs. Samahati Soor and Mr. Sudiptam Maity*

Acknowledgments

My thesis has become a reality with the kind support and help of many individuals. I want to express my sincere appreciation and admiration to everyone who has helped me tremendously throughout my PhD work.

I want to express my gratitude to my PhD supervisors **Prof. Amba Shetty** and **Prof. Shashidhar G Koolagudi** for the unwavering support, inspiration, and the enormously helpful discussions we had over the years. Additionally, I want to express my gratitude to **Sampriti Soor** and **Nidhi Talwar**, with whom I had many productive discussions in various stages of my doctoral work.

I express my sincere gratitude to the esteemed members of my Research Progress Appraisal Committee (RPAC), **Dr. Jeny Rajan** from the Department of Computer Science and Engineering, and **Dr. Debabrata Karmakar** from the Department of Water Resources and Ocean Engineering. Their dedicated time and meticulous examination during the proposal, first progress, second progress, and pre-synopsis seminars have been invaluable.

I wish to thank **Prof. Mahesha A**, **Prof. Amba Shetty**, **Prof. Dodamani B M**, and **Prof. Varija K**, the successive Heads of the Department of Water Resources and Ocean Engineering, NITK, for the kind support and encouragement extended by them. I would also like to thank **Dr. Subrahmanya Kundapura**, Secretary DRPC, Department of Water Resources and Ocean Engineering, NITK, Surathkal, for his support and encouragement.

I would like to express my gratitude to Director **Prof. B Ravi**, Dean Academic, Staff of Office of Dean Academics of National Institute of Technology, Karnataka for their support and permission to use the institutional infrastructure facilities. Also I thank the Ministry of Education for the funding to carry out the research work.

I consider myself very lucky to be surrounded by friends **Chinmayi Yogendra, Arya, Komal, Swathi Shetty, Deepa, Ayushi** and countless more. I want to thank you all for the enjoyable discussions on various topics related or not related to this thesis work. Because of you all, I never felt lonely in my difficult times. I will always remember the memorable moments we spent together over the past few years.

The thesis would not be possible without the contribution of each and every one of you.

Priyanka Kumari

Abstract

The availability of spectral libraries for CRISM (Compact Reconnaissance Imaging Spectrometer for Mars) data through NASA's Planetary Data System has revolutionized the study of the surface mineralogy of Mars. However, building supervised learning models for mineral mapping remains a challenge due to the scarcity of ground-truth training data. In this thesis, an innovative framework is presented that leverages supervised learning to classify spectra within CRISM hyperspectral images. To overcome the data limitation, an augmentation approach is employed that creates the training data by augmenting the minerals available in the MICA spectral library, preserving key absorption signatures of each mineral class while introducing adequate variability. The framework includes a comprehensive pre-processing pipeline, featuring a novel feature extraction method to capture distinctive absorption patterns in the spectra. The approach is validated using CRISM images from diverse Martian locations and interactive mineral maps are also provided for the detected dominant minerals. While this initial framework ensures acceptable accuracy, utilizing more sophisticated learning models and advanced preprocessing techniques can enhance the performance of the framework. Spectra in remotely sensed hyperspectral images are often affected by the presence of continuum, which changes the global curvature of the spectra, although the key absorption signatures are present. The continuum removal process, one of the critical preprocessing steps in the pipeline, is modified from the traditional approach to a novel method named Segmented Curve Fitting, which can identify more absorption shoulder points in a spectrum and thus can detect the absorption features in it more distinctively. Lastly, the thesis introduces MICANet, a specialized Deep Convolutional Neural Network (DCNN) architecture tailored for mineral identification using CRISM hyperspectral data. Inspired by Inception-V3 and InceptionResnet-V1 architectures, MICANet leverages 1-dimensional convolutions for processing spectra at the pixel level. This innovative architecture represents a significant contribution, being the first solely dedicated to this objective. The performance of the mineral mapping framework is assessed using both simulated data of varying complexity and a real CRISM TRDR/MTRDR hyperspectral dataset. In conclusion, this study advances the field of planetary science and remote sensing by providing automated approaches for mineral identification and mapping on Mars, also, enhances the understanding of Martian surface mineralogy, offering valuable insights into the planet's geological history and habitability.

Contents

Abstract

List of Figures

List of Tables

List of Acronyms

1	Introduction	1
1.1	Motivation	4
1.2	Challenges	6
1.3	Research Gap	8
1.4	Research Objective	9
1.5	Organisation of the Thesis	10
2	Essential Background	13
2.1	CRISM Data Specification	13
2.2	Atmospheric Correction for CRISM data	14
2.2.1	Volcano Scan	15
2.2.2	Discrete Ordinate Radiative Transfer (DISORT)	16
2.3	Summary Parameters and Browse Products	18
2.3.1	Summary Parameter	19
2.3.2	Browse Product	21
2.4	Spectral library	22
2.4.1	CRISM spectral library	23
2.4.2	MICA type spectral library	24
2.4.3	RELab library	24

2.5	Surface Mineralogy of Martian surface	25
2.5.1	Mafic minerals and iron oxides	26
2.5.2	Sulfates	26
2.5.3	Phyllosilicates	28
2.5.4	Hydrated silicates and halides	28
2.5.5	Ices	29
2.5.6	Carbonates	29
2.6	Geological Information of different Study areas	30
2.7	Different Supervised Learning Models	32
2.7.1	Artificial Neural Network (ANN)	32
2.7.2	Convolutional Neural Network (CNN)	33
2.7.3	Support Vector Classifier (SVC)	34
2.7.4	Random Forest Classifier (RFC)	35
2.8	Performance Measures	36
2.8.1	Precision	37
2.8.2	Recall	37
2.8.3	F-score	37
2.8.4	Accuracy	38
2.8.5	Confusion Matrix	38
2.8.6	Receiver Operating Characteristic (ROC) curve	39
3	Literature Review	41
3.1	Distance-based matching methods	43
3.2	Distribution-based unsupervised methods	43
3.3	Distance-based unsupervised methods	45
3.4	Neural networks	46
4	A Fully-Automated Framework for Mineral Identification	49
4.1	Pre-processing Pipeline	52
4.1.1	Data Augmentation	53
4.1.2	Domain Collating	55
4.1.3	Spectra Smoothing	56
4.1.4	Continuum Removal	57

4.1.5	Spectra Standardization	58
4.1.6	Absorptions Extraction	59
4.2	Performance Analysis	62
4.2.1	Experimental Setup	62
4.2.2	Uncertainty Analysis of Pre-processing Pipeline	69
4.2.3	Performance Comparison	69
4.3	Geological information of study area for mineral mapping	71
4.4	Results and Discussions	73
4.5	Chapter Summary	81
5	Segmented Curve-Fitting Method for Continuum Removal	83
5.1	Notations	89
5.2	Segmented Curve-fit for Continuum Removal	90
5.3	Performance Evaluation	95
5.3.1	Experimental Setup	96
5.3.2	Performance Analysis	106
5.4	Results and Discussion	113
5.5	Chapter Summary	115
6	MICAnet: A Deep Neural Network for Mineral Identification	117
6.1	Dataset preparation and Methodology	117
6.2	Model Architecture	119
6.2.1	Experimental Setup	123
6.2.2	Overall Architecture	125
6.3	Performance Analysis	125
6.4	Chapter Summary	127
7	Conclusion and Future Perspectives	129
7.1	Conclusion	129
7.2	Contributions of the thesis	130
7.3	Future Extension of the Research	131
	References	133

List of Figures

1.1	Representation of the data acquisition process	3
1.2	Flowchart of sequential preprocessing of CRISM data	3
1.3	CRISM image cube	3
1.4	Manual identification of mineral	5
1.5	The spectrum captured from the surfaced is a mixed spectrum	7
1.6	The difference in global curvatures between the two H ₂ O-Ice spectra	7
2.1	Volcano Scan Correction Method:processing of TRDR3 to MTRDR data	16
2.2	DISORT Model:processing of EDR to MTRDR data	17
2.3	Mola elevation map showing different location on the Martian surface	30
4.1	Mineral Spectra Available in MICA library	50
4.2	Visualization of scale and shape change in MTRDR data	51
4.3	Flowchart of the data pre-processing pipeline	52
4.4	Augmented pure spectrum with continuum and random noise	54
4.5	Smoothed spectrum is generated by Savitzky-Golay filtering	56
4.6	Visualization of the effect of continuum removal process	57
4.7	Visualization of the effect of standardization on a spectrum	58
4.8	Illustrations of band-depth, band-angle and band-area.	59
4.9	Visualization of wavelength ranges with high diversity in band-depths	60
4.10	Different augmentation parameter model's performance	64
4.11	Architecture of the CNN model used in the study	66
4.12	Architecture of the ANN model used in the study	67
4.13	Mars Orbital Laser Altimeter-MOLA elevation Map	71
4.14	False-colour images from different locations on Martian surface.	72
4.15	Classified pixels with in FRT93BE for the dominating minerals	74

4.16	Absorption matching of dominant minerals in FRT93BE	76
5.1	A comparison of absorption feature detection between SCF and UCH .	87
5.2	Visualization of Segmented Curve-Fitting process	93
5.3	Workflow of the Performance Evaluation	95
5.4	Synthesizing dataset- 1, 2 and 3 for different noise parameters	98
5.5	Preprocessing pipeline that includes SCF as the continuum removal . .	99
5.6	Band-minima and FWHM of the prominent segments in processed spectra	99
5.7	Demonstration of WSSC spectra matching method	105
5.8	The density plots of band-minima and FWHM values of different methods	111
5.9	Mineral detection in MTRDR data using WSSC with SCF	114
5.10	Spectra matching in detected minerals using WSSC with SCF	114
6.1	A preprocessed spectra with SCF as the continuum removal operation .	118
6.2	Workflow of the mineral identification process using MICAnet	118
6.3	s-Block, i-Block and r-block of MICAnet	122
6.4	The architecture of MICAnet	123
6.5	Training and validation accuracy-loss plots of MICAnet	124
6.6	Confusion Matrix and ROC curves for different mineral classes and groups	126

List of Tables

1.1	Specifications of different MRO sensors	2
2.1	Different CRISM observing modes and data products	14
2.2	Different Summary parameters for CRISM hyperspectral data	20
2.3	Different browse products of a CRISM hyperspectral data FRTC518	22
2.4	Spectral features of the dominant minerals on the Martian surface	27
2.5	Different locations on the Martian surface with the dominant minerals	31
3.1	Different methods used for mineral identification in CRISM data	42
4.1	Different parameters set in the pre-processing pipeline	63
4.2	Ablation study of the CNN Architecture	66
4.3	Ablation study of the ANN Architecture	67
4.4	Hyper-parameters for SVC and RFC models used in the experiment	68
4.5	Uncertainty Analysis of pre-processing pipeline	70
4.6	Performance comparison of proposed supervised models	70
4.7	Browse Products description of image FRT93BE	73
5.1	Band-center and FWHM scores in synthetic data	108
5.2	Mineral identification scores in synthetic data	109
5.3	Evaluation measures in data-4	109
5.4	Mineral-groupwise accuracy comparison with previously proposed models	113
6.1	Hyper-parameters and training specifications for MICAnet	124
6.2	Ablation study of the proposed architecture	124
6.3	group wise Mean Accuracy comparison	126

Acronyms

AAD Average Absolute Deviation

ACR Apparent Continuum Removal

ANN Artificial Neural Network

AUC Area-Under-the-Curve

CAT CRISM Analysis tool

CNN Convolutional Neural Network

CRISM Compact Reconnaissance Imaging Spectrometer for Mars

CTX Context Imagery

DCNN Deep Convolutional Neural Network

DEMUD Discovery via Eigenbasis Modeling of Uninteresting Data

DISORT Discrete Ordinate Radiative Transfer

DPM Dirichlet Process Mixture

EDR Experimental Data Record

FN FALSE Negative

FP FALSE Positive

FPR FALSE Positive Rate

FRT Full-Resolution Targeted

GAN Generative Adversarial Network

GH Geometric Hull

GMM Gaussian Mixture Model

HBM Hierarchical Bayesian Model

HCP High Calcium Pyroxene

HDP Hierarchical Dirichlet process

HiRISE High-Resolution Imaging Science Experiment

I2GMM Infinite Infinite Gaussian Mixture Model

ICR Imposed Continuum Removal

IGMM Infinite Gaussian Mixture Model

IR Infra-Red

LCP Low Calcium Pyroxene

LDA Linear Discriminant Analysis

MA Mean Accuracy

MARCI Mars Color Imager

MCS Mars Climate Sounder

MF Matched Filtering

MICA Minerals Identified in CRISM Analysis

MRO Mars Reconnaissance Orbiter

MSL Mars Science Laboratory

MTRDR Map-projected Targeted Reduced Data Record

NMF Non-negative Matrix Factorization

OPTICS Ordering Points To Identify Clustering Structure

PCA Principal Component Analysis

PDS Planetary Data System

PO-HDP Partially Observed Hierarchical Dirichlet process

RELab Reflectance Experiment Laboratory

ReLU Rectified Linear Unit

RFC Random Forest Classifier

ROC Receiver Operating Characteristic

SAM Spectral Angle Mapper

SHARAD Shallow Radar

SMACC Sequential Maximum Angle Convex Cone

SUH segmented Upper Hull

SVC Support Vector Classifier

TN TRUE Negative

TP TRUE Positive

TPR TRUE Positive Rate

TRDR Targeted Reduced Data Record

UCH Upper Convex Hull

VNIR Visible to Near-InfraRed

WSSC Weighted Sum of Segment Correlation

Chapter 1

Introduction

Mars, Earth's closest planetary neighbor, offers a captivating avenue for scientific exploration with far-reaching implications. Its resemblance to Earth provides a unique window into the evolution of rocky planets and the mysteries of our own planet's past. Mars acts as a natural laboratory, allowing us to delve into the fundamental geological processes that have shaped terrestrial planets. Of paramount interest is the question of extraterrestrial life, a pressing inquiry in planetary science. With its ancient river valleys and polar ice caps, Mars hints at a watery history, igniting our quest to detect signs of life beyond our home planet. By scrutinizing the Martian surface, we aim to unlock the secrets of habitability, both past and present, thus advancing our search for life elsewhere in the cosmos. Moreover, the Martian surface harbors a wealth of information within its minerals, the foundational components of planetary geology. Each mineral narrates a chapter in Mars' geological history, revealing tales of volcanic eruptions, impact events, and the presence of water. These revelations not only deepen our comprehension of Mars but also significantly contribute to the broader realm of planetary science.

The Mars Reconnaissance Orbiter (MRO) was launched on August 12, 2005 following the loss of two previous Martian missions, the Mars Climate Orbiter (1998) and Mars Polar Lander (1999). During its Primary Science Phase operation, which spanned from November 2006 to October 2010, MRO aimed to achieve several scientific objectives, such as studying seasonal variations in the Martian atmosphere and surface, detecting evidence of historical water presence and its effects on the Martian surface, and mapping and characterizing the geology, stratigraphy, and identifying the

composition of surface deposits. MRO is equipped with several scientific instruments, including the High-Resolution Imaging Science Experiment (HiRISE), Mars Color Imager (MARCI), Context Imagery (CTX), Mars Climate Sounder (MCS), and Shallow Radar (SHARAD). Different specifications of these sensors are presented in Table-1.1. These instruments are specifically designed to study different aspects of Mars, such as its geology, atmosphere, surface, climate, and the possibility of habitability.

The HiRISE instrument McEwen et al. (2007) on MRO is capable of capturing high-resolution images of the Martian surface with a resolution of up to 60 centimeters per pixel. This exceptional level of detail enables scientists to closely examine diverse surface characteristics like sand dunes, craters, and gullies, facilitating the identification of potential landing sites for upcoming missions. On the other hand MARCI and CTX Malin et al. (2007) gives information about regional stratigraphy and morphology, the MCS McCleese et al. (2007) instrument uses Infra-Red (IR) and radio occultation measurements to study the Martian atmosphere. By examining the structure and composition of the atmosphere, scientists can better understand the planet’s climate and how it has evolved over time whereas SHARAD Seu et al. (2007) instrument is a ground-penetrating radar that can detect subsurface features down to a depth of several hundred meters. MRO’s extended phase mission aims to determine the feasibility of potential future landing sites, assess Mars rover traversal, and provide a data relay service from ground missions back to Earth.

Compact Reconnaissance Imaging Spectrometer for Mars (CRISM), the seventh instrument of MRO, is a highly effective tool that has significantly advanced researchers’ understanding of the mineralogy of Mars. CRISM, equipped with enhanced spectral and spatial capabilities, has successfully obtained a multitude of consecutive images

Table 1.1: Specifications of different MRO sensors

Sensor	Spectral Range(μm)	Spatial Resolution	No. of Bands
HiRISE	0.4 -0.7	0.6 meter	1
CTX	0.5 – 0.8	6 meter	1
MCS	0.3 - 4.5	5 km	9
MARCI	0.2 - 0.8	Visible: 1-7 km UV: 10-30 km	Visible-5
SHARAD	12-20	15 meter	-
CRISM	0.3 – 3.9	18 to 200 meter	544

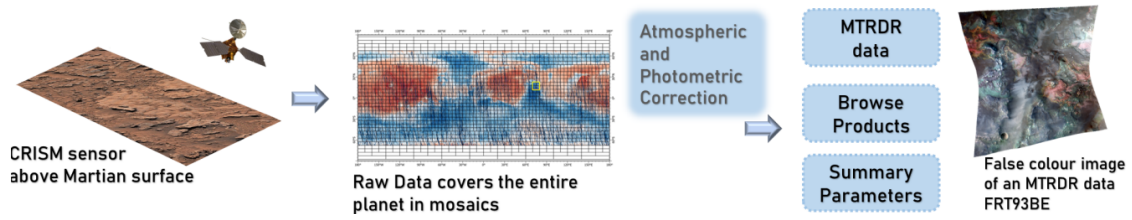


Figure 1.1: process of data collection from Martian surface to yield MTRDR data after applying preprocessing

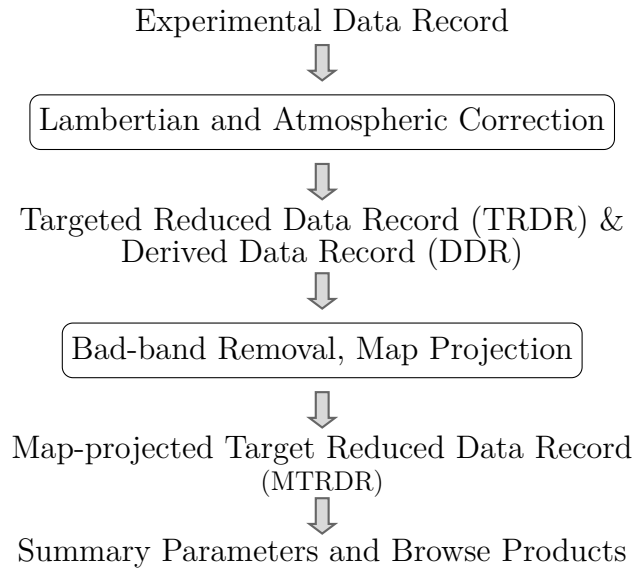


Figure 1.2: Sequential preprocessing of EDR to MTRDR of CRISM data, showing the roles of noise correction

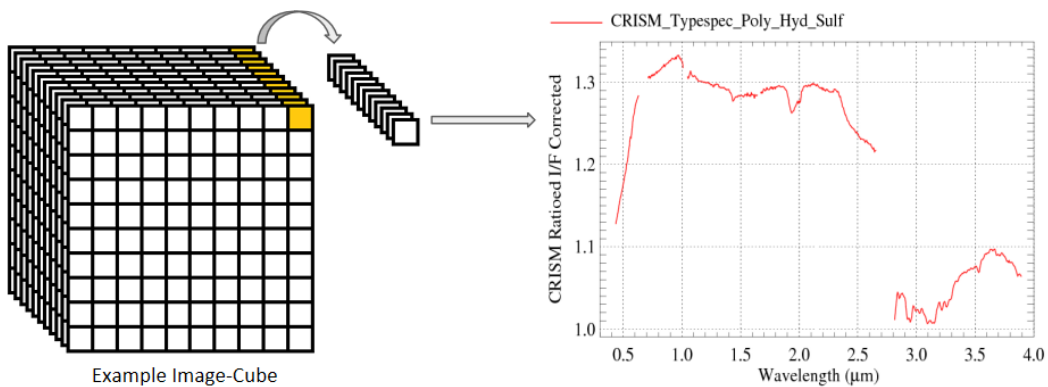


Figure 1.3: Example of CRISM image cube and a sample spectrum at the yellow marked pixel (the spectrum image is taken from NASA PDS)

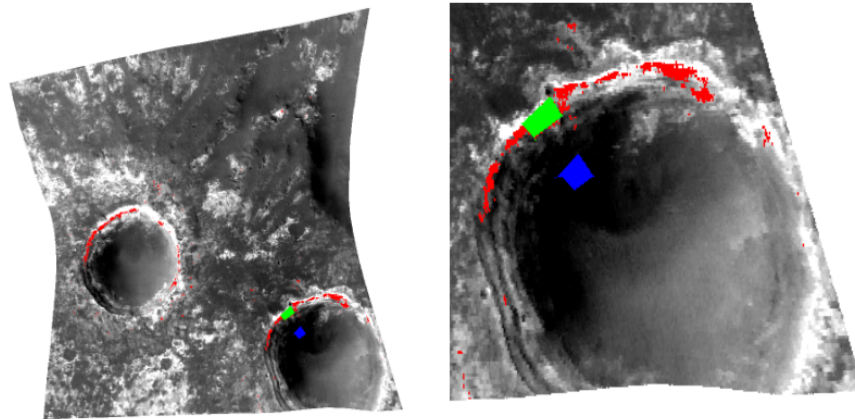
from significant Martian regions, including volcanic areas, precipitous cliffs, and sedimentary deposits. CRISM data measures electromagnetic energy of Visible to Near-InfraRed (VNIR) wavelengths in the range 0.3-3.9 micrometer with an improved spectral and spatial resolution of 18m/pixel at 300km. These hyperspectral images cover

the entire Martian planet, forming a mosaic representation (see figure 1.1). Initially, CRISM gathers raw data, storing it in an Experimental Data Record (EDR) format comprising 544 bands. These data undergo a series of corrections, as illustrated in figure 1.2, resulting in the creation of Targeted Reduced Data Record (TRDR) and Map-projected Targeted Reduced Data Record (MTRDR) data cubes, now reduced to 489 bands. Each pixel within these TRDR and MTRDR images contains rectified reflectance values, which, when plotted along the wavelength domain, reveal the spectral signatures stored within (see figure 1.3). These TRDR and MTRDR images of a scene are used for mineral identification and mapping. Additionally, from the MTRDR data, spectral summary parameters and browse products are computed, offering valuable insights for spectral analysis and visual interpretation, aiding in the characterization of the Martian surface. This comprehensive datasets has significantly expanded our knowledge of Martian geology and mineral composition.

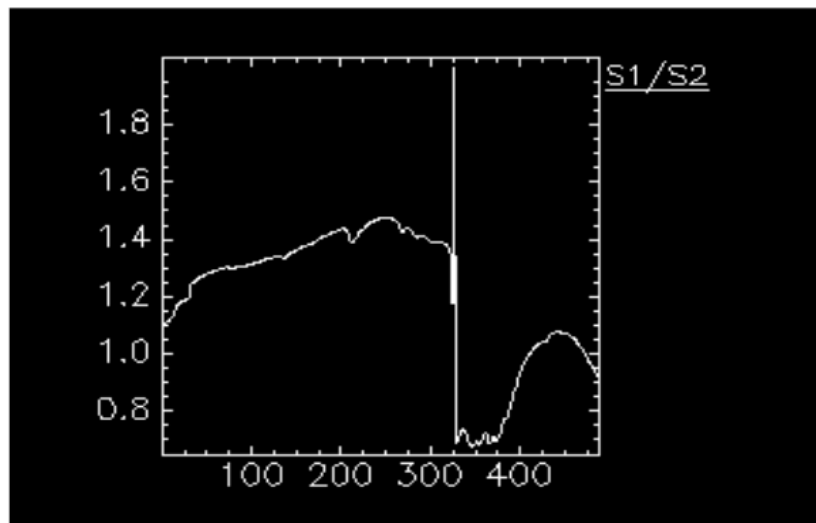
CRISM has enabled the identification and characterization of various minerals, notably, the detection of phyllosilicates including kaolinite, hydrated silica, and different types of smectites Mustard et al. (2008). This detection is of particular significance as these minerals are typically formed in the presence of liquid water. Apart from phyllosilicates, CRISM has also detected different mafic minerals, carbonates, and sulfates Wendt et al. (2011); Skok et al. (2012); Ehlmann et al. (2014). The identification and mapping of these minerals provide valuable insights into Mars' past climate and geologic history, also the geologic processes that have shaped the Martian surface and the evolution of the planet's atmosphere and climate.

1.1 Motivation

In the early days of mineral identification and mapping, the task was carried out manually by experts. The process involved utilizing summary parameter images to identify various minerals. Initially, specific pixels were selected from the image based on their summary parameter values falling within a predefined range referred to as the "stretch limit." It's important to note that this stretch limit could vary not only for different minerals but even for the same mineral in different image scenes. To illustrate, consider Figure 1.4, where we aimed to identify poly-hydrated sulfate minerals in the



*green=numerator(s1) *blue=denominator(s2)



(S1/S2) average spectra

Figure 1.4: Process of Manual identification of Mineral polyhydrated sulphate using Summary Parameter(BD1900) and validation with Spectral library

MTRDR image FRT13D4F, taken from the Jejero crater region on Mars. In this case, a summary parameter named BD1900 was employed, and by setting a stretch limit of 0.03-0.05, the pixels highlighted in red were identified as potentially containing this specific mineral. However, further verification was required to confirm these pixels as the desired mineral. To achieve this confirmation, a region of interest (ROI) was chosen from the selected pixels and marked in green (termed as S1). Simultaneously, another region, preferably with flat reflectance values, was selected either from the same or nearby line-sample and labeled as S2, marked in blue within the image. Subsequently, the mean spectra of these two selected regions were ratioed to enhance the spectral features of the region of interest. This enhanced spectrum was then compared with the spectrum of the poly-hydrated sulfate mineral from a spectral library such as Minerals

Identified in CRISM Analysis (MICA).

However, it's important to acknowledge that this manual process was cumbersome, time-consuming, and heavily reliant on experts' involvement. To streamline and automate this procedure, several distance-based matching approaches and both distance-based and distribution-based unsupervised methods have been explored in the literature, some of which will be discussed in Chapter 3. While these methods have made significant strides, they still have limitations in terms of performance and automation compared to what supervised learning models achieved in the last decade in different other objectives. In the realm of mineral identification, even though a handful of researchers have ventured into applying supervised learning models to CRISM data, achieving full automation in the mineral identification process has proven to be a challenging endeavor. This served as the impetus for my doctoral research, where I dedicated my efforts to developing a comprehensive automated framework tailored for mineral identification on the Martian surface.

1.2 Challenges

The complexity of CRISM hyperspectral data poses several intricate challenges in data processing and analysis, such as,

- **Presence of bad bands:** CRISM data often contains problematic bands caused by factors like atmospheric interference, sensor noise, detector issues, or data transmission errors. Detecting and removing these bad bands is crucial for accurate analysis.
- **Domain and Scale Inconsistency:** Variability in atmospheric conditions, mineral compositions, and other factors leads to inconsistencies in the data's domain and scale. Different minerals in the MICA spectral library also have spectra of various wavelength ranges, for example, 430 bands for gypsum and 480 bands for bassanite. To address this, interpolation techniques are applied to mitigate domain inconsistencies. Standardization or normalization is used to bring the data to a uniform scale for effective comparison and analysis.

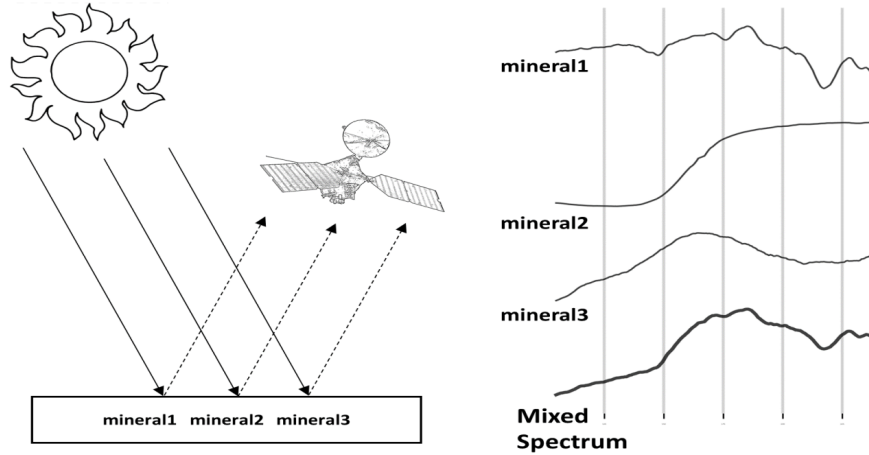


Figure 1.5: The diagram depicts a surface (a pixel in hyperspectral data) containing three different minerals having distinct spectra. The spectrum captured from the surfaced is a mixed spectrum containing individual absorptions of those minerals.

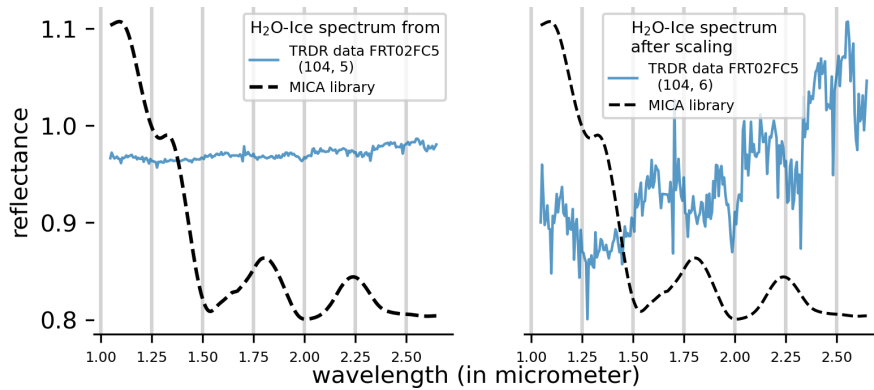


Figure 1.6: The difference in global curvatures between the two H₂O-Ice spectra in the left image is evident after the scaling operation in the right image.

- **Residual Fluctuations:** Even after applying atmospheric and photometric corrections, residual fluctuation noise in the form of spikes or small kinks can persist in spectra. These artifacts can obscure significant features and introduce errors. Researchers have employed various smoothing techniques, such as window-median filtering and Savitzky–Golay filtering, to mitigate these disturbances Carter et al. (2013b); Pelkey et al. (2007); Kumari et al. (2023a).
- **Mixed Spectra:** CRISM’s spatial resolution can vary widely, between 18-200 meters per pixel depending on the mode of operation, causing scenes to consist of mixtures of different minerals, rocks, and soils. Each object in the scene has its unique spectral signature, but hyperspectral imaging combines these signatures, resulting in spectral mixing (figure 1.5 provides a pictorial representation). This makes it challenging to detect individual endmembers. Spectral unmixing

techniques are employed to extract individual spectra and fractional abundances of materials within each pixel.

- **Presence of continuum** : Mixed spectra exhibit a smooth baseline shape known as a continuum, which masks individual spectral features. Continuums can also arise from instrument artifacts and topographic illumination effects, altering the global curvature of the target spectrum. Figure 1.6 shows the changes in the global shape in a spectrum although the absorption signatures are intact, which is more evidently visible after performing the scaling operation. Eliminating the continuum is essential to accurately identify distinctive absorption characteristics, facilitating precise material identification. The continuum removal process effectively eliminates global shape distortions, addressing both curvature issues and scaling disparities.

These challenges underscore the complexity of CRISM data processing and the need for advanced techniques to extract meaningful information for mineral identification on Martian surfaces.

1.3 Research Gap

In the domain of mineral identification using CRISM data, a noticeable research gap has emerged - the absence of a dedicated automated framework for mineral identification. The development of such a framework, particularly one employing supervised learning models, has been significantly impeded by the unavailability of essential ground-truth or training data, an issue specific to CRISM data analysis. The manual creation of ground-truth or training data is a labor-intensive and time-consuming process, often requiring expert knowledge of mineral spectral signatures.

Moreover, CRISM data, even after undergoing meticulous atmospheric and photometric corrections, still exhibits residual noise. This noise, as discussed previously, poses a substantial challenge to accurate mineral identification. While various studies have explored distinct preprocessing techniques for CRISM data, there is a critical lack of a comprehensive, well-documented preprocessing pipeline designed explicitly for the mineral identification objective. Such a unified preprocessing framework is pivotal for enabling the development of an automated mineral identification system.

Furthermore, the envisioned automated framework should demonstrate robustness and consistency in delivering accurate results when applied to CRISM data collected from diverse Martian surface locations. The environmental and instrumental variations inherent to different Martian regions can significantly influence or obscure the spectral information contained in the data. Thus, it is imperative that this research gap be addressed to construct an automated mineral identification framework that not only copes with the various issues of the CRISM data and also ensures reliable performance on the CRISM images collected across different locations of the Martian surface.

1.4 Research Objective

The primary objective of this research is to bridge the existing research gap in the domain of mineral identification using CRISM data by developing a robust and automated framework. This framework will leverage supervised learning models to enhance the accuracy and efficiency of mineral identification processes. To achieve this overarching goal, the following specific research objectives are pursued:

- i. An automated framework, that includes a supervised learning model, is developed that achieves acceptable robustness and consistency. To address the scarcity of ground-truth or training data, a new augmentation approach is proposed using the mineral spectra from the MICA spectral library. The augmentation process ensures that key absorption features for each mineral class are present while introducing adequate variability to mirror the noise found in real data. The resulting training dataset undergoes a comprehensive preprocessing pipeline tailored explicitly for the unique requirements of mineral classification in CRISM data, to mitigate the impact of residual noise and enhance data quality for subsequent phases. The same preprocessing pipeline is applied to real data during testing to ensure consistency.

The proposed framework is designed to ensure adaptability to CRISM data captured from different Martian surface locations, accounting for variations induced by environmental and instrumental factors. This adaptability will be achieved through robust feature extraction techniques that capture the distinctive spectral signatures of minerals despite variations in data characteristics. While the initial

framework ensures acceptable accuracy, the potential for further improvement is explored. This includes the investigation of more sophisticated supervised learning models and advanced preprocessing techniques.

- ii. Continuum in remotely sensed hyperspectral images can alter the overall shape of spectra, even though the primary absorption features remain intact. The continuum removal process, one of the critical preprocessing steps, is modified from the traditional approach to a novel method named Segmented Curve Fitting. This innovative approach aims to capture separate spectral information more distinctly.
- iii. A deep learning model named MICANet is proposed to further enhance the performance. The architecture of MICANet is inspired by Inception-V3 and InceptionResnet-V1 architectures, but leverages 1-dimensional convolutions for processing spectra at the pixel level.

1.5 Organisation of the Thesis

The thesis is organised as follows:

Chapter 2: This chapter provides a foundation of this thesis highlighting several key concepts including CRISM data preprocessing, MICA library minerals, geological context, supervised learning models, and different evaluation metrics used for performance analysis in the following chapters.

Chapter 3: This chapter presents comprehensive literature reviews on distance-based matching methods, distribution-based and distance-based unsupervised methods, as well as the neural networks-based approaches previously used for mineral identification on the Martian surface.

Chapter 4: This chapter develops an automated framework for mineral identification on the Martian surface using supervised learning models. It includes a new data augmentation procedure to create the training data needed to build the supervised learning model, and a novel feature extraction method, along with a preprocessing pipeline to completely automate the process of mineral mapping.

Chapter 5: Here, a new continuum removal method, Segmented Curve-Fitting, is proposed for hyperspectral data. This method enhances the accuracy of material

identification by precisely determining distinct absorption signatures.

Chapter 6: This chapter introduces the MICAnet, a Deep 1-D Convolutional Neural Network, to boost mineral identification performance.

Chapter 7: The final chapter summarizes the main findings, draws conclusions, discusses limitations, and outlines future research directions.

Chapter 4, 5 and 6 constitute the core contributions of this thesis.

Chapter 2

Essential Background

This chapter serves as the cornerstone of this thesis, laying the essential groundwork for the subsequent chapters. Here, we delve into fundamental concepts that are pivotal for understanding and contextualizing the research conducted in this work. We commence by elucidating the noise-correction of CRISM data, a critical step in preparing the raw data to usable for mineral identification. Understanding this process is vital as it significantly influences the quality and reliability of our analysis. Next, we introduce the MICA library minerals, which form the basis for our supervised learning model. These minerals possess distinctive spectral signatures that are key to identifying and characterizing Martian surface materials. Furthermore, we explore the geological context of our study areas on Mars. Understanding the geological features and formations provides critical insights into the diversity of minerals present on the Martian surface. In this chapter, we also introduce different supervised learning models that play a central role in our mineral identification framework. These models are essential tools in automating the process and enhancing accuracy. Lastly, we discuss the various evaluation metrics employed to assess the performance of our models, ensuring that our results are both reliable and meaningful.

2.1 CRISM Data Specification

The CRISM mission to Mars in 2006 was the seventh successful operation to Mars orbiting at an altitude of 300 km in a sun-synchronous near-polar orbit. The CRISM instrument detects visible near-infrared (VNIR) wavelength by the 'S' detector in

Table 2.1: Characteristics of different CRISM observing Modes and their Data Products

Observing modes	Observation & Mapping type	Resolution	Coverage and description
Targeted (Hyperspectral) (positioned at Gimbale)	Full Resolution Targeted (FRT)	<ul style="list-style-type: none"> Spatial Resolution: 18 m/pixel @ 300 km No. of bands: 544 	<ul style="list-style-type: none"> 6500 per Mars year FRT is high-priority targeted data whereas HRL and HRS have limited data volume.
	Half Resolution Short-targeted (HRS) & Half Resolution Long-targeted (HRL)	<ul style="list-style-type: none"> Spatial Resolution: 36 m/pixel @ 300 km No. of bands: 544 	
	Emission Phase Function (EPF)	<ul style="list-style-type: none"> Spatial Resolution: 200 m/pixel @ 300 km No. of bands: 544 	
Atmospheric (positioned both at Gimbale and Nadir)	Tracking Optical Depth (TOD)	<ul style="list-style-type: none"> Spatial Resolution: 200×900 m/pixel @ 300 km No. of bands: 544 	<ul style="list-style-type: none"> 2 orbits in every 2 months Free-standing for atmospheric monitoring.
	Multi-Spectral Survey (MSS)	<ul style="list-style-type: none"> Spatial Resolution: 200 m/pixel @ 300 km No. of bands: >72 	
Multispectral (Positioned at Nadir)	Multi-Spectral Windows (MSW)	<ul style="list-style-type: none"> Spatial Resolution: 100 m/pixel @ 300 km No. of bands: 72 	<ul style="list-style-type: none"> 80 percent of Martian surface MSP has long strips for global mapping

the range 364-1055 nanometers, while infrared (IR) wavelength is detected by the 'L' detector in the range 1.1-3.9 micrometers with a sampling of 6.55 nanometers per channel. The mission consisted of two phases: the Multispectral mode and the Targeted mode. In the Multispectral mode, global mineral characterization was carried out with 72 selected channels operating at a resolution of 100-200 meters per pixel, while the gimbal was positioned at the nadir. The data were collected at a frequency of 15-20Hz. This mode was crucial in confirming the presence of hydrous movement on the Mars surface, which was difficult to detect with prior Mars-orbiting spectrometers due to their low spatial and spectral resolution. The Targeted mode, with its superior spatial resolution of 18-20 meters per pixel across 544 bands, covered a wide swath width of 9.5-12 kilometers. This heightened spatial and spectral resolution offered an enhanced capability for in-depth analysis and comprehensive characterization of the Martian surface, surpassing what was achievable with the Multispectral mode. The detailed description of CRISM data for different observing modes is shown in Table-2.1.

2.2 Atmospheric Correction for CRISM data

In this section, the significance of pre-processing CRISM hyperspectral data to enhance the quality and efficiency of mineral mapping is explored. Here the use of two techniques - volcanic scan correction and the DISORT model - is emphasized to eliminate dominant atmospheric gas contributions in the near-infrared spectra. By employing these techniques, the MRO mission is able to attain accurate characterization of sea-

sonal fluctuations in suspended dust particles and icy aerosols. Additionally, these methods provide supplementary data concerning the Martian atmosphere, contributing to a more comprehensive understanding of its properties.

2.2.1 Volcano Scan

Volcano Scan is an empirical correction method that is designed to remove CO₂ absorption in the near-infrared range of spectrum 1-2.6 micrometer. This method is based on previously derived transmission spectra and is applied empirically to remove the absorption of atmospheric gas. Low and high-altitude spectra taken over Olympus Mons are used to obtain the necessary spectra, and the Beer-Lambert Law is utilized to calculate the transmission spectra Wiseman et al. (2016). The images are generally processed for reflectance using the CRISM Analysis tool (CAT) McGuire et al. (2009).

The initial step is to transform the spectral radiance observed by the sensor, which is measured in units of watts per square meter per steradian per micrometer, to I/F, which is the ratio of the radiance detected by the sensor to the solar irradiance, divided by π . This converted data is then stored in the Experimental Data Record (EDR). Following this, the Photometric Lambertian correction is carried out to modify the bidirectional reflectance characteristics of the Lambertian surface and convert the data to a standard illumination geometry resulting in Lambert albedo. The Ratio Shift Correction is then performed to evaluate the systematic cross-track residual structure, which is a ground plane along-track striping, and creates a correction frame based on inter-column ratio statistics supported cross-track structure. Then, the Empirical Geometric Normalization is conducted to characterize and correct the geometric dependencies that arise from the continually changing geometry of CRISM targeted observations wavelength-dependent along-track gradients. Finally, the Empirical Smile Correction is performed to characterize and correct a radiometric residual related to a spectral smile, an instrument optical artifact, and wavelength-dependent asymmetric cross-track gradients. Figure 2.1 illustrates the process.

Once all the corrections are applied, the resulting value is stored in a Targeted Reduced Data Record (TRDR), which contains important information such as latitude, longitude, incidence angle, emission angle, and phase angle. This information is used for map projection and post-processing corrections. A summary product is

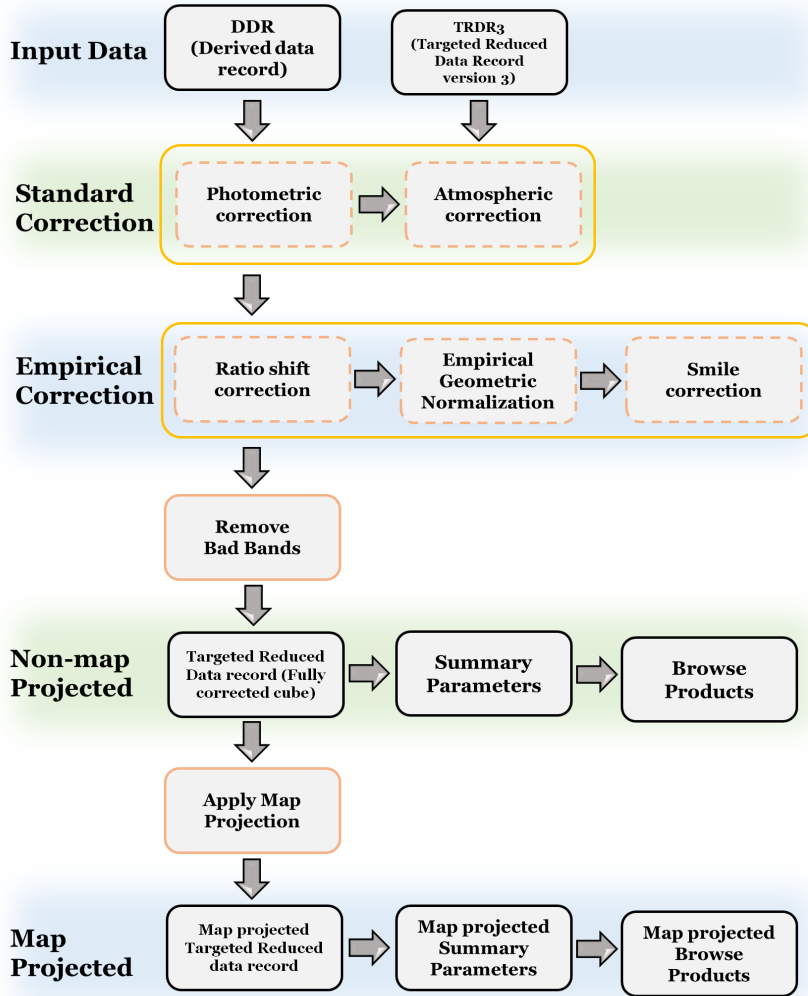


Figure 2.1: Volcano Scan Correction Method: Sequential processing of TRDR3 data along with DDR to yield MTRDR data

then calculated, and a browse product is created. Finally, after the map projection and pre-processing steps, spectral indices are derived and the MTRDR (Map-projected Targeted Reduced Data Record) is obtained. How these summary products are used for mineral identification is provided in a later section.

2.2.2 Discrete Ordinate Radiative Transfer (DISORT)

DISORT is a powerful radiative transfer model widely utilized to replicate the propagation of light through a scattering medium like a planetary surface or atmosphere. It finds extensive usage in remote sensing applications to simulate the interaction of light with planetary atmospheres and surfaces. In the context of CRISM data, DISORT can be employed to mimic the radiative transfer of sunlight through the Martian

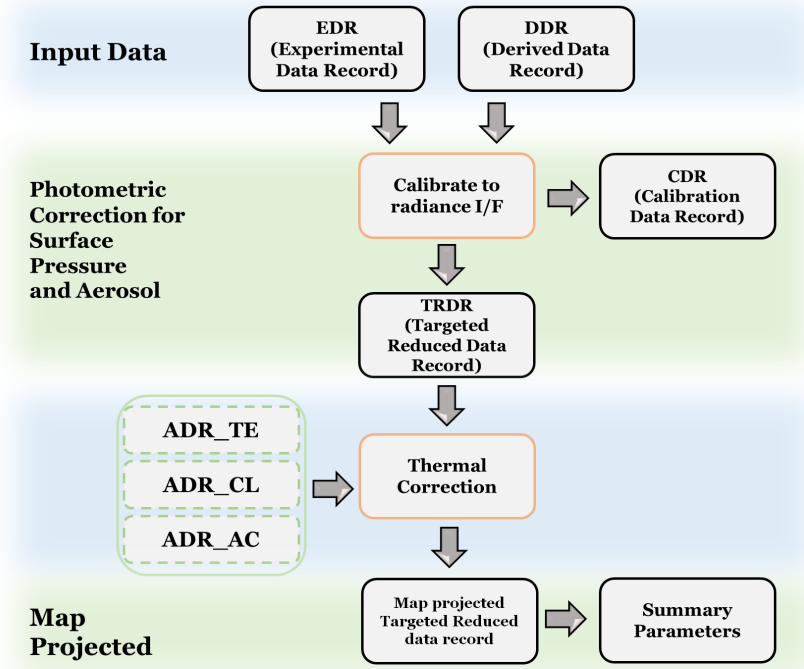


Figure 2.2: DISORT Model: Sequential processing of EDR data along with DDR to yield MTRDR data

atmosphere and its reflection and scattering by the surface features. By comparing the simulated outcomes with the actual CRISM data, vital information regarding the composition and structure of the Martian surface can be deduced.

The DISORT model is a complex process that requires multiple inputs and steps to correct atmospheric effects. These steps include photometric, atmospheric, and thermal corrections, as well as the retrieval of various parameters from lookup tables. Figure 4 shows the different lookup tables used in the model. The photometric step begins by calibrating the raw data in EDR format to TRDR, considering various viewing and incidence angles. Next, using the latitude, longitude, topography, and apparent solar time associated with a specific pixel retrieved from the appropriate DDR, the column abundances of atmospheric elements and aerosols are procured from a lookup table called *ADR_CL*. In addition, the model obtains information regarding surface slope azimuth and magnitude, thermal inertia, dust, and ice aerosol capacities, as well as surface temperature for each pixel location. Subsequently, the values for each I/F (reflectance) at every wavelength in the scene are obtained from corresponding pixel locations in the DDR and ADR. To account for any necessary corrections, a pre-computed multiplicative correction retrieved from the lookup table *ADR_AC* is

applied. The ultimate output of the DISORT model is the calculation of surface I/F, representing the theoretical Lambert albedo under ideal conditions with normal illumination and viewing geometry, disregarding atmospheric effects and thermal emission.

limitations: Both Volcano Scan and DISORT are commonly used methods for correcting and analyzing CRISM data, however, they do have certain limitations.

- i. The Volcano Scan correction method is specifically designed for volcanic regions, and may not be applicable to non-volcanic regions. Similarly, DISORT may not be suitable for all types of surface materials or atmospheric conditions.
- ii. Both methods require significant computational resources and time to process large amounts of data. This can limit their use for large-scale analysis or real-time applications.
- iii. Both methods rely on certain assumptions about the surface and atmospheric properties of Mars and may have uncertainties in their results. For example, the Volcano Scan correction method assumes a specific scattering phase function for the surface, which may not be accurate in all cases.
- iv. Both methods require accurate calibration and validation of the CRISM data, which can be challenging and may introduce errors in the analysis. Overall, while Volcano Scan correction and DISORT are useful tools for analyzing CRISM data, they should be used with caution and in conjunction with other methods to ensure accurate and reliable results.

2.3 Summary Parameters and Browse Products

This section presents a concise overview of the products that result from the atmospheric correction process, namely the summary parameters and browse products. These products play a crucial role in the interpretation of spectral data from Mars. Summary parameters represent a single parameter value that captures the spectral properties of specific mineralogy. These values are derived using different formulas applied to combinations of spectral bands, designed by the field experts Murchie et al. (2007). A summary parameter or combination of those captures the spectral properties

particular to a given mineralogy. Another important product of the atmospheric correction process is the CRISM browse product, which is a combination of thematically related summary parameters to form different false-colour images. This product shows spectral variation associated with different mineral groups, such as ice, phyllosilicates, mafics, sulfates, carbonates, and hydrated silica groups of minerals in distinguishable colours. This product is useful for identifying minerals on the Martian surface visually. The optimal implementation of these parameters is critical for accurate interpretation of the data.

2.3.1 Summary Parameter

Initially, 44 summary parameters were given in Pelkey et al. (2007) by Pelkey et al. based on multispectral images which was later on updated in Viviano et al. (2014a) by Viviano et al. with 60 summary parameters based on the hyperspectral images. Viviano et al. used these summary parameters to study the mineralogy and geology of several regions on Mars, including the Nili Fossae area and the Medusae Fossae Formation. These are derived from the following measures which are calculated from reflectances in key wavelengths.

- **Band-Depth ratio** measures the relative depth of two absorption features in the spectrum of a given region. The two features used in Viviano et al. (2014a) are associated with iron- and magnesium-rich phyllosilicates, which are indicators of aqueous alteration on Mars.
- **Spectral slope** measures the rate of change of reflectance or radiance with a wavelength in the visible and near-infrared parts of the spectrum. Spectral slope can be used to infer the composition and grain size of surface materials.
- **Integrated band area** measures the area under an absorption feature in the spectrum of a given region. The absorption feature used in Viviano et al. (2014a) is associated with olivine, a mineral that is common in basaltic rocks on Mars.
- **Band center position** measures the location of the center of an absorption feature in the spectrum of a given pre-computed absorption feature used in Viviano et al. (2014a) and is associated with pyroxene, a mineral that is also common in basaltic rocks on Mars.

Table 2.2: Different Summary parameters for CRISM hyperspectral data

Parameter name	Examples	Standard formula
Reflectance (R)	R440 (0.44 μm reflectance), R530 (0.53 μm reflectance), R600 (0.60 μm reflectance)	based on absorption at particular reflectance
Band ratio (BR)	RBR(for reflectances at 0.7 and 0.4 μm), IRR1(for reflectances at 0.8 and 1.2 μm), IRR2(for reflectances at 2.5 and 2.2 μm), IRR3(for reflectances at 3.7 and 3.5 μm)	$\frac{R_{c_1}}{R_{c_2}}$ where R_{c_1} is the reflectance for Band 1 R_{c_2} is the reflectance for Band 2
Spectral slope	SLOPE1 (Spectral slope 1)	$\frac{R_{c_1} - R_{c_2}}{\lambda_{c_1} - \lambda_{c_2}}$
Spectral Variance	VAR (1.0-2.3 μm) variance in spectra	variance in the fitted curve between 1 to 2.3 μm
Band Depth (BD)	BD2165 (2.16 μm) Band depth due to Al-OH, BD2190 (2.19 μm),Band depth due to Al-OH BD2100 (2.10 μm) band-depth due to shift in shifted H ₂ O	$BD(\lambda_c) = 1 - \frac{R_c}{R_c^*} = (1 - \frac{R_c}{aR_s + bR_t})$ where R_c = Reflectance at the center wavelength λ_c $R_c^* = (a * R_s + b * R_t)$, is derived from the continuum fit across the band $b = \frac{(\lambda_c - \lambda_s)}{(\lambda_t - \lambda_s)}$, $a = 1 - b$
Inverse Band Depth (BH)	SH600 (0.6 μm), SH770 (0.77 μm), where SH is the Shoulder point.	$BH(\lambda_c) = 1 - \frac{R_c^*}{R_c} = (1 - \frac{aR_s + bR_t}{R_c})$ Note: two defining absorption features of ferric oxides overlap in the characteristic spectrum
Doublet Parameter	DOUB2200 (0.16 and 2.21 μm band depth - doublet), MIN2345_2537 and MIN2295_2480 (due to Fe/Mg Carbonate overtone and band-depth in metal-OH)	$GEOM(\lambda_{c_1}, \lambda_{c_2}) = \sqrt{(BD(\lambda_{c_1}) * BD(\lambda_{c_2}))}$ $MIN(\lambda_{c_1}, \lambda_{c_2}) = MIN[BD(\lambda_{c_1}), BD(\lambda_{c_2})]$ where GEOM and MIN is geometric mean and Minimum of two band depth.
Broad Band	OLINDEX2, HCPINDEX2	combining multiple band depth $INDEX(\lambda_{c_1}, \lambda_{c_2}, \dots, \lambda_{c_n}) = D_1(BD(\lambda_{c_1})) + D_2(BD(\lambda_{c_2})) + \dots + D_n(BD(\lambda_{c_n}))$

These summary parameters provide valuable information about the elements and physical properties of the Martian region and also are vastly used for mineral identification. Table-2.3 presents some of these summary parameters along with their standard formulas.

limitation in mineral identification: The use of summary parameters for identifying minerals on the Martian surface using has several limitations, such as,

- **Spectral Variability:** The spectral response of minerals can vary significantly depending on factors such as grain size, composition, and hydration state. Therefore, summary parameters that rely on a single spectral measurement may not be able to distinguish between different mineral species.
- **Surface Mixtures:** The Martian surface can contain mixtures of different minerals, making it difficult to identify individual species. In some cases, summary parameters may not be able to differentiate between mixtures of similar minerals.
- **Instrument Noise:** CRISM data can contain noise and artifacts that can affect the accuracy of summary parameters. This can lead to false positives or negatives in

mineral identification.

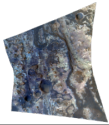
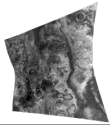
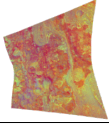
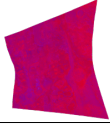
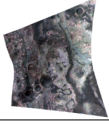


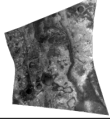
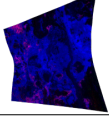
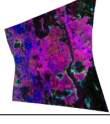
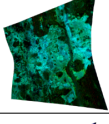
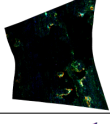
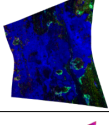
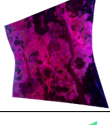
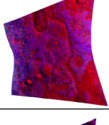
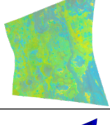
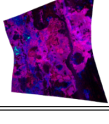
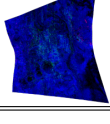
- **Spatial Resolution:** The spatial resolution of CRISM data is limited, which can make it difficult to identify minerals in small or complex geological features.
- **Lack of Ground Truth:** The identification of minerals using summary parameters is often based on spectral libraries and models, which may not accurately represent the Martian surface. In addition, there is limited ground truth data available for mineral identification on Mars, which can make it challenging to validate the results.

In summary, the use of summary parameters for identifying minerals on the Martian surface using CRISM data has several limitations, and these should be taken into account when interpreting the results.

2.3.2 Browse Product

A Browse Product is created by combining three summary product composites, resulting in a false-color image that allows for visual identification of minerals and analysis of their distribution map. The PFM and PAL browse products, in particular, exhibit enhanced sensitivity to such variations. The PFM product utilizes RGB composites of BD2355, D2300, and BD2290 to provide insights into Fe/Mg-phyllsilicates. In this composite, the existence of prehnite or chlorite is represented by red and yellow colors, while cyan colors generally show the existence of Fe/Mg smectites. On the other hand, the PHY product, with RGB composites of D2300, D2200, and BD1900r2, portrays all Fe/Mg-phyllsilicates as inseparable red or magenta given that possess similar hydration bands. The PAL product, with RGB composites of BD2210_2, BD2190, and BD2165, offers insights specifically related to Al-OH materials. In this composite, Al smectites are depicted as cyan, while kaolinites appear light or white in color. Similarly, the PHY product represents all Al-OH segments as indistinguishable green or cyan if they possess comparable hydration bands. Additionally, the HYS product, utilizing RGB composites of MIN2250, BD2250, and BD1900r2, further identifies Si/Al-hydroxylated minerals. In this composite, hydrated silica is depicted as light red or yellow, while Al-OH minerals are represented as cyan. To accommodate variations in summary product values across scenes, each summary product is individually

Table 2.3: Different browse products of a CRISM hyperspectral data FRTC518

Name, RGB Channels	Significance	Example Browse Product	Name, RGB Channels	Significance	Example Browse Product
True colour (TRU) R600, R530, R440	Enhanced CRISM I/F image after atmospheric and photometric correction applied.		VNIR albedo (VNA) R770, R770, R770	Photometric corrected CRISM I/F image at 770nm, used for correlation between spectra and mineralogy.	
Ferrous mineral (FEM) BD530.2, SH600.2, BDI1000VIS	Red: ferric oxides Green: textural effects Blue: mafic minerals		Ferrous mineral second version (FM2) BD530.2, BD920.2, BDI1000VIS	Red: ferric oxides Green: coarser-grained Fe minerals Blue: mafic minerals	
False colour (FAL) R2529, R1506, R1080	False colour CRISM I/F image.		"IR albedo (IRA) R1300, R1300, R1300	Photometrically corrected CRISM I/F image at wavelength 1330nm.	
Tandem (TAN) R2529, IRA, R770	Red: Olivine-Rich mineral. Green: mostly shows clay. Gray / Brown: Basaltic minerals.		Mafic mineral (MAF) OLIINDEX3, LCPINDEX2, HCPINDEX2.	Red: olivine and Fe-phyllsilicates. Green/Cyan: HCP Blue/Magenta: LCP.	
Hydrated mineral (HYD) SINDEX2, BD2100.2, BD1900.2.	Red/Magenta: polyhydrated sulfate Green/yellow: monohydrated sulfate Blue: clay,carbonate and zeolite		Phyllosilicates (PHY) D2300, D2200, BD1900r2.	Red/Magenta: hydrated phyllosilicates Green/cyan: hydrated silica Blue: Sulfates, carbonate, hydrated silica	
Phyllosilicates with Fe and Mg (PFM) BD2355, D2300, BD2290	Red/yellow: prehnite, chlorite, Ca/Fe carbonate cyan: Fe/Mg smectites, Mg carbonate.		phyllosilicates with Al (PAL) BD2210.2, BD2190, BD2165.	Red/yellow: smectites or hydrated silica green/cyan: alumite light-white: kaolinite	
hydrated silica (HYS) MIN2250, BD2250, BD1900r2	Red/yellow: hydrated silica, jarosite cyan: Al-OH minerals Blue: hydrated minerals		ices (ICE) BD1900.2, BD1500.2, BD1435	Red: sulfates, clays Green: water-ice Blue: ice	
ices second version (ICE 2) R3920, BD1500.2, BD1435	Red: ice free surfaces Blue: ice frost.		Chloride (CHL) ISLOPE, BD3000, IRR2	Red: chloride deposits Green: hydrated mineral. Blue: ice frost.	
Carbonates (CAR) D2300, BD2500H2, BD1900.2	Red/Magenta: Fe/Mg-phyllsilicates yellowish-white: Mg carbonates Blue: hydrated minerals.		Carbonate second version (CR2) MIN2295.2480, MIN2345.2537, CINDEX2	Red/Magenta: Mg carbonates Green/cyan: Fe/Ca carbonates	

stretched and converted into an 8-bit RGB channel composition for the browse product. Table 2.3.2 lists some commonly used browse products, their RGB composites, and associated colour meanings of a CRISM hyperspectral data FRTC518 from the Gale Crater Region.

2.4 Spectral library

In remote sensing, a spectra consists of measurements of how much light is absorbed or reflected at different wavelengths by a particular material. A spectral library is

a collection of spectra built as a reference database by experts for different types of materials such as vegetation, soil, water, minerals, and man-made features like roads and buildings. For the minerals on the Martian surface many spectral libraries is created by compiling spectrum data from common materials for almost 50 years and made available easily by research organizations for the Martian surface which most widely used such as CRISM spectral library Murchie et al. (2007), MICA type spectral library Viviano et al. (2014a) and RELAB library Carlé M. Pieters¹ (2004). These spectral libraries are important resources for planetary scientists studying Mars. These enable remote sensing analysts to identify the observed materials in the image by comparing the spectral signature of the materials to known spectral signatures in the library, and map their distribution and abundance. Additionally, these libraries guide mission planning by identifying areas of interest, aid in understanding the Martian environment by studying the distribution of water and ice, and help develop new analytical techniques for planetary surface study. By analyzing the spectral data in these libraries, scientists can gain new insights and make new discoveries about the Red Planet.

2.4.1 CRISM spectral library

NASA has built a Planetary data science system(PDS) by incorporating spectra from the CRISM spectrum library as well as from other sensors. The CRISM spectral library is a significant resource for studying the mineralogy and composition of Mars, and it has numerous important applications in planetary science. This library released on March 10, 2006, is the first ground truth library to allow the interpretation and analysis of minerals on the Planetary surface. There are currently 2260 spectrum analyses altogether collected from Mars, Moon, and Earth surface, consisting of 1134 natural and artificial Mars samples in the CRISM spectral library, which is organized in a hierarchical framework. All of the spectra in this library are samples with the same spectral resolution of CRISM data and were interpolated using linear interpolation to remove the atmospheric obstruction and CO₂ absorption under appropriate environmental conditions of the Martian surface. The material origin (Mars, Moon, and Earth surface.), classification (rocks, minerals, etc.), mineral class (phyllosilicates, sulfates, etc.), diverse mineral species (prehnite), and device for measuring CRISM

data are all included in the content of this spectrum library. This library is incorporated within the CAT tool and accessible on the PDS geoscience node. PDS provides a web-based interface where data can be searched, displayed, and downloaded by adding location information (latitude, longitude) of the surface.

2.4.2 MICA type spectral library

The MICA-type spectral library, derived from a CRISM sensor comprising multispectral and hyperspectral images, serves as a widely accepted and utilized standard for mineral identification and validation on the Martian surface. This comprehensive library is composed of data collected over a span of more than 7 years from CRISM TRDR data, along with recently discovered data from diverse Martian locations captured by the CRISM instrument. The library is the result of continuous efforts by researchers to expand the collection of spectral data available for the interpretation of Martian surface mineralogy. The library contains three types of spectra: Numerator, Denominator, and Ratioed I/F spectra. These spectra are used for mineral identification and mapping and have proven to be valuable tools in the study of the geology and mineralogy of Mars. The MICA library has a total of 31 minerals grouped into six different types: Mafic and iron oxide, sulfates, phyllosilicates, carbonates, hydrated silicates, and Ice. Viviano et al. (2014a). The planetary data and the CRISM website both provide access to the information corresponding to the MICA-type spectral library Viviano et al. (2014a).

2.4.3 RELab library

The Reflectance Experiment Laboratory (RELab) spectral library is a collection of visible to near-infrared reflectance spectra of minerals, rocks, and other planetary materials. The library was developed by the Planetary Spectroscopy Laboratory at Brown University and is widely used in planetary science and remote sensing applications. The Relab library contains over 2,000 spectra of minerals and rocks that are relevant to planetary science, including samples from the Moon, Mars, asteroids, and other planetary bodies. The spectra were acquired using a variety of laboratory instruments and under different environmental conditions, such as different illumination angles, temperatures, and pressures. One of the unique features of the Relab library

is its high spectral resolution, which allows for the identification of subtle spectral features that may not be visible in lower-resolution spectra. The library also includes detailed metadata for each sample, such as mineralogy, physical properties, and sample preparation methods. The Relab library is widely used in remote sensing applications for planetary exploration, including the analysis of data from several space missions such as the Mars Reconnaissance Orbiter, Lunar Reconnaissance Orbiter, and the Dawn spacecraft. The library is publicly available and can be accessed online through the Planetary Data System (PDS) website, which allows for easy access and sharing of data Carlé M. Pieters¹ (2004).

2.5 Surface Mineralogy of Martian surface

The Martian surface is a treasure trove of minerals that hold valuable information about the planet's geological history and potential for habitability. Various mineral groups can be found on Mars, each with its own significance. The mafic and iron oxide group, including minerals like olivine, pyroxene, and magnetite, are indicators of past volcanic and impact processes. The sulfate group, such as gypsum and jarosite, and the Phyllosilicates group, including clay minerals, suggest the presence of liquid water in the past and are potential markers for past or present microbial life. Carbonates, like calcite and magnesite, provide insights into Mars' past climate and water cycle. Hydrated silicates, such as serpentine and chlorite, form through hydrothermal alteration. Ice minerals, including water ice and carbon dioxide ice, are found in the polar ice caps and the atmosphere, respectively. Studying these minerals through remote sensing techniques enables scientists to unravel Mars' evolution and its potential for supporting life. Future missions will continue to focus on exploring these diverse mineral types for astrobiological investigations. By understanding the surface characteristics of minerals, including their spectral signatures and spatial distribution, researchers can enhance mineral mapping, mineral exploration, and the development of materials science applications. The significant absorption features of some of the most common minerals found on the Martian surface are discussed below. These minerals are also summarized in Table-2.4 for reference.

2.5.1 Mafic minerals and iron oxides

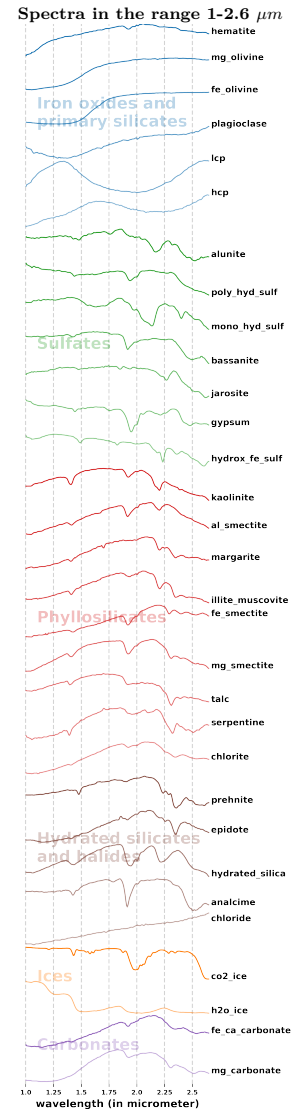
This mineral category primarily consists of iron and magnesium-rich minerals, including hematite, olivine, plagioclase, and pyroxene. Hematite detection, which is attributed to the Fe^{3+} transition within the 0.4-0.9 micrometer wavelength range, was accomplished using the CRISM detector. The absorption features at approximately 0.53 micrometer and 0.9 micrometer are crucial for identifying and distinguishing Fe^{3+} -bearing minerals like hematite, jarosite, and nanophase oxides Morris et al. (2000). Olivine, a mineral rich in magnesium and iron, exhibits broad absorption around 1 micrometer, which is further intensified by the electronic transition of iron within its structure, defining its spectral characteristics. In contrast, pyroxene spectra show broad absorption peaks centered around 1 micrometer and 2 micrometer, resulting from the domain transition of iron in multifaceted coordination. The pyroxene mineral group includes Low Calcium Pyroxene (LCP) and High Calcium Pyroxene (HCP). In LCP minerals, the absorption band is centered at approximately 0.9 micrometer and 1.8 micrometer whereas in HCP, the bands are located within 1.05 micrometer and 2.3 micrometer. The precise positions of these mineral absorptions are influenced by the calcium content within the pyroxene structure Burns (1993); Adams (1974). Plagioclase, another significant mineral found on the Martian surface, exhibits broad absorption characteristics centered at 1.25 micrometer and 1.31 micrometer, primarily on account of minor substitution of Fe^{2+} for Ca^{2+} . Plagioclase is typically detectable when other mafic minerals are present in an abundance of less than 5 percent Wray et al. (2013).

2.5.2 Sulfates

The sulfates group of minerals is abundantly present and widely distributed across the Martian surface. Notable concentrations of sulfates have been identified in Meridiani Planum and adjacent areas of Arabi, as well as within the internal layered deposits on the canyon system's floor and associated chaotic zones in Valles Marineris. The dunes surrounding the northern polar icecap are primarily composed of sulfate gypsum Gendrin et al. (2005); Lichtenberg et al. (2010). Unlike mono-hydrated sulfates, which exhibit variations in water vibrational combinations depending on the cation,

Table 2.4: Spectral features of some minerals found on the Martian surface and the spectra from MICA library

Mineral Groups	Mineral Names	Absorption Features
Mafic and Iron Oxides	Hematite	absorption at $0.53\mu\text{m}$ and close to $0.9\mu\text{m}$
	Fe/Mg Olivine	Broad absorption near $1\mu\text{m}$
	Plagioclase	Broad absorption at 1.25 and $1.31\mu\text{m}$
	Low calcium Pyroxene	absorption at 0.9 and $1.8\mu\text{m}$
	High calcium Pyroxene	absorption at 1.05 and $2.3\mu\text{m}$
Sulfates	Monohydrated Sulphate	absorption at $2.1\mu\text{m}$
	Polyhydrated Sulphate	absorption $2.1, 1.4, 1.9$ and $2.4\mu\text{m}$
	Alunite	doublet near 1.4 and $2.2\mu\text{m}$ absorption near 1.76 and $2.3\mu\text{m}$
	Hydroxy Fe-Sulphate	strong absorption at $1.48, 1.75,$ and $2.23\mu\text{m}$
	Jarosite	absorption at $0.9\mu\text{m}$ $1.47, 1.85$ and $2.25\mu\text{m}$
	Gypsum	triplet band absorption near 1.4 to $1.5\mu\text{m}$
	Bassanite	strong band absorption near $1.93\text{--}1.94\mu\text{m}$ multiple features near $2.1\text{--}2.3\mu\text{m}$
Phyllosilicates	Kaolinite	prominent absorption at $1.4\mu\text{m}$ a doublet near $2.2\mu\text{m}$
	Al-Smectite	absorptions 2.26 and $2.35\mu\text{m}$ doublet near $2.2\mu\text{m}$
	Illite / Muscovite	absorption at 1.9 and $2.3\mu\text{m}$
	Fe-Smectite	absorptions at $1.4, 1.9$ and $2.28\text{--}2.32\mu\text{m}$
	Mg-Smectite	narrow band absorption at $1.4\mu\text{m}$ absorption drop at $2.35\mu\text{m}$
	Talc	strong absorption near $1.9\mu\text{m}$
	Serpentine	OH overtone at $1.39\mu\text{m}$ weaker band at $2.1\mu\text{m}$ absorption centered at 2.32 and $2.5\mu\text{m}$
	Chlorite	strong absorption near $2.3\text{--}2.35\mu\text{m}$
	Prehnite	absorption between 2.35 and $2.36\mu\text{m}$
	Hydrated silicates	Hydrated Silica
Epidote		absorption at 2.30 and $2.51\mu\text{m}$
Analcime		triplet band absorption near 1.4 to $1.5\mu\text{m}$
Chloride		strong band near $1.93\text{--}1.94\mu\text{m}$ multiple features near $2.1\text{--}2.3\mu\text{m}$
Ices	H ₂ O-Ice	Broad absorption at $1.5\mu\text{m}$
	CO ₂ -Ice	tiny absorption at $1.435\mu\text{m}$
Carbonates	Fe/Ca carbonate	absorption at 2.33 and $2.53\mu\text{m}$
	Mg carbonate	the strong absorption at 2.30 and $2.51\mu\text{m}$



spectra of poly-hydrated sulfates display an absorption feature at 2.1 micrometer, resulting from a combination of elongation and flexion oscillations of water molecules. The detection of poly-hydrated sulfates is challenging due to the presence of another hydrous mineral that exhibits absorptions within 1.4 micrometer, 1.9 micrometer, and 2.4 micrometer Craig et al. (2006). Several sulfate species with distinctive spectral characteristics have been identified. Jarosite, for instance, displays absorption peaks centered at 1.47 micrometer and 1.85 micrometer Farrand et al. (2009a). Bassanite exhibits a prominent band within 1.93-1.94 micrometer, along with multiple absorption characteristics in the range of 2.1-2.3 micrometer attributed to H₂O Wray et al.

(2010). Gypsum spectra reveal a distinct band in the range of 1.4 micrometer to 1.5 micrometer, while alunite exhibits a doublet near 1.4 micrometer and 2.2 micrometer, accompanied by additional absorptions near 1.76 micrometer and 2.3 micrometer Swayze et al. (2008).

2.5.3 Phyllosilicates

Phyllosilicates comprise a diverse range of minerals found on the Martian surface, each exhibiting unique spectral characteristics. For instance, kaolinite prominently shows an absorption peak at 1.4 micrometer and a doublet near 2.2 micrometer, resulting from vibrational modes of the hydroxyl group and the Al-OH band. Al-smectite and mica also display a doublet near 2.2 micrometer but can be distinguished by the extra channel at 2.26 micrometer and 2.35 micrometer Ehlmann et al. (2011). Fe/Mg-phyllosilicates are prevalent in various geological settings, including stratified deposits, exposed crust outcrops, and occasionally in alluvial fans or deltas. This group encompasses Fe-smectite, Mg-smectite, serpentine, talc, prehnite, chlorite, and margarite. The identification of Fe/Mg-phyllosilicates is based on their compositional H₂O and OH absorption features at near 1.4 micrometer and a decrease at 2.35 micrometer feature, which shifts to elongated wavelengths as Mg replaces Fe Ehlmann et al. (2011). Mg-smectite exhibits narrower absorption characteristics around 1.4 micrometer and a decrease at 2.35 micrometer, talc demonstrates a strong absorption near 1.9 micrometer near 2.3-2.35 micrometer attributed to the Mg-OH band Calvin and King (1997), and prehnite exhibits absorption between 2.35 micrometer and 2.36 micrometer. Serpentine is identified by a diagnostic weaker band at 2.1 micrometer, an OH overtone at 1.39 micrometer, and absorptions centered at 2.32 micrometer and 2.5 micrometer. However, conclusive observations of serpentine pose challenges due to the requirement of a high Signal strength relative to noise to identify the superficial yet diagnostically significant 2.1 micrometer feature.

2.5.4 Hydrated silicates and halides

The mineral group consisting of epidote, zeolite, and chloride displays specific absorption characteristics at 2.21-2.22 micrometer arising from Si-OH amalgamation vibration, particularly at 2.26 micrometer, 1.91 micrometer and 1.4 micrometer because

of compositional H₂O and OH. Epidote exhibits a strong absorption near 2.24 micrometer and 2.35 micrometer, with a weaker absorption at 1.55 micrometer, enabling its differentiation from spectrally similar mixtures such as chlorite, illite, and calcite Carter et al. (2013a); Dalton et al. (2004). Zeolite exhibits notable absorptions within 1.4 micrometer, 1.9 micrometer, and 2.4 micrometer, which share spectral similarities with poly-hydrated sulfates. However, zeolite can be distinguished from poly-hydrated sulfates by its intense and subtle absorption at 2.5 micrometer and 1.79 micrometer Murchie et al. (2009). On the other hand, chlorides do not display distinct Serpentine attributes in the visible and near-infrared spectrum; however, they demonstrate unusually amplified thermal infrared radiative properties. This is accompanied by a decreasing slope in the spectral profile as the wave numbers decrease. Chlorides demonstrate a distinctive combination of a blue slope in the visible and near-infrared range, a red slope in the infrared range, and a relatively less prominent 3 micrometer H₂O feature. This suggests their hydrous nature compared to other surface materials detected by CRISM.

2.5.5 Ices

The unique spectral characteristics of ice, such as the broad absorption around 1.5 micrometer associated with crystalline H₂O ice and the small absorption feature at 1.435 micrometer in CO₂ ice spectra, offer a means to distinguish between different ice types. The narrow absorption at 1.435 micrometer is particularly advantageous because it is unaffected by atmospheric CO₂ bands at 2 micrometer, and it is approximately 2.3 times more potent than the subsequent secondary CO₂ ice bands at 2.281 micrometer Fink and Sill (1982).

2.5.6 Carbonates

Carbonates are formed when water captures atmospheric carbon dioxide, leading to the formation of a mineral group known as carbonates, which includes Mg-carbonate and Fe/Ca carbonate. The presence of carbonates can be identified by their characteristic absorption peaks at 2.3 micrometer and 2.5 micrometer, corresponding to vibrations of the C-O bond. Fe/Ca carbonate exhibits specific absorption peaks at 2.33 micrometer and 2.53 micrometer, while Mg-dominant carbonates shift to 2.30 micrometer and 2.51

micrometer. The abundance of calcium carbonates can be attributed to the weathering of Ca-dominant silicate rocks and the previous existence of carbonate rocks. The current saltwater on Mars is over-saturated with calcium carbonate. On the other hand, deposits of magnesium carbonate provide insights into past aqueous activity on the Martian surface Edwards and Ehlmann (2015); Walker et al. (1981).

2.6 Geological Information of different Study areas

Mars is known for its fascinating geology, which can be divided into two hemispheres, the northern and southern hemispheres. The northern hemisphere is characterized by a large and flat plain known as the Vastitas Borealis, which is home to several large craters, including the Lyot Crater and the Korolev Crater. In contrast, the southern hemisphere of Mars is much more rugged and varied, with several deep canyons, including the Valles Marineris, which is the largest canyon system in the solar system, and several large volcanoes, including the massive Olympus Mons, which is the largest volcano in the solar system. Fossae are another important geological feature on the Martian surface, with the Cerberus Fossae and the Valles Marineris being the largest systems. The Syrtis Major is a dark, circular region on the planet's surface that is thought to be a large volcanic plain. The Hellas Planitia and the Argyre Planitia are the two largest impact basins in the southern hemisphere of Mars, and both are characterized by large, flat plains. Craters are the most prominent feature on Mars, with the Hellas Planitia being the largest crater on the planet. Mars is also home to several large and significant valleys, including the Valles Marineris, Mawarth Vallies,

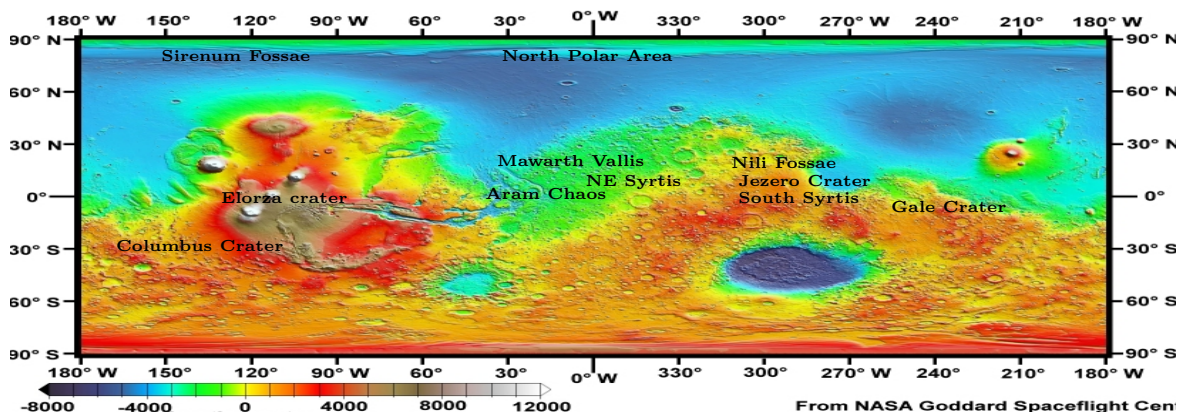


Figure 2.3: Mola elevation map showing location on the Martian surface where the mineral has previously been studied Smith et al. (2001)

Table 2.5: Different locations on the Martian surface with the dominant minerals

Area	Major Findings	References
Aram Chaos 2.6°N, 21.5°W	Monohydrated sulfate, Nanophase Ferric Oxide, Hydroxy sulfate	Lichtenberg et al. (2010)
Columbus 29.8°S, 166.1°W	kaolinite, polyhydrated sulfate 1, monohydrated sulfate Fe/Mg phyllosilicates, Jarosite, alunite, kaolinite gypsum, polyhydrated and monohydrated Mg/Fe-sulfates, kaolinite	Wray et al. (2009) Chaves et al. (2018) Wray et al. (2011)
Mawrth Vallis 22.3°N, 343.5°E	Fe smectite, alunite, Al smectite Fe/Mg-phyllosilicates, Al-Phyllosilicates, Hydrated Silica Fe/Mg-smectite, Al-phyllosilicate, hydrated silica	Sessa et al. (2018) Noe Dobrea et al. (2010) Michalski et al. (2010)
Melas Chasma 10.4°S, 72.7°W	nontronite, jarosite, Al-clays and leached clay Polyhydrated, monohydrated sulfates and jarosite High Calcium Pyroxene and Phyllosilicate	Weitz et al. (2015) Roach et al. (2010) Sivasankari and Arivazhagan (2019)
NE Syrtis 18°N, 77°E	Low-calcium pyroxene, Fe/Mg smectite, olivine Olivine, High calcium pyroxene, Low calcium pyroxene Fe/Mg-smectite, Low calcium Pyroxene	Ehlmann and Mustard (2012) Clenet et al. (2013) Scheller and Ehlmann (2020)
Nili Fossae 22°N, 75°E	Fe/Mg smectite, magnesium carbonate, olivine kaolinite, nontronite, chlorite, and vermiculite chlorite, prehnite, serpentine, kaolinite, potassium mica Prehnite, Chlorite, Silica	Ehlmann et al. (2009a) Xue et al. (2018) Ehlmann et al. (2009b) Viviano et al. (2013)
Kashira crater 27.0°S, 341.7°E	kaolin-group mineral halloysite	Goudge et al. (2015b)
Elorza Crater 304.8°E, 8.76°N	phyllosilicates (vermiculite) and mafic silicates	Jain and Chauhan (2016)
North polar area 88°N, 15°E	Gypsum	Fishbaugh et al. (2007)
Sirenum Fossae 35.57°S, 197.26°W	Kaolinite	Wray et al. (2011)
South Syrtis 18.855°N, 77.519°E	Ca/Fe carbonate, illite	Glotch and Rogers (2013)
Gale Crater 5.5°S, 137.8°E	Olivine and High-calcium Pyroxene Kaolinite, Chlorites, Smectite, Jarosite, Northupite	Seelos et al. (2014) Xue and Jin (2013)
Jezero Crater 18.38°N, 77.58°E	Mg-rich carbonate, olivine Fe/Mg-smectites, Al-phyllosilicates, carbonates	Goudge et al. (2015a) Salvatore et al. (2018)
Robert Sharp craters 4.17°S, 133.42°E	Akaganeite	Peretyazhko et al. (2018)

Ma'adim Vallis, and the Valles Alpes, which were mostly created by past, severe flooding. The MRO CRISM instrument has detected clays in the Jezero crater, indicating the past presence of water. This makes Jezero Crater a prime location for the Mars 2020 mission's objective of exploring a potentially habitable environment for remnants of past life. Mawrth Vallis was also considered a potential landing site for the Mars Science Laboratory (MSL) mission in 2011, but Gale was ultimately chosen as the landing site for the Curiosity mission due to indications of water by the presence of clays and sulfate minerals. Researchers have already explored various areas on the Martian surface some of which are listed in table-2.5.

2.7 Different Supervised Learning Models

2.7.1 Artificial Neural Network (ANN)

ANNs are computational models inspired by the human brain's structure and functioning, used extensively in machine learning for a wide array of tasks. ANNs comprise interconnected units called neurons or perceptrons, organized into layers: the Input Layer, Hidden Layers (one or more), and the Output Layer. Neurons take inputs, apply mathematical operations, and produce outputs. Connections between neurons have associated weights that signify the strength of the connection, and these weights are adjusted during training to learn the relationship between inputs and outputs. Activation functions introduce non-linearity into the network, enabling it to model complex data patterns effectively. Key activation functions include sigmoid, Rectified Linear Unit (ReLU), tanh, and softmax. The feedforward propagation process involves multiplying inputs by weights, summing the results, and passing them through the activation function in each neuron, progressing through the layers from Input to Output. To evaluate how well the network performs, a loss function quantifies the error between predicted and actual target values, with different loss functions tailored to specific tasks. Backpropagation, the core of training, refines the network by computing gradients of the loss with respect to weights and updating weights using optimization algorithms like gradient descent. Hyperparameters such as learning rate, the number of hidden layers, the number of neurons in each layer, and activation functions profoundly affect the network's behavior and training process. Training occurs over multiple epochs, where the entire dataset is iteratively processed. Batch size determines the number of data points used in each forward and backward pass. Techniques like dropout and L2 regularization mitigate overfitting, where the network fits the training data too closely but struggles to generalize to new data. Validation and testing datasets are employed to monitor progress during training and assess the final model's generalization performance, ensuring the ANN's effectiveness in various machine learning applications. Understanding and selecting appropriate hyperparameters are critical for successfully training ANNs, making them versatile and powerful tools in modern data-driven tasks.

2.7.2 Convolutional Neural Network (CNN)

CNNs represent a groundbreaking advancement in machine learning, tailor-made for processing structured grid data, with their primary application domain being image and video analysis. At their core, CNNs are characterized by a hierarchical architecture composed of several key components. Convolutional layers initiate the process, applying convolutional operations through small filters or kernels. These kernels systematically slide across the input data, performing element-wise multiplications and aggregations, leading to the extraction of distinctive features. Notably, CNNs employ multiple parallel filters, resulting in the creation of feature maps that capture diverse aspects of the input data. Subsequently, pooling layers are often integrated to curtail the spatial dimensions of the feature maps while retaining critical information, thus reducing computational complexity. The introduction of non-linearity through activation functions like ReLU ensures that CNNs can grasp intricate patterns and relationships within the data. Fully connected layers follow, transforming the flattened feature maps into a 1D vector and facilitating traditional neural network operations, particularly suitable for tasks such as image classification. Anchoring the network are the weights and biases, which are learned during training to optimize the network's predictive capabilities. Vital hyperparameters wield significant influence over CNNs' effectiveness, such as the kernel size and stride, which govern the size and detail of features extracted. Padding, through techniques like zero-padding or valid padding, plays a role in controlling the spatial dimensions of output feature maps. The number of filters in convolutional layers dictates the complexity and richness of the features detected, with a higher count enabling the detection of finer details. Dropout, a regularization technique, is employed to fend off overfitting by randomly deactivating neurons during training, encouraging the network to learn more robust features. The learning rate determines the magnitude of weight updates during training, shaping the network's convergence and stability. Training extends over numerous epochs, encompassing multiple passes through the dataset. Additionally, the choice of activation functions in convolutional layers, such as ReLU, Leaky ReLU, or Sigmoid, can significantly impact the model's performance. Lastly, the batch size, governing the number of data samples processed in each forward and backward pass, is yet another essential parameter influencing CNN training. Altogether, these elements and parameters

collectively shape the essence of Convolutional Neural Networks, empowering them to automatically learn and discern intricate patterns within structured grid data, making them an indispensable tool in modern computer vision and deep learning applications.

2.7.3 Support Vector Classifier (SVC)

SVC stands as a robust and widely-used machine learning algorithm, particularly adept at handling binary classification tasks. Its fundamental premise revolves around identifying the optimal hyperplane within the feature space that maximally separates two distinct classes of data points. This hyperplane is strategically positioned to maximize the margin between the classes, a feature that renders SVC resistant to outliers and enhances its generalization capabilities. The linchpin of SVC's operation lies in the concept of "support vectors," which are those data points closely situated near the decision boundary, thus influencing the positioning and orientation of the hyperplane. The choice of kernel function serves as a pivotal parameter, permitting the transformation of the original feature space into a higher-dimensional space. Common kernels encompass linear, polynomial, radial basis function (RBF), and sigmoid, with each catering to different degrees of problem complexity and non-linearity. Additionally, the regularization parameter 'C' exercises control over the balance between margin maximization and classification error minimization, with smaller 'C' values promoting broader margins but potentially tolerating misclassifications, and larger 'C' values enforcing narrower margins but minimizing classification errors. For certain kernel functions like RBF, the gamma parameter assumes significance, determining the influence of individual training examples—smaller gamma values conferring a broader influence and larger values exerting a localized impact. In the context of polynomial kernels, the 'degree' parameter steers the degree of the polynomial function employed for feature space transformation, with higher degrees accommodating more intricate relationships. The option to assign class weights, through the 'class_weight' parameter, proves invaluable in scenarios characterized by imbalanced datasets, enabling the prioritization of minority classes. 'Shrinking,' a computational efficiency enhancement technique, prunes the number of support vectors engaged in training when activated. Enabling probability estimation furnishes probability scores alongside class predictions, a feature relevant in certain applications. Finally, the 'tolerance' parameter delineates

the tolerance level for the stopping criterion during optimization, with smaller values honing accuracy at the expense of longer training durations. In essence, Support Vector Classification operates on the premise of finding the optimal separation hyperplane in the feature space, and the judicious selection and configuration of kernel functions and hyperparameters are pivotal for SVC's efficacy across diverse real-world classification tasks, where it excels due to its robustness and adaptability to complex data distributions.

2.7.4 Random Forest Classifier (RFC)

A RFC is a popular ensemble machine-learning algorithm used for both classification and regression tasks. It is known for its robustness and high predictive accuracy, making it a go-to choice for various applications. The Random Forest algorithm is based on the principle of bagging and combines multiple decision trees to produce a more robust and accurate model. Here's an introduction to RFC, including its general concept and key parameters. The RFC is an ensemble learning method that builds a collection of decision trees during training and combines their outputs to make predictions. Each decision tree is trained on a randomly selected subset of the training data, and the final prediction is determined by a majority vote (for classification) or an average (for regression) of the individual tree predictions. This ensemble approach reduces overfitting and increases the model's generalization capability. RFC is a powerful ensemble learning technique that combines multiple decision trees to make robust and accurate predictions in classification tasks. RFC leverages bootstrapping to create diverse subsets of the training data and introduces randomness during feature selection for each decision tree. This diversity and randomness reduce overfitting and enhance generalization. The final prediction in RFC is determined through a majority vote among the individual decision trees. Key parameters include the number of trees (`n_estimators`), max depth of trees (`max_depth`), minimum samples per leaf (`min_samples_leaf`), and the maximum number of features considered for splitting nodes (`max_features`). RFC also allows you to control bootstrapping, set a random seed for reproducibility (`random_state`), and specify the criterion for splitting nodes (e.g., "gini" or "entropy"). Additionally, you can assign class weights to handle imbalanced datasets and use out-of-bag samples to estimate model accuracy (`oob_score`). Proper parameter tuning is

essential to optimize RFC performance for specific classification tasks, making it a versatile and widely-used algorithm in machine learning.

2.8 Performance Measures

Evaluation metrics play a pivotal role in the realm of machine learning, and they are closely tied to the specific tasks at hand, such as classification and regression. While certain metrics are tailored for particular tasks, some, like precision-recall, offer versatility by being applicable across multiple tasks. These tasks, classification and regression, are both examples of supervised learning, a fundamental component of the vast landscape of machine learning applications. The choice of evaluation metrics is far from arbitrary; it's a strategic decision aimed at enhancing the overall predictive power of our models before they are deployed for real-world use on unseen data. Relying solely on accuracy, a common but not always sufficient measure, can be problematic. In fact, it can lead to critical issues when our models are applied to novel, unseen data, potentially resulting in subpar predictions. By examining precision, recall, F1-Score, specificity, ROC-AUC or other relevant metrics, we gain a comprehensive understanding of our model's strengths and weaknesses. We can then make informed decisions regarding model selection, optimization, and deployment strategies.

- **TRUE Positive (TP):** These are instances that the model correctly predicted as positive, and they actually belong to the positive class.
- **TRUE Negative (TN):** These are instances that the model correctly predicted as negative, and they actually belong to the negative class.
- **FALSE Positive (FP):** These are instances that the model incorrectly predicted as positive, but they actually belong to the negative class. False positives are also known as Type I errors.
- **FALSE Negative (FN):** These are instances that the model incorrectly predicted as negative, but they actually belong to the positive class. False negatives are also known as Type II errors.

2.8.1 Precision

Precision quantifies the accuracy of positive predictions made by a classification model. Specifically, it measures the proportion of true positive predictions (correctly predicted positive instances) among all instances predicted as positive. Mathematically, precision is defined as:

$$Precision = \frac{TP}{TP + FP} \quad (2.8.1)$$

2.8.2 Recall

Recall, also known as true positive rate, indeed measures the ability of a classification model to correctly identify all the actual positive cases. It is an essential performance metric, especially in scenarios where the cost or consequences of false negatives (Type II errors) are higher than false positives (Type I errors). Your example of medical cases underscores the critical importance of recall in certain real-world applications.

Mathematically, Recall is defined as:

$$Recall = \frac{TP}{TP + FN} \quad (2.8.2)$$

2.8.3 F-score

The F1-Score is a single metric that balances the trade-off between precision and recall. It provides a harmonic mean of precision and recall, which makes it particularly useful when dealing with imbalanced dataset or situations where both false positives and false negatives are costly. The F1-Score ranges between 0 and 1, with higher values indicating better model performance. Mathematically, Recall is defined as

$$Fscore = 2 * \frac{Precision * Recall}{Precision + Recall} \quad (2.8.3)$$

Interpretation: A high F1-Score indicates that the model has a good balance between making accurate positive predictions (precision) and capturing most of the actual positive instances (recall). A low F1-Score suggests that the model either has low precision (many false positives) or low recall (many false negatives). The F1-Score is

commonly used in situations where you want to find a balance between precision and recall.

2.8.4 Accuracy

Accuracy, in the context of machine learning and classification tasks, measures the overall correctness of a model's predictions. In other words, accuracy quantifies the proportion of correctly predicted instances out of the total instances in the dataset. Accuracy is computed as

$$Accuracy = \frac{TP + TN}{TP + TN + FP + FN} \quad (2.8.4)$$

2.8.5 Confusion Matrix

A confusion matrix is a fundamental tool in the field of machine learning and classification. It is used to assess the performance of a classification model by comparing its predictions to the actual class labels in a tabular format. The confusion matrix provides a detailed breakdown of how many predictions were correct and how many were incorrect, making it a valuable resource for understanding the strengths and weaknesses of a model. The confusion matrix provides a granular view of a model's performance and helps data scientists and machine learning practitioners make informed decisions about model selection, optimization, and deployment. It is particularly valuable in cases where the consequences of false positives and false negatives differ significantly or where a detailed understanding of model behavior is required.

A multiclass confusion matrix provides a concise summary of a classification model's performance by showing how well it classifies instances into multiple classes. It reveals the number of correct predictions (true positives) for each class. It shows where the model made errors by indicating false positives and false negatives for each class. It helps assess how well the model performs for individual classes, highlighting strengths and weaknesses. It calculates overall metrics like accuracy, precision, recall, and F1-score to assess the model's effectiveness across all classes.

2.8.6 Receiver Operating Characteristic (ROC) curve

The ROC curve is a graphical representation of a classification model's performance across various decision thresholds. It plots the either TRUE Positive Rate (TPR) or the recall against the FALSE Positive Rate (FPR) at different threshold settings. A multiclass ROC curve is a graphical representation of a classification model's performance when there are more than two classes. It shows how well the model can distinguish between different classes by plotting the TPR against the false positive rate (FPR) for various classification thresholds. It illustrates the trade-off between sensitivity (recall) and specificity for different classes, helping you choose an appropriate threshold for your specific application. The Area-Under-the-Curve (AUC) of a multiclass ROC curve quantifies the model's overall discriminative ability. A higher AUC indicates better performance.

Chapter 3

Literature Review

Mineral identification on the Martian surface is a fundamental step in understanding the geological and geochemical processes that have shaped the planet's surface. The manual approach for mineral identification in CRISM images involves selecting a region of interest, which act as the numerator, and an unremarkable region, that act as the denominator, to obtain the ratioed I/F CRISM image. The spectral rationing enhances the spectral absorption characteristics and reduces the multiplicative noise. These spectra are then visually compared with a spectral library to identify minerals based on their absorption features. However, this approach is time-consuming and requires tremendous manual labour. The identification of an unremarkable zone within the image possibly on the same line sample and finding the right match of numerator, denominator and stretch limit requires immense domain expertise. As a result, there is a growing need for automated solutions. Initially, distance-based similarity-matching techniques were employed but struggled to capture semantic differences, rendering them inadequate for mineral identification. Therefore, alternative approaches such as probabilistic, unsupervised, and neural network models have been developed to address these limitations and demonstrate improved effectiveness in mineral identification. Some of the distance-based methods, as well as the alternative techniques, are discussed in this section.

Table 3.1: Different genres of methods used in literature for mineral identification in CRISM data

Method Genre	Method Name	Study Area	References
Distance-based Matching	Spectral Angular Mapper(SAM)	Jezero Crater, Gale Crater	Yang et al. (2014), Xue and Jin (2013)
	Euclidean Distance(ED)	Jezero Crater, Nili Fossae	Allender and Stepinski (2017a), Saramathan and Parente (2021a)
	Mahalanobis Distance(MD)	Jezero Crater, Mawarth Vallis	Bue (2014), Bue et al. (2011a), Wu et al. (2021b) Wu et al. (2021a)
Distribution-based unsupervised methods	Matched Filtering(MF)	Nili Fossae, Gale Crater	Dunder and Ehlmann (2016)
	Gaussian mixture model (GMM)	Nili Fossae	Plebani et al. (2022),
	Hierarchical Dirichlet process (HDP)	Aram Chaos	Yerebakan et al. (2014)
	Partially-Observed HDP (PO-HDP)	Nili Fossae	Dundar et al. (2013a)
Distance-based unsupervised methods	Hierarchical Bayesian Model (HBM)	Gale Crater	Allender and Stepinski (2017a)
	Ordering Points To Identify the Clustering Structure (OPTICS), Discovery through Eigenbasis Modeling of Uninteresting Data (DEMUD)	Nili Fossae	Thompson et al. (2010)
	Sequential Maximum Angle Convex Cone (SMACC), N-FINDR	Jezero crater	Caggiano et al. (2019)
Neural Networks	Deep Neural Network(DNN)	Nili fossae	Saramathan and Parente (2021a)
	Active learning-based classifier, Generative adversarial network (GAN)	Jezero Crater	Kumari et al. (2023a)
	CNN, ANN, SVM, RFC	Mawarth Vallis	

3.1 Distance-based matching methods

Distance-based methods are used for mineral mapping because they are relatively simple to implement and can be used to quickly classify large amounts of hyperspectral data. The distance-based methods are based on the fact that minerals have unique chemical compositions and crystal structures that affect the way they reflect and absorb light. By computing the distance or angle between a pixel's spectrum signature and the spectra of reference minerals in a library, the pixel can be assigned to the mineral that bears the closest resemblance.

Euclidean distance Danielsson (1980) is a simple and commonly used distance metric that measures the straight-line distance between two points in spectral space. *Mahalanobis distance* McLachlan (1999) is a more complex metric that accounts for the correlations between the spectral bands and is, therefore, more robust than Euclidean distance. *Spectral Angle Mapper (SAM)* Kruse et al. (1993) is based on the idea that the spectra of different minerals have different shapes in spectral space, and that these shapes can be characterized by the angles between them. The main advantage of using SAM is that it is invariant with scale and illumination. *Matched Filtering (MF)* Turin (1960) is based on the idea that the spectral signature of a pixel can be decomposed into a linear combination of the spectral signatures of the end members in the library, and that the end member with the highest coefficient is the one that best represents the pixel.

Although Distance based approach is so simple to map the mineral very less literature exists for it. The main reason behind this similarity method is designed to capture the global difference between two vectors. On the contrary, mineral identification is based on similarity involving the presence of absorption dip with the wavelength ranges.

3.2 Distribution-based unsupervised methods

Probabilistic methods are favoured in mineral mapping due to their ability to provide accurate and comprehensive characterization of mineralogy, surpassing traditional approaches based on thresholds or linear models. These methods offer several advantages. Firstly, they allow for uncertainty quantification, enabling the estimation of mineral

abundances and classifications with associated uncertainty. This is crucial when dealing with mineral mixtures or noisy spectral signatures. Secondly, probabilistic methods account for non-linearity, acknowledging that the relationship between reflectance spectra and mineral abundances is often non-linear. Linear models may not capture this accurately, making probabilistic methods more suitable for precise abundance estimation. Lastly, probabilistic methods exhibit robustness to outliers and noise in the data. Several widely employed probabilistic methods in this context are highlighted below.

- **Gaussian Mixture Model (GMM)** Reynolds et al. (2009) is a parametric probability density function used to model the distribution of observed data by combining multiple Gaussian distributions. It aims to identify distinct mineral components in spectral data by representing their spectral signatures as Gaussian distributions. The GMM assumes that each pixel in the image contains a mixture of mineral components and estimates the proportion of each component in every pixel. To overcome limitations in handling skewed distributions or unknown numbers of components, the *Infinite Gaussian Mixture Model (IGMM)* has been introduced. It allows for the estimation of inference and other component parameters in a unified process. However, to handle situations requiring non-Gaussian or differently shaped distributions, the *Infinite Infinite Gaussian Mixture Model (I²GMM)* has been developed Yerebakan et al. (2014). It is doubly non-parametric and enables the identification of the number of components for each cluster with various shapes and sizes. GMM is relatively simple and computationally efficient for mineral mapping, but it assumes Gaussian distributions for mineral spectral signatures and does not incorporate prior knowledge about mineral distributions in the region of interest, limiting its accuracy in some cases.
- **Hierarchical Dirichlet process (HDP)** Wang et al. (2011) is a Bayesian non-parametric model that enables the clustering of data points into multiple groups based on their similarity, without requiring a predefined number of clusters. It provides a flexible framework for discovering latent structures in data. In the context of mineral identification using spectral data, the *Partially Observed Hierarchical Dirichlet process (PO-HDP)* is a variant of this model. The PO-HDP is specifically designed to identify the presence of various minerals within a specific region based

on spectral information. It operates under the assumption that each pixel in a spectral image represents a mixture of different mineral components. By utilizing the spectral data, the model estimates the proportion of each mineral component within each pixel, allowing for accurate mineral identification and mapping. The PO-HDP offers a powerful approach for analyzing complex spectral datasets and extracting valuable information about the mineral composition of an area. Its Bayesian nature provides a robust and flexible framework for handling uncertainties and missing data.

- **Hierarchical Bayesian Model (HBM)** Allenby and Rossi (2006) models the observed data as a function of unknown parameters, which are themselves modelled as random variables. In the context of mineral mapping, the observed data could be spectral data collected from a satellite or airborne sensor, and the unknown parameters could be the proportions of different minerals present in each pixel of the image. One advantage of the HBM is that it is a flexible modeling framework that can be adapted to different data types and sources of prior knowledge. This prior information can be derived from geological maps, previous mineral surveys, or other sources of information. By incorporating prior knowledge into the model, the HBM can improve the accuracy and robustness of the mineral mapping results, allowing for the identification of mineral deposits correlated with certain geological features. Plebani et al. (2022) used a Bi-Level Bayesian Gaussian mixture model, that had shown promise in eliminating nonlinear noise and determining both high and low-abundance mineral aspects in CRISM images, where GMM is implemented for the identification of the spectral and spatial distribution of minerals at pixel scale for each mineral class. This developed model made efficient, accurate, and scalable assessments toward automation of mineral identification by replacing traditional spectral analysis techniques.

3.3 Distance-based unsupervised methods

The unsupervised classification approach is widely used for mineral characterization on the Martian surface due to the deficit of classified training data, as it does not require any prior knowledge of the end members. Unsupervised clustering methods

find natural groupings on similar spectral characteristics in the unlabeled data and then match each group with the spectral library to assign a label. These methods also can identify new mineral types that may not be present in a pre-defined mineral library and help researchers to discover new mineral types or identify previously unknown minerals.

- **Ordering Points To Identify Clustering Structure (OPTICS)** Ankerst et al. (1999) identifies the natural clustering structure of a dataset without assuming a fixed group of clusters or any previous information of the data distribution. It does this by defining a hierarchy of density-based clusters based on the concept of reachability distance. Allender and Stepinski (2017a) used OPTICS algorithm to cluster super-pixels to reduce redundancy in identified minerals and make more confident from the respective region on the Martian surface, followed by **Discovery via Eigenbasis Modeling of Uninteresting Data (DEMUD)** analysis on the super-pixels to assign a label based on threshold operation for anomaly detection to find rare minerals. This method has been applied to Hesperia Planum (Fe/Mg smectite), Aram Chaos (Jarosite, Kieserite), and Juventae Chasma (Mg-Olivine, Monohydrated Sulphate).
- **Sequential Maximum Angle Convex Cone (SMACC)** Gruninger et al. (2004) method constructs convex cones around each data point, and then merges the cones that have similar spectral properties. **N-FINDR** Winter (1999) is another unsupervised algorithm that uses Non-negative Matrix Factorization (NMF) to identify pure spectral endmembers in an iterative process. In Thompson et al. (2010) authors used these methods on CRISM images and detected several dominant minerals like Kalonite, carbonate, Olivine, and phyllosilicates. Nevertheless, these methods can be time-consuming, and it is still necessary to identify the minerals of the suspected detections by comparing them with spectra obtained from laboratory analysis.

3.4 Neural networks

Neural Networks are renowned for their ability to uncover hidden patterns in data. However, they typically require a substantial amount of labeled training data, which can be a challenge when it comes to mineral identification on the Martian surface. The

scarcity of ground truth or training data hinders the development of supervised learning models for this purpose. Currently, there are only a few studies that have employed neural network-based approaches with CRISM hyperspectral data for mineral exploration Caggiano et al. (2019). In Saranathan and Parente (2017) authors proposed an active learning-based classifier for neutral spectra, aiming to reduce the number of labeled examples required for training. They employ a selective sampling technique that evaluates the quality of each neutral spectrum individually, minimizing the need for expert labeling and reducing costs. The algorithm utilizes the Query-by-committee approach, iteratively selecting the most informative data points for labeling and training a committee of models on the same training set. Through multiple iterations, the model improves over time, with a particular emphasis on addressing problematic areas. The subjective nature of labeling allows the proposed framework to learn complex boundaries in classification tasks.

In Saranathan and Parente (2021a), generative models were employed to improve the distinguishability of spectra. The authors manually labeled samples from 30 CRISM images, using MICA identification for classification. A detailed preprocessing pipeline was presented to prepare the data for the generative model. The study demonstrated that the features acquired by the Generative Adversarial Network (GAN) exhibited greater efficacy in distinguishing mineral signatures within the CRISM database when compared to summary parameters and traditional similarity metrics. For pixel classification, the SAM metric was used to identify the best match between the target pixel and the spectra generated by the models.

Chapter 4

A Fully-Automated Framework for Mineral Identification

This chapter introduces an automated framework designed to classify the spectral data within CRISM hyperspectral images. It addresses a crucial gap in Martian surface mineralogy research by providing a method to build supervised learning models for mineral classification. This achievement is of paramount importance as it enables us to unlock the valuable insights hidden within CRISM data, shedding light on Mars' surface composition and geologic history. The cornerstone of this chapter is the innovative approach to generating the essential training data. By augmenting mineral spectra from the Minerals Identified in CRISM Analysis (MICA) spectral library, the framework ensures the models capture the key absorption signatures while accounting for the variability present in real-world Martian surface conditions. Further we have discussed detailed methodology, including the pre-processing pipeline and feature extraction techniques that enhance the accuracy of mineral classification. Experimenting with different parameters of the augmentation process, the optimal set of parameters are fixed. Also, the need for different preprocessing steps in the pipeline is established by an uncertainty analysis. The chapter also provides validation through the application of various supervised learning models and a comparative analysis with previously employed methods showcasing the framework's practical utility and robustness.

The characterization of minerals on the Martian surface is challenging because of instrumental artifacts and seasonal fluctuations in CO₂, ice aerosols, and dust in

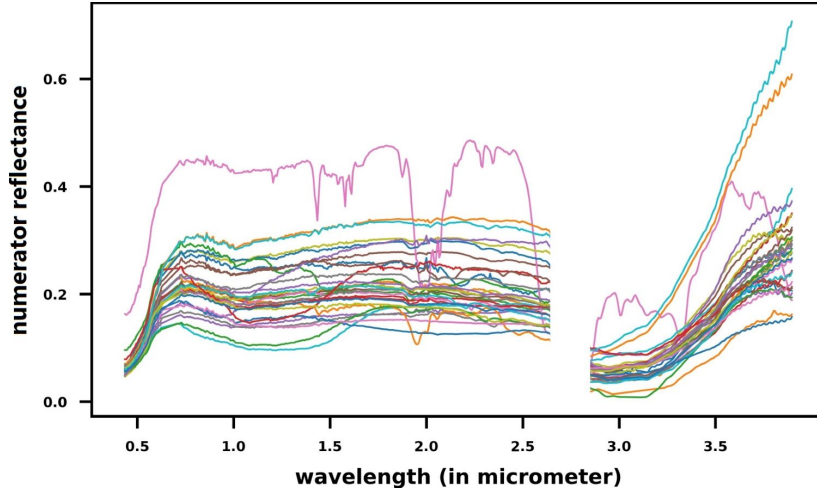


Figure 4.1: Numerator reflectance spectra of 31 different minerals/ mineral groups provided in the MICA spectral library in the available wavelength range of 0.3-3.9 micrometer are shown by different colours.

the Martian environment while collecting the data. So, the raw-collected Experimental Data Record (EDR) with 544 bands, undergoes numerous correction stages and a Map-Projected Targeted Reduced Data Record (MTRDR) is formed and left out with 489 bands. From this MTRDR data, spectral summary parameters and browse products have been calculated, which is essential for spectral analysis and visual interpretation for the characterization of the Martian surface Viviano-Beck et al. (2014).

MICA (Minerals Identified in CRISM Analysis) type spectral library, which was made available at the Planetary Data System (PDS) geoscience node in 2014, and since then has been used vastly for both identification and validation of the minerals. The content of MICA type spectral library includes numerator, denominator, and ratioed (ratio of radiance to incident and solar radiation) reflectance spectra for 31 distinct minerals/mineral groups [figure 4.1], which was prepared by analyzing CRISM hyperspectral imagery from different mineral-rich locations on Martian surfaces Viviano-Beck et al. (2014).

Despite the availability of such an extensive spectral library, the development of automated systems for mineral identification is hugely still in progress. Most of the methods for mineral mapping in the initial days were constrained by the use of similarity metrics on the full spectra distribution to map the mineral classes and were limited by the quality of the end results. The mineral identification is not so straightforward, because, firstly, the reflectance values for a mineral in the spectral library

and the reflectance values for that same mineral in MTRDR data may be at different scales [figure 4.2a], secondly, the presence of different continuum noise in MTRDR data changes the global shapes of the spectra Parente et al. (2011) through the absorptions are preserved [figure 4.2b]. For this reason, building learning models for mineral mapping based on similarities in position and strength of absorption features has been a focus of research in recent years Allender and Stepinski (2017b); Bue et al. (2011b); Dundar et al. (2013b); Saranathan and Parente (2021b). One major challenge to building a supervised model for mineral identification in CRISM data is the insufficiency of labelled data for model training. A dearth of studies on spectral pre-processing to increase mapping quality is also observed.

Supervised models are acclaimed for recognizing the hidden features in data, and may thus be trusted to map test pixels based on the absorption features; though the challenge lies here in accumulating an unbiased and divergent training dataset. In this study, a new data augmentation technique is used on the mineral spectra available in the MICA-type spectral library to generate the training data that eliminates the challenges of manual intervention to gather the training data. The training data being generated solely from the library makes these models applicable to any MTRDR

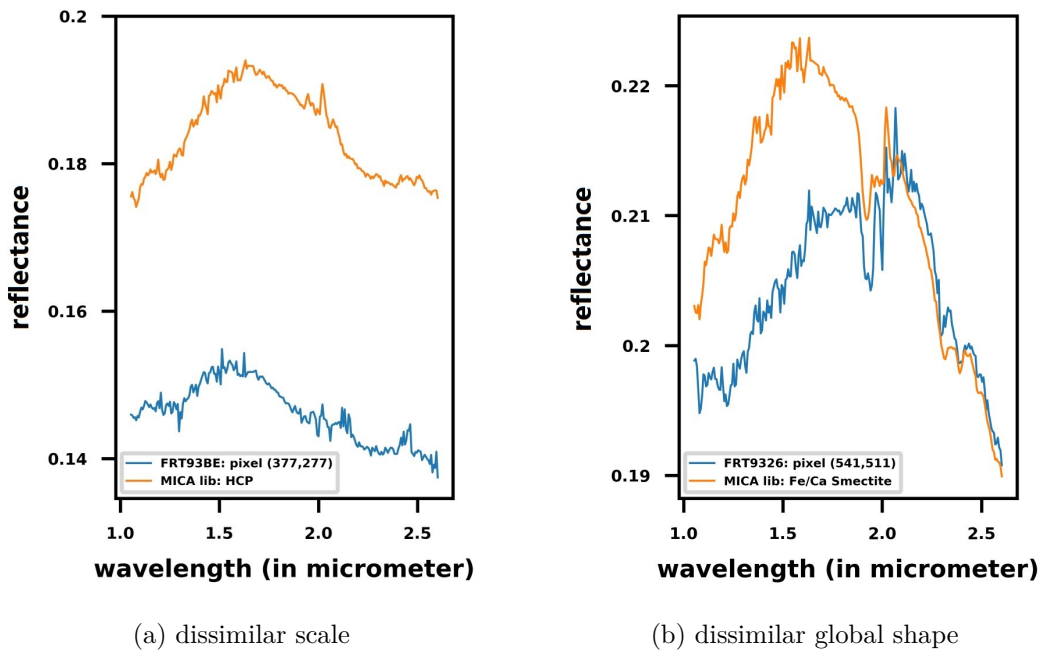


Figure 4.2: MICA library spectra in blue colour and sample pixel spectra from an MTRDR data in orange colour

data of the Martian surface. Also, a new idea of feature extraction is proposed that calculates the absorption information over the most diverse wavelength ranges in a spectrum, that in turn helps to train the models faster with improved accuracy. The objective of this study is to create a common framework for mineral mapping in CRISM hyperspectral images, that can be used with any supervised learning model. This study does not compare or evaluate the competence of the used supervised learning models; instead, its sole goal is to determine the efficacy of the framework with the provided data augmentation and absorptions extraction step. To our knowledge, no such fully-automated framework for mineral identification in the Martian data is available till date.

4.1 Pre-processing Pipeline

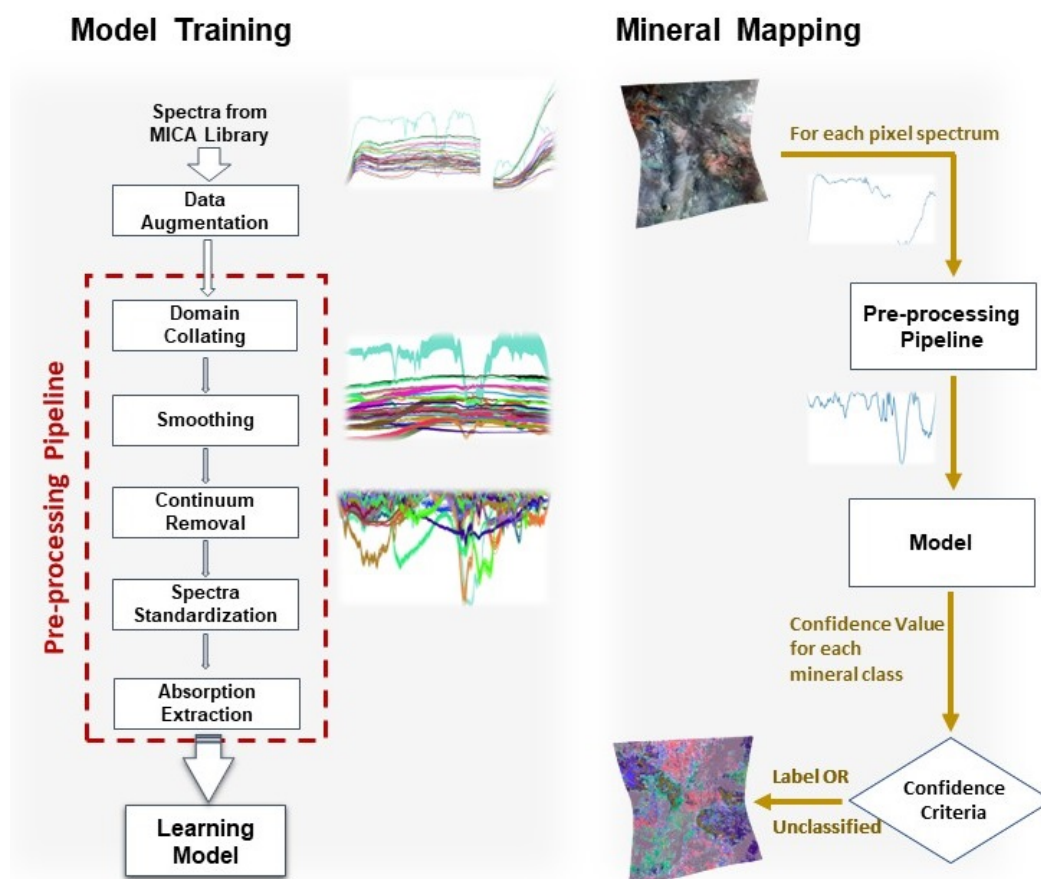


Figure 4.3: Flowchart of the data pre-processing pipeline that is used to train the supervised models, and the mineral mapping procedure using the trained models at right

In this section, the process to create the augmented data is described first, and then

the pre-processing pipeline to build the viable training data is discussed. The domain collating step is used to establish the consistency of the features in the training data, the smoothing step is necessary to remove overly spurious portions of the spectrum as well as small unwanted kinks that occur due to various noises in real data, the continuum removal process is required to improve some absorption signatures in the spectrum that are subdued by the presence of continuum in real data, and whereas the standardisation step introduces high variance in the training data to speed up the learning process. The feature extraction procedure is then used to create the training dataset by extracting features from the most diverse of spectral areas. The illustrations in figure 4.3 depict the model training and mineral identification procedure.

4.1.1 Data Augmentation

Data enhancement essentially involves introducing such noise into training data which has a regularization effect, thus increasing the strength of the supervised learning models. MICA library contains single sample (ground truth) spectra for 31 different minerals. Building a supervised learning model with such a small number of training data could make the model biased to some features or sensitive to some other features, making it harder for the model to generalize absorption patterns, which could decrease output accuracy. Using mineral signatures in the MICA library to augment spectral signatures of minerals is not an obvious approach. The nonlinear multiplicative noise that predominates in CRISM images is particularly difficult to replicate via augmentation. This noise component varies not only between distinct images but even within the same image. In this study, a new augmentation method has been used that preserves the direction of the spectra curve while deviating randomly within a carefully chosen limit from the original spectra, and then was combined with noise and a randomly generated continuum in order to make the model work with real data.

step-1: (*Augmenting the pure spectra from MICA*)

Let Aug is the spectra augmented from the pure spectra Org in MICA library. Let w' is the previous wavelength of w where a reflectance is captured. Org_w and $Org_{w'}$ are the reflectance values for original mineral spectra in MICA library and Aug_w and $Aug_{w'}$ are the determined reflectance values in the augmented spectra at wavelength w and w' respectively. Equations (4.1.1-4.1.3) generates Aug from Org constrained by

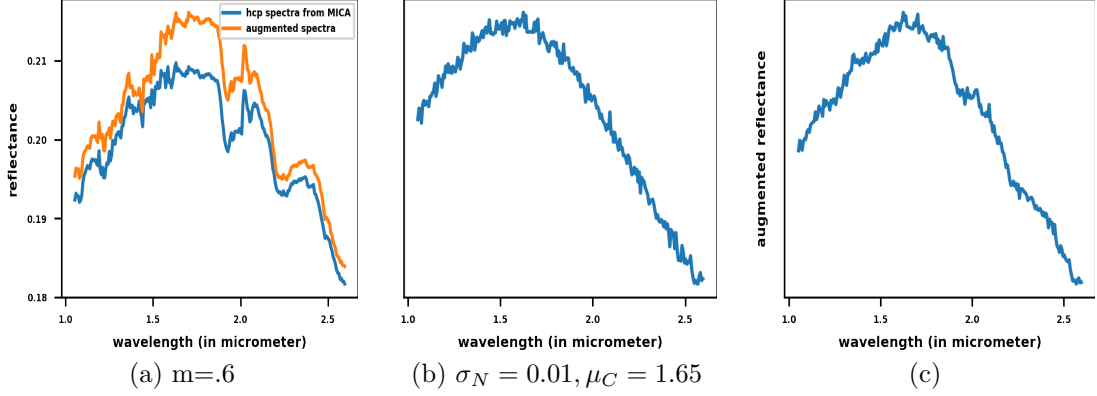


Figure 4.4: (a) Augmented pure spectrum, (b) Generated Continuum with noise, (c) Augmented pure spectra blended with continuum and random noise

a deviation limit m .

$$change_w = (Org_w - Org_{w'})/Org_{w'}, \forall w > w_0 \quad (4.1.1)$$

$$frac_w = change_w \times ((1 - m) + 2 \times m \times r), \forall w > w_0 \quad (4.1.2)$$

$$Aug_w = \begin{cases} Aug_{w'} \times (1 + frac_w), & \text{if } w > w_0 \\ d & \text{otherwise} \end{cases} \quad (4.1.3)$$

w_0 is the wavelength where the first reflectance value in the spectrum is measured. Equation (4.1.1) determines the change of reflectance value at w in Org and equation (4.1.2) determines a proportional change limited by the two constraints m and r , where r is generated randomly $\in [0, 1]$ and $m(\geq 0)$ is set beforehand. The proportional change is applied on $Aug_{w'}$ to get the augmented reflectance value at w in equation (4.1.3). Note that, by equation (4.1.2) the direction of change (upward or downward) from w' to w in Org remains the same in Aug . If $m = 0$, Aug is parallel to Org with the distance of initial deviation d .

step-2: (*Blending noise and continuum*)

In real hyper-spectral data often the presence of continuum and noises alters the absorption information stored in the spectrum. Therefore, the augmented spectra created in the previous step are mixed with random noise and continuum to create a more accurate reproduction of the real data, making our model capable of detecting characteristics in the real spectra. The random noise N is generated by randomly chosen values from a Gaussian distribution $\mathcal{N}(0, \sigma_N^2)$ and the continuum curve C is

predicted by a Gaussian curve $\Phi(w, 0.65)$, where the wavelength w is the position of the peak of the curve and is picked randomly within the selected range of the wavelengths. The noisy augmented curve $AugN$ is given by,

$$AugN =_{scaled} Aug \times_{scaled} (C + N) \quad (4.1.4)$$

The prefix *scaled* denotes a min-max scaling operation on the data. Note that, even though the augmented reflectance values are not entirely coherent with the original spectrum, that will affect the classification process due to the presence of continuum removal and standardization steps in the pipeline. Figure 4.4 graphically depicts the augmentation process.

4.1.2 Domain Collating

Supervised learning Models must have domain consistency between training and testing data. For this purpose, a predefined set of wavelengths is needed to be fixed as the domain for both training and testing data. In MICA library different minerals have spectra as a function of a different set of wavelengths (for example spectra of gypsum have 430 bands, alunite has 469 bands whereas bassanite has 480 bands). The fixed set of spectra to work on has been derived by unifying all the different wavelengths. Various curve-based interpolation techniques can be used to perform this task such as cubic, cosine, gaussian, and others. In this study, linear interpolation is applied to generate additional reflectance values, for the sake of simplicity and also for the negligible difference if more complicated interpolation methods were used.

It has been concluded in different studies that most of this absorption occurs in the wavelength range 1-2.6 micrometer Saranathan and Parente (2021b); Carter et al. (2013c); Lin et al. (2018). Though for some minerals a few distinguishable absorptions lie beyond this range, spectra are generally very prone to noises thus exhibiting additional drifts. To avoid models trained with unwanted features, a trade-off is made by compromising the effect of those distinguishable absorptions. From the interpolated 480 bands the 247 bands within the 1-2.6 micrometer wavelength range are selected to be used in the next pre-processing steps.

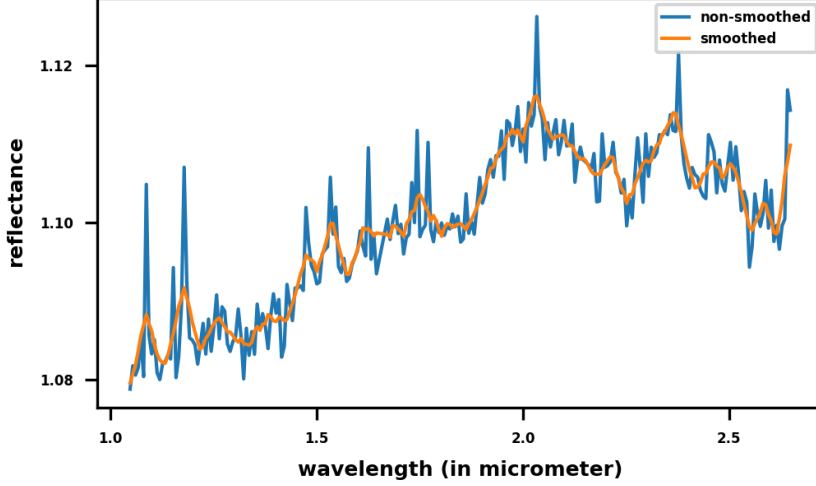


Figure 4.5: smoothed spectrum is generated by Savitzky-Golay filtering with window size 5 and order 2 followed by spike removal with $\omega = 5$ and $s = 0$

4.1.3 Spectra Smoothing

In CRISM hyperspectral data narrower bandwidth captures diverse energy that introduces the self-generated noise inside the sensors leading to spurious spectra both in the MICA library and MTRDR data. These small kinks remain present in each of the augmented spectrum replicas and can affect the generalization ability of the learning models. Hence, the following stage in the pre-processing procedure is to smooth each spectrum. Savitzky-Golay filter Gorry (1990), which is a frequently used smoothing technique appearing in various computational and optimization studies for years, increases the precision of the data without deforming the signal tendency. The trade-off to include the wide range of minerals reducing the noises blended with real data was given precedence, even if the Savitzky-Golay smoothing even with small window sizes is uncertain to preserve the doublet characteristics present in some uncommon phases. Moreover, the Savitzky-Golay filter, unfortunately, cannot remove the larger spikes from a spectrum; hence an additional spike removal step is necessary.

Let, SG is a smoothed spectrum and the coefficient of variation of it being cv_{SG} . Let a small window of size ω is moved across the set wavelength range such that cv_w^ω is the coefficient of variation and μ_w^ω is the mean of the available reflectance values within the window, w being the middle position of the window. Let $mean(cv^\omega)$ and $max(cv^\omega)$ respectively be the mean and the maximum of the coefficient of variations

of all such windows. The spike removal procedure is given by,

$$SR_w = \mu_w \text{ if } \frac{|mean(cv^\omega) - cv_w^\omega|}{max(cv^\omega) - mean(cv^\omega)} > s \quad (4.1.5)$$

where SR_w is the spike removed reflectance value at wavelength w and the parameter s regulates the spuriousity in the resultant spectrum. Figure 4.5 shows a sample result of the smoothing generated by Savitzky-Golay filtering followed by spike removal.

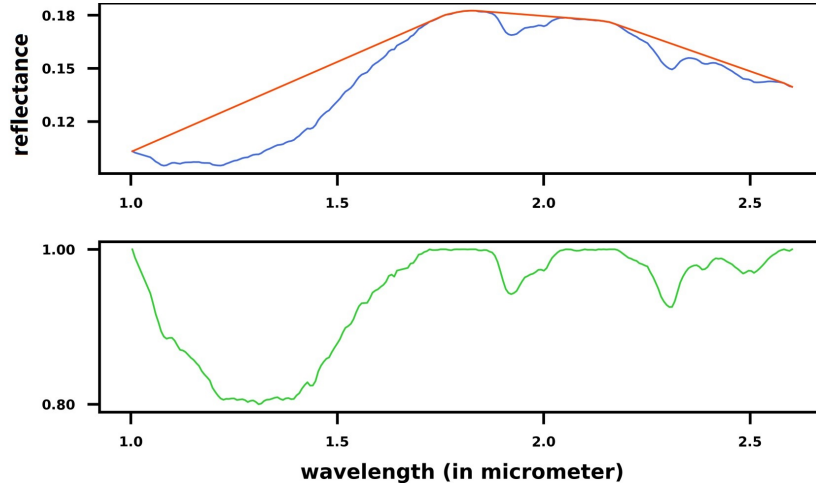


Figure 4.6: Top: sample spectrum in blue colour at the top image, its upper convex hull in red colour; Bottom: Continuum removed spectrum.

4.1.4 Continuum Removal

Even after atmospheric and photometric corrections on CRISM data, the spectrum contained in a pixel of an MTRDR image may be distorted by several factors like reflectance, radiance, and other environmental conditions producing a continuum, which alters some essential criteria for mineral identification, such as reflectance value, curvature tendency, the position of the absorption and others, making mineral identification much more difficult Parente et al. (2011). The Continuum-removing step focuses on eliminating these distortions and enhances the absorption qualities of the spectrum. Because continuum spectra are frequently convex or flat, the continuum is estimated by fitting an upper convex hull to the original spectrum Clark and Roush (1984a); de Berg et al. (2000). The ratio between the pixel spectrum and the value of its Upper Convex Hull (UCH) at the same wavelength has been calculated to remove the continuum from the spectrum [figure 4.6].

$$CR_w = Aug_w / CH_w$$

where at wavelength w , Aug_w is the original reflectance value, CH_w is the value of the upper convex hull around Aug , and CR_w is the value of the continuum removed spectrum.

While the applying UCH is a widely used approach for estimating the continuum line, it may not accurately capture subtle absorption features or handle potential variations in spectral signatures and overlapping features, which are critical for distinguishing between diverse mineral groups. To address this limitation, a more advanced technique called Segmented Curve Fitting (SCF) is introduced and discussed in detail in Chapter 5.

4.1.5 Spectra Standardization

Machine learning models based on gradient descent converge to the minima more quickly if the variance of the different features is high. Patterns in a spectrum emerge as absorptions positioned around specific wavelengths recorded in consecutive bands, implying that the features/bands are not fully independent of one another. Also, the continuum removal step ensures all the features in input data are in the (0,1] range, thus minimizing the variance. A standard scaler performed over the continuum removed data, by dividing a spectrum by its standard deviation, and establishes the mean at 0 and the standard deviation is 1 for each spectrum. This improves its absorption characteristics even more [figure 4.7], and speeds up the learning process. As an alternative process, row normalization can be performed with a min-max scaler.

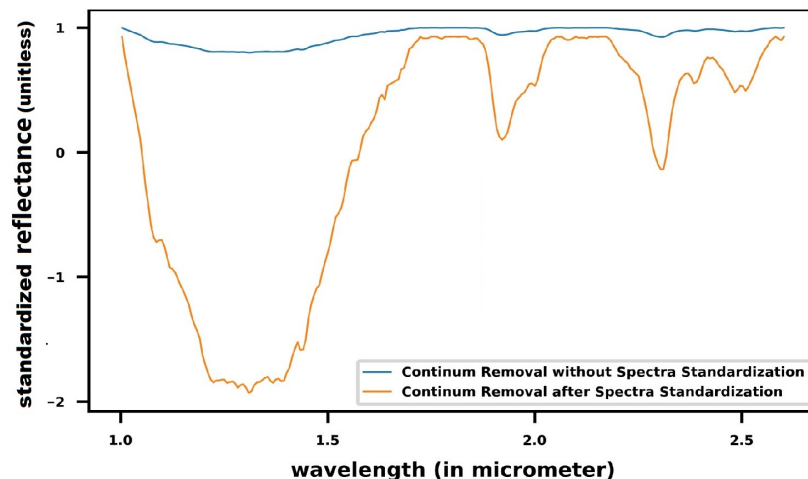


Figure 4.7: Visualization of the effect of standardization on a spectrum

4.1.6 Absorptions Extraction

Though supervised models are well-known for discovering hidden patterns in data on their own, they are referred to as black-box models because it is unclear which patterns are prioritized; this manifests the fact that there is no certainty over its acceptable performance on delicate test data. On the other hand, feeding the possible patterns more distinctively to the learning models imposes more control over the models' performance. To say precisely, though it is an additional challenge for the designers to generate more sophisticated feature values, it provides more control over the model outcome.

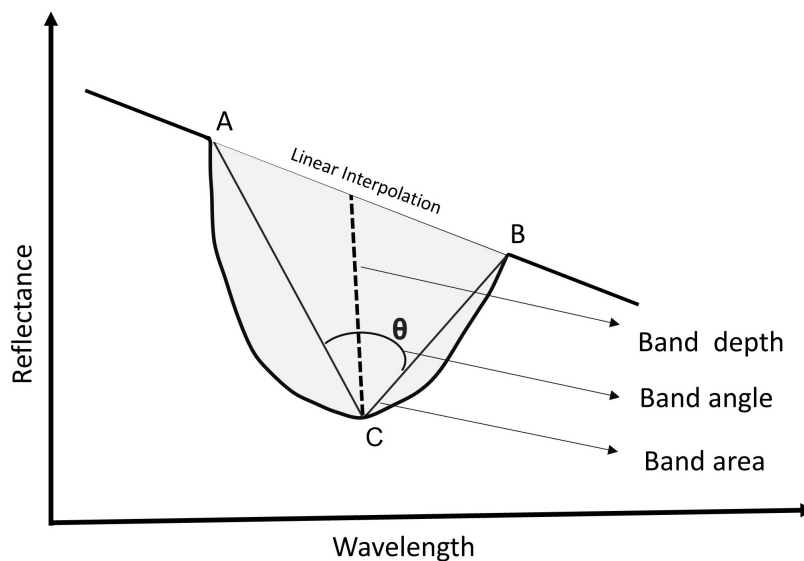


Figure 4.8: Illustrations of band-depth, band-angle and band-area. The thick line depicts the spectrum. A and B are the two end points of the absorption and C is the point with the lowest reflectance between them.

A section of a spectrum known as an absorption band is made up of reflectance values from a group of nearby wavelengths, with the lowest reflectance value occurring in the middle of the wavelengths (C point in figure 4.8) and all reflectance values before it having a negative slope and all reflectance values after it having a positive slope. The endpoints of the absorption band are the points where the slope changes (A and B points in figure 4.8). Following are some of the well-used absorption features in literature Pelkey et al. (2007):

- **band-depth:** If the endpoints of the absorption band are interpolated, the depth of the lowest point from the interpolation line is referred as the band-depth (dashed line in figure 4.8) .

- **band-angle:** This is the angle between the lines connecting the lowest point with the endpoints (θ in figure 4.8).
- **band-area:** This is the total area covered by the absorption band and the interpolated line and is estimated by the summation of depths of all the points in the absorption band from the interpolated line (grey-coloured area in figure 4.8).

In a continuum removed and standardized spectra S the band-depth at a particular wavelength w within a wavelength range w_s to w_t is calculated by

$$D = S_w^{[w_s, w_t]} - S_w \quad (4.1.6)$$

where $S_w^{[w_s, w_t]}$ is represents a linear interpolation between w_s and w_t with corresponding processed reflectance values, w being a wavelength within the range and S_w is the processed reflectance value at w . The band-area within this range can be estimated by

$$A = \sum_{\forall w \in [w_s, w_t]} (S_w^{[w_s, w_t]} - S_w) \quad (4.1.7)$$

Note that, by definition (4.1.6) and (4.1.7), on a spectrum for a specified range these values can be negative.

Here a new idea is proposed to extract a set of absorption features from a spectrum. From all 31 numerator reflectance spectra, extracting the wavelength ranges with

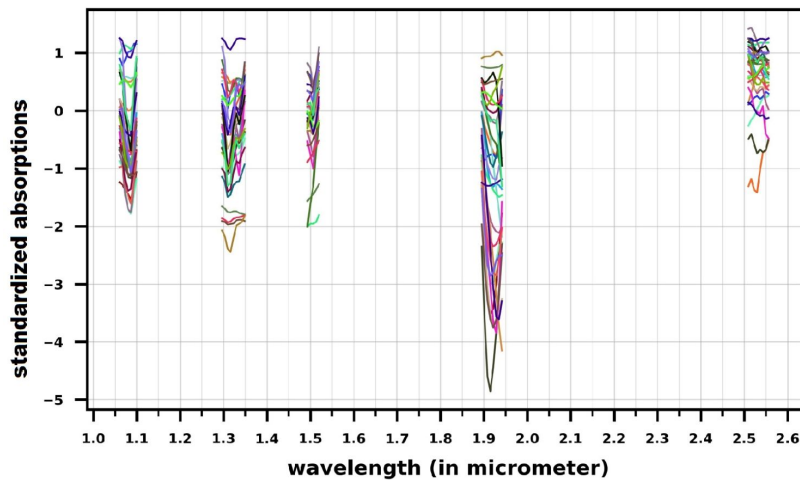


Figure 4.9: Visualization of sample wavelength ranges with high diversity in band-depths; Different colours showing the absorption bands in the different mineral spectra of MICA library.

higher diversity is the first task in this step, which is performed by identifying all shoulder points/ endpoints from each of the processed spectra available in the MICA library and considering ranges between every two consecutive endpoints in them. More than 350 absorptions of varying shapes with overlapping wavelength ranges have been retrieved. Then for each of the wavelength ranges in each numerator spectrum, band-area is calculated. The diversities in wavelength ranges are measured by the Average Absolute Deviation (AAD) of the band-areas.

$$AAD = \text{mean}(|X_i - \text{median}(X)|)$$

A new set of training data is derived by calculating band-depths in the processed spectra for a portion of the retrieved wavelength ranges with high diversities. As increasing the dimension is inversely related to the learning time in supervised models, and also makes the model prone to over-fitting, feeding a training dataset of a large number of features is avoided in such models. Figure 4.9 shows some example absorption bands with high diversity.

The pre-processing steps may not necessarily be performed in the same order as given in figure 4.3, as an example, performing augmentation after cropping and interpolation steps would reduce the run-time. However, reordering these steps does not have any evident effect on the performance of the learning models. The training data prepared by the discussed pipeline can be used to train the supervised learning models. The number of training classes in all learning models is 31, which corresponds to the number of mineral classes in the MICA spectral library. To generate the mineral map of an MTRDR data, the spectrum from each pixel is extracted and after applying the same pre-processing steps is evaluated by a model; the label is set on basis of the confidence given by the model for being a mineral class. An issue with supervised learning models is that the models are bound to classify each pixel to one of the mineral classes even if the pixel spectrum does not match with the mineral spectrum considerably, which often leads to misclassification. We set some confidence cut-off to be achieved by the model to get a pixel classified. For each pixel, the model gives a result of confidence by ensuing probability for each of the classes that are the minerals present in the MICA library. With the criterion imposed, a pixel is mapped to some mineral that has the highest confidence, only if the confidence value is more than 0.5 and the second-highest confidence is less than half of the highest confidence. If the condition

is failed, the pixel is marked as unclassified, though during performance measures, an unclassified pixel is considered a false negative.

4.2 Performance Analysis

In this section, the performance of the proposed procedure is evaluated. The augmented data after applying the proposed pipeline is used to train three types of supervised learning models, which are deep learning-based approach Artificial Neural Network (ANN), binary classification-based approach Support Vector Classifier (SVC) and decision tree-based approach Random Forest Classifier (RFC). Moreover, the performances of these models are compared with that of a shallow Convolutional Neural Network (CNN) model that is trained by the augmented data pre-processed until the spectra standardization step. Applying convolutions to the domain of extracted features is ineffective because a CNN model learns the absorption characteristics on its own using convolutions that rely on the resemblance of the reflectance values at the consecutive wavelengths. The purpose of using the different supervised learning models is to show the automated framework can perform with any of them with regard to the pre-processing pipeline proposed in the previous section.

The experimental setup, which covers the description of the test data, parameter tuning of the learning models, and selection of an ideal set of parameter values for the pre-processing pipeline, is first described. Then, through an uncertainty analysis, the significance of each step of the pipeline is demonstrated. Finally, the performances of these models are compared with some of the previously used methods for mineral classification in martian data. The codes for all the experiments and results presented here can be found online at Soor (2023b).

4.2.1 Experimental Setup

4.2.1.1 Data Specifications

Recently Plebani et al Plebani et al. (2022) published a collection of labelled pixels from 77 different TRDR images from various locations on the Martian surface in the wavelength range 1 to 3.47 micrometer, that were labelled using a hierarchical Bayesian model for estimating distributions of spectral patterns, and can be used as a

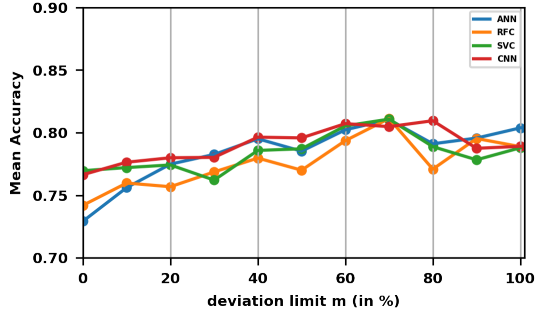
basis for nonlinear noise removal, or as training data for mineral classification models as well as for validating the models that use TRDR or MTRDR data for training. The dataset contains a total of 592413 spectra with 39 different labels including the spectra for artifacts and some bland pixels, of which 28 labels are similar to MICA library. We analyzed the performance of our model with these 28 labels, taking randomly sampling 500 spectra from each label, and repeating the occurrence of some spectra for the labels where less than 500 records are present in the dataset. Note that, the supervised models used in this performance analysis, i.e, CNN, ANN, RFC, and SVC are trained by the dataset augmented from MICA spectral library and tested on this data, whereas, all the other methods mentioned in this section are both trained and tested on this data by k-fold cross-validation.

Table 4.1: Different parameters set in the pre-processing pipeline

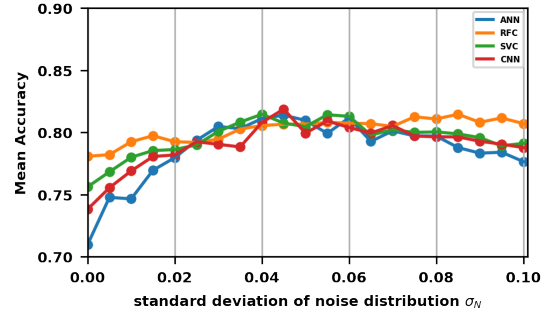
pre-processing	parameters
Augmentation	No. of replica per class: 1000 Deviation limit (m): 0.7 Standard deviation of Noise (σ_N): 0.045
Domain Collating	All the available wavelengths within the range 1-2.6 micrometer in MICA library
Smoothing	Savitzky–Golay filter: window-size: 11, order: 2 Spike Removal: window-size (ω): 5, s: 0.5
Absorption Extraction	diversity criteria: band-area feature: band-depth No. of features: 100

4.2.1.2 Pre-processing parameters

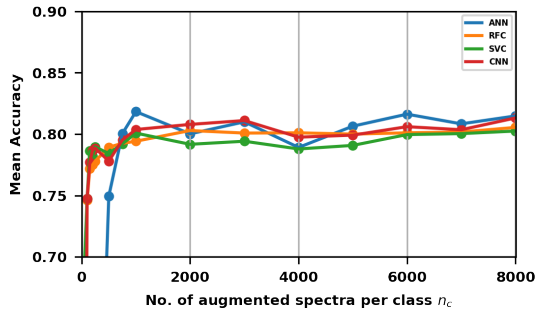
The correctness of the models how depends on the different parameters used to produce training data are discussed here. The plots presented in figure 4.10 show that mean accuracy around or more than 0.8 was frequently attained by using particular values for the different parameters like deviation limit (m) and standard deviation of noise distribution (σ_N) to generate the randomness within an augmented spectrum and the number of augmented spectra for each mineral class (n_c) and the number of extracted features (n_E). Each of the plots in figure 4.10 shows the change in mean accuracy with respect to the change in one of these parameters, where other parameters are constant. Figure 4.10a and 4.10b show that the optimum result can be generated if m



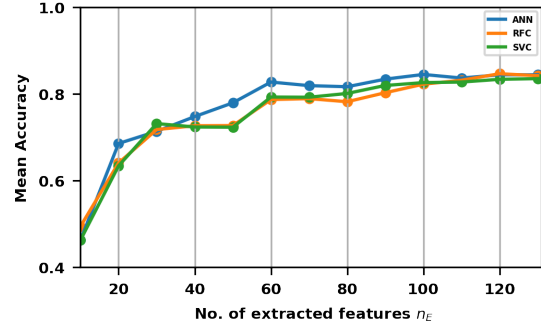
(a) $\sigma_N = .05, n_c = 1000$ and $n_E = 100$



(b) $m = .6, n_c = 1000$ and $n_E = 100$



(c) $\sigma_N = .05, m = .6$ and $n_E = 100$



(d) $\sigma_N = .05, m = .6$ and $n_c = 1000$

Figure 4.10: Change in mean accuracy in the models with respect to the change in different parameter values. σ_N is the standard deviation of the noise distribution blended with the augmented spectra, n_E is the no. of absorption features extracted, and n_c is the no. of replicas for a single class in the augmented dataset.

and σ_N are set to around 0.7 and 0.45 respectively. From figure 4.10c and 4.10d it can be seen that increasing the size of the augmented dataset or the number of extracted features does not improve the performance significantly after a certain limit, which in turn helps to find a suitable upper-limit to both the parameters to restraint the run-time of the learning process. Table 4.1 summarises the various parameter settings that were utilised to produce the training data.

4.2.1.3 Model Specifications

4.2.1.3.1 CNN Model LeCun et al. (2015) CNN with 1-D convolutions operates in a multiscale manner from local to global which examines the information in the locally adjacent bands. In the case of mineral identification, spectra are matched based on position and the intensity of the absorptions. In test data, the position of the absorption patterns must occur in the same wavelengths or at negligibly different wavelengths to be classified within the same class of the training data. For this reason, minimal size of kernels and strides are used with 1-D convolutions at the convolution

layers of the model. With a vast set of tuning parameters available in the TensorFlow 2.0 package Abadi et al. (2015) sometimes it is tricky to get the best set of parameter values for a model. With the help of hyper-parameter tuning on each layer, the use of Leaky ReLU activation Xu et al. (2015) is validated in all but the last layer. SoftMax activation is applied in the last (output) layer. Loss function and optimizer are respectively, categorical cross-entropy and RAdam Han et al. (2018) with warm-proportion (similar idea to momentum in general neural network optimizers like Adam) is set to 0.2, and the learning rate is set to 1×10^{-5} . With multiple experiments, it is deduced that the best model performance occurs with batch size 60. The model is set with the network weights at the epoch of the best validation loss out of a maximum of 100 epochs. The hyperparameter specifications are listed below.

Activation Function	Output: SoftMax, Other: ReLU
Optimizer	RAdam, initial learning rate: 1×10^{-5}
Loss Function	categorical cross-entropy
Epochs and Batch-size	100 (maximum) and 60

The utilization of a low batch size aims to enhance the generalization ability of the model, while a low learning rate is considered to minimize the risk of overfitting.

◦ **Ablation study for the CNN model:**

To optimize the architecture, experiments were conducted with varying numbers of 1-D convolution layers (2, 3 and 4), each followed by a max-pooling and batch-normalization layer in sequence. The number of filters in the convolution layers was adjusted across experiments, while filter size and strides were kept constant at 5 and 1, respectively. In max-pool layers, the settings were fixed at 2 for both parameters. For each of the experimental architectures, the trained model with the lowest validation loss in the training process was considered for testing. The results in the table 4.2 demonstrate the Mean Accuracy (MA) of mineral identification with different configurations, showing that the architecture with 3 convolution layers, each with 32 filters (as shown in figure 4.11), achieved the highest MA. Note that, for this ablation study both the training and testing data are gathered from the labelled dataset provided in Plebani et al. (2022). This architecture having a reasonably small size (FLOPs) is considered for performance analysis in this study.

Table 4.2: Ablation study of the CNN Architecture

2 Conv1D layers			3 Conv1D layers			4 Conv1D layers		
#Kernels	FLOPs	MA	#Kernels	FLOPs	MA	#Kernels	FLOPs	MA
16-16	0.40M	90.1	16-16-16	0.51M	90.6	16-16-16-16	0.55M	88.0
32-32	1.39M	91.1	32-32-32	1.88 M	91.6	32-32-32-32	2.07M	88.8
64-64	5.11M	90.8	64-64-64	7.17 M	90.4	64-64-32-16	6.1M	89.7
64-32	2.65M	90.7	64-32-16	2.84M	91.4	64-32-32-16	3.22M	89.1
64-16	1.43M	91.4	64-32-32	3.14M	89.7	64-32-32-32	3.34M	89.8

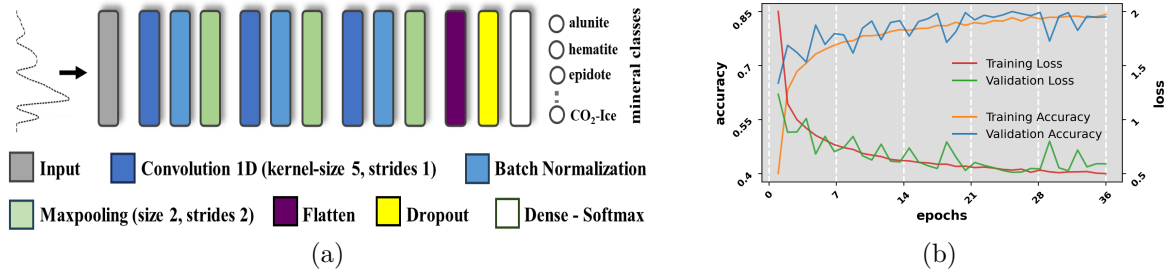


Figure 4.11: (a) The architecture of the best CNN model identified by the ablation study, (b) The accuracy-loss plot of the model during training

4.2.1.3.2 ANN Model Ojha et al. (2017) The Artificial Neural Network (ANN) features a straightforward architecture where the input layer corresponds to the feature domain size, and the output layer aligns with the number of classes. Intermediate dense layers connect all nodes with those in the preceding and succeeding layers. This model structure had three hidden layers and the output layer had 31 nodes corresponding to the 31 mineral classes. To mitigate overfitting and enhance generalization, batch-normalization and dropout layers are included in the model. In this study’s ANN architecture, each intermediate dense layer is succeeded by a batch-normalization layer, and a dropout layer precedes the output layer. The sizes of the dense layers are decreased gradually till the output layer and drop-out layers (drop value of 0.4) followed by batch-normalization layers were appended to the model structure, after each hidden layer [figure 4.12]. The node activation functions, loss function, and optimizer are set the same as the CNN model discussed above.

o **Ablation study for the ANN model**

The optimal architecture for the Artificial Neural Network (ANN) is determined through an ablation study. Different configurations, involving 2, 3, and 4 dense layers with different node counts (256, 512, or 768), are experimented with. Table 4.3 presents results for mean accuracy (MA) of mineral identification on the test dataset across these configurations. The findings demonstrate that the architecture featuring 3 dense layers,

with 768, 512, and 256 nodes respectively, attains the highest MA, and is selected for performance analysis in this study. Figure 4.12 illustrates its structure and accuracy and loss plots during the training process, indicating a favourable convergence. Here also the dataset provided in Plebani et al. (2022) is used for both training and testing of the models.

Table 4.3: Ablation study of the ANN Architecture

2 Dense layers			3 Dense layers			4 Dense layers		
#Kernels	FLOPs	MA	#Kernels	FLOPs	MA	#Kernels	FLOPs	MA
256-256	0.23M	82.3	256-256-256	0.36M	83.7	256-256-256-256	0.49M	80.2
512-512	0.72M	82.5	512-512-512	1.25M	84.8	512-512-512-512	1.78M	80.9
768-768	1.47M	83.1	768-768-768	2.66M	85.2	768-768-512-256	2.49M	82.4
768-512	1.06M	84.3	768-512-256	1.314M	86.9	768-512-512-256	1.84M	81.9
768-256	0.65M	84.2	768-512-512	1.59M	86.1	768-512-512-512	2.12M	83.8

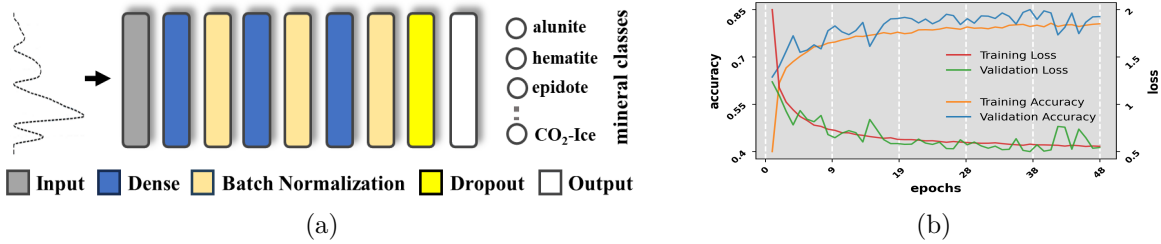


Figure 4.12: (a) The architecture of the best ANN model identified by the ablation study (Dense Layers' sizes: 758-512-256), (b) The accuracy-loss plot of the model during training

4.2.1.3.3 RFC Model Yanbin and Zhijun (2020) Scikit-learn library Pedregosa et al. (2011) provides a vast set of parameters to fine-tune the performance of a random forest. The branching criterion used in our model is based on the Gini impurity, where, when a dataset is randomly labelled, the probability with which each element is mislabelled is measured. The number of trees (estimators) is set to 100, which is used to fix the number of votes available in the ensemble learning process. No restrictions are set on the maximum depth of the trees to avoid impurity cases at the leaf nodes. Same way, no particular restriction is set on other branching factors like the minimum number of elements needed to split an internal node and the minimum number of elements needed to be a prediction node. The low correlation between the individual trees is ensured by using bootstrapping.

4.2.1.3.4 SVC Model Guo et al. (2019) A Support Vector Classifier is a binary classifier with hyperplanes acting as class boundaries which are often learned by using a kernel. The Regularization parameter, symbolized as C, puts a bound on the distance from the class boundary for each training example. When C is high, the optimizer selects a separating hyperplane with a smaller margin if that hyperplane can classify all of the training points more accurately, whereas, with a low value of C optimizer selects a separating hyperplane with a big margin to create a more generalized model. The best result was generated by setting radial basis function kernel and C (Regularization Parameter) as 1 using hyper-parameter tuning Pedregosa et al. (2011).

Table 4.4: Hyper-parameters for SVC and RFC models used in the experiment

RFC	number of estimators: 100 branching criteria: gini minimum samples in leaf: 5	SVC	pre-processing: PCA kernel: 'rbf' Regularization parameter (C): 1 tolerance: 0.001
------------	--	------------	---

Note that, learning the hyperplane classifier is largely a time-consuming process that increases with a higher number of features/dimensions in the data; hence a dimensionality reduction pre-procedure is a must-require before learning an SVC model. Principal Component Analysis (PCA) Alhayani and Ilhan (2017), a transformation applied for a wide variety of objectives that requires dimensionality reduction, is included in our model to fasten the learning process of SVC. Naturally, reducing the number of features in data affects accuracy; though, the objective of dimensionality reduction is to sacrifice some accuracy in exchange for simplicity as machine learning algorithms can learn the features more easily and quickly without having to deal with superfluous factors.

Table 4.4 provides a description of the different parameters set to fine-tune the learning models through numerous experiments in order to achieve the best outcomes. The confidence cut-off mentioned in the previous section is set upon all the models to generate the classification. CNN model is included only in this section to provide a comparison with the other models that use the data processed by the proposed feature extraction step, and those are the models used to generate the results in section 5.4.

4.2.2 Uncertainty Analysis of Pre-processing Pipeline

An uncertainty analysis is depicted in Table-4.5 that contains mean accuracy and standard deviation for the supervised models, calculated over multiple runs i.e., taking a different set of validation samples from the Plebani et al. (2022) data in each run. The accuracy is simplified by the total number of correct predictions ratioed to the total number of samples (i.e., 28×500). The pre-processing steps mentioned in each row of table-4.5 indicate the pipeline used in the same order as mentioned, for both the training data and validation data to calculate the corresponding evaluation value.

The pre-processing steps mentioned in section 4.1 are used for the uncertainty analysis. The mean accuracies of the models increase as the pipeline is extended by almost every pre-processing step. The improvement after the smoothing step is not much, which could be due to the exclusion of some weaker absorption signatures in the process of removing unwanted kinks from the spectra. Although the smoothing step alone does not significantly alter the accuracy, using it before the continuum removal stage results in higher mean accuracy. If spectra standardization is included in the pipeline, a significant increase in mean accuracy is observed. However, it is clear from the table that this improves the accuracy to an acceptable level when used in association with the continuum removal step. It can be concluded that, the pre-processing steps mentioned in the order in figure 4.3 yields the best combination for all the supervised models. The similar accuracy obtained by CNN that works on the standardized data, and the other models like ANN, RFC and SVC for which the absorption extraction step is included in the data processing pipeline shows the significance of the feature extraction step to use such supervised learning models.

4.2.3 Performance Comparison

Extensive research has previously been done on the use of probabilistic and unsupervised models for mineral identification in martian data. Allender et al. Allender and Stepinski (2017b) used OPTICS (Ordering Points To Identify Clustering Structure) algorithm to generate the first level of clusters, followed by the rare class discovery algorithm DEMUD (Discovery via Eigenbasis Modeling of Uninteresting Data) to identify mineralogical units of separate features and used a decision tree based on

Table 4.5: Mean accuracy with standard deviation calculated on the data from Plebani et al. (2022) with the pre-processing are noted for the supervised models

pre-processing	CNN	ANN	RFC	SVC
None	13.07 ± 1.0	19.71 ± 0.8	27.22 ± 1.4	07.23 ± 1.1
cr	26.70 ± 1.6	29.96 ± 1.2	27.48 ± 1.1	07.14 ± 0.4
cr+sm	29.05 ± 1.1	30.36 ± 1.6	25.25 ± 1.7	7.14 ± 0.1
cr+CR	51.23 ± 1.2	51.07 ± 0.1	37.77 ± 0.7	44.39 ± 1.2
cr+sm+CR	53.98 ± 0.5	51.73 ± 1.1	40.36 ± 0.5	44.50 ± 0.8
cr+sm+SS	70.82 ± 1.5	75.06 ± 0.1	66.66 ± 1.1	60.16 ± 1.3
cr+sm+CR+SS	81.68 ± 0.8	79.05 ± 0.9	76.21 ± 0.7	77.39 ± 1.3
cr+sm+CR+SS+AE	–	82.25 ± 0.5	79.67 ± 0.7	80.33 ± 0.3

cr: Cropped Spectra, sm: Smoothing, CR: Continuum Removal, SS: Spectra Standardization, AE: Absorption Extraction

different browse products to assign semantic labels to the identified mineral deposits in Full-Resolution Targeted (FRT) data. Bue et al. (2011b) applied a metric learning method using multiclass Linear Discriminant Analysis (LDA) to improve segment constancy to the classes of interest. Intending to identify some previously unidentified minerals Dundar et al. used the Partially Observed Hierarchical Dirichlet Process (PO-HDP), which uses a Dirichlet Process Mixture (DPM) to model each set of data and connects various groups of data by a higher level DP to create a hierarchy in the test dataset comprised of both identified and unknown samples and effectively classified the unknown samples by mapping to the known samples were having common ancestors in the hierarchy. The key advantage of this method is that it simplifies the process by automatically clustering data that don't fit into one of the observed classes, allowing verification after generating the initial clusters rather than at the sample level, as other anomaly detection methods do Dundar et al. (2013b).

Table 4.6: Mean accuracy and standard deviation of different models for the mineral groups in MICA library

Mineral Group	CNN	ANN	RFC	SVC	OPTICS	LDA	DPM
Primary silicates	85.42 ± 0.5	82.82 ± 0.4	81.70 ± 0.3	81.12 ± 0.5	68.80 ± 0.7	89.17 ± 0.4	77.80 ± 1.0
Ices	97.57 ± 0.4	90.29 ± 0.6	74.37 ± 0.2	81.52 ± 0.5	85.12 ± 1.1	94.31 ± 0.7	84.21 ± 1.6
Sulfates	85.44 ± 0.2	84.22 ± 0.2	86.25 ± 0.0	84.97 ± 0.2	68.48 ± 1.8	85.10 ± 0.5	76.07 ± 0.8
Phyllosilicates	78.13 ± 0.3	89.26 ± 0.3	88.60 ± 0.1	93.75 ± 0.2	71.21 ± 3.1	81.08 ± 0.7	69.81 ± 2.1
Carbonates	77.16 ± 0.7	73.39 ± 0.7	64.50 ± 0.9	62.20 ± 0.6	31.24 ± 1.2	69.54 ± 1.8	51.12 ± 2.0
Hydrated silicates	68.89 ± 0.4	69.42 ± 0.7	68.00 ± 0.5	65.32 ± 0.3	56.51 ± 1.6	79.91 ± 0.5	65.24 ± 1.6

The performances of the supervised models with previously specified parameter settings and trained on the augmented spectra controlled by the aforementioned parameters are compared with these models in table 4.6, where the mean accuracy and

standard deviation are measured over successful mineral-group classification. The mean accuracy and standard deviation are calculated by multiple runs with different sets of training and test data. The overall performances of the supervised models are as per the previously used methods, which proves the potential of the proposed framework. As carbonates, due to the C-O bond vibration overtones, have the same paired 2.3 and 2.5 micrometer absorption signatures that are used to identify phyllosilicates as well Viviano-Beck et al. (2014), the accuracy of carbonate detection is relatively low. Halides like epidotes are spectrally similar to phyllosilicate mixtures including calcite, chlorite, and illite with the major 2.34 and 2.25 micrometer absorptions and are only distinguishable by the presence of a minor band at 1.55 micrometer Viviano-Beck et al. (2014), and thus, the confidence of identification for halides could have been lower, resulting a bit lesser accuracy.

4.3 Geological information of study area for mineral mapping

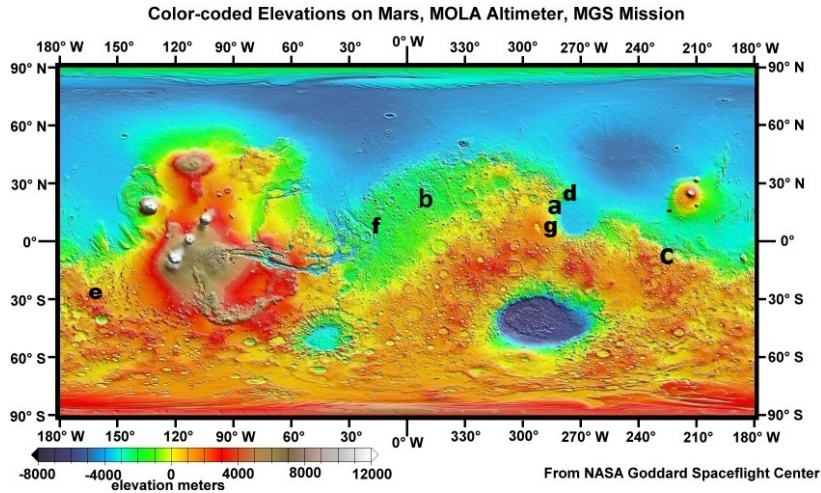


Figure 4.13: Mars Orbital Laser Altimeter-MOLA elevation Map Ferguson et al. (2018) where different locations are marked as follows. **a:** Jezero Crater, **b:** Mawrth Vallis, **c:** Gale Crater, **d:** Nili Fossae, **e:** Columbus Crater, **f:** Aram Chaos, **g:** North-East Syrtis

On Mars, the Syrtis Major quadrangle (which spans longitudes latitudes 0° to 30° north and 270° to 315° west) contains a cluster of massive lowlands known as the Nili Fossae. Olivines, smectites, hydrated silica, kaolinite, and iron oxides are the main minerals found in this area Hoefen et al. (2003); Edwards and Ehlmann (2015). It



Figure 4.14: False-colour images from different locations on Martian surface. These images are used for the experiments and results presented in section 5.4

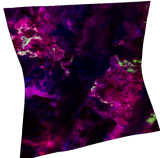
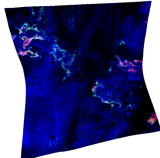
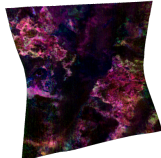
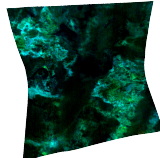
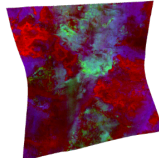
was chosen as a prospective landing location for the Mars 2020 rover in September 2015. Jezero crater, a huge impact crater of about 45-kilometer in diameter Fassett and Head III (2005) located in the Nili Fossae region, was in fact the landing site for the Mars 2020 mission, which sought to gather the deposit mineral samples that might be brought back to Earth for the first time ever by a future mission. It may therefore be used to compare and assess how the diversity of minerals evolves over time on a specific region of the Martian surface. For this region, the regions close to Jezero crater are thoroughly researched in literature to identify minerals and sediments. Mg-Carbonate, Fe/Mg-Phyllosilicates, Mafic minerals (Pyroxene and Olivine), and outcrops of Serpentine and Chlorite are the most common minerals found in the Jezero Crater region Saranathan and Parente (2021b); Farrand et al. (2009b). An MTRDR image, FRT93BE, from this region has been used in this study to describe the validation process in detail using browse products and absorption matching with library spectra. We also applied the proposed frameworks for mineral mapping in MTRDR data collected from several other regions of the Martian surface as well.

Mawrth Vallis is a 100-kilometer-broad hole that has been altered by many impact craters, many small streams, and volcanism. The visible and near-infrared spectrometers have been used extensively to study Mawrth Vallis. Some of the dominant minerals identified in earlier studies are Fe/Mg-Phyllosilicates, Al-Phyllosilicates, and High Calcium Pyroxene (HCP) McKeown et al. (2009); Wray (2013). Gale Crater is a 150-kilometer-wide impact crater that occurred near the early Hesperian time stratigraphic outline. Earlier studies have discovered extensive detections of mafic minerals and hydrated silicates in both bedrock and sediments, as well as temporal changes in water chemistry as evidenced by the presence of chloride salts Vaniman et al. (2014); Imanian et al. (2019). The 119-kilometer-diameter Columbus Crater on Mars is situated in the Terra Sirenum, a massive region in the southern hemisphere encompassing

latitudes 10° to 70° South and 110° to 180° West. An orbiting near-infrared spectrometer analysis has revealed that it contains layers of both clay, gypsum, and sulfates indicating the presence of fresh water and the possibility of life on the planet Wray et al. (2011). The 280-kilometer-diameter impact crater Aram Chaos is located in the Margaritifer Terra region of Mars. Hematite, jarosite, and hydrated sulfates are minerals that are frequently discovered in this area Glotch and Christensen (2005). Northeast Syrtis, a part of the Syrtis Major volcanic province in Mars’ northern hemisphere, has stratified terrain that is filled with a variety of igneous minerals, including olivine and high- and low-calcium pyroxene, as well as aqueous minerals, such as clay, carbonate, serpentine, and sulfate Murchie et al. (2009); Ehlmann et al. (2009b). Figure 4.13 shows the locations of the regions on the Martian surface from where the images used in the present study are acquired and figure 4.14 shows the false-colour images.

4.4 Results and Discussions

Table 4.7: Browse Products description of image FRT93BE

Carbonate Minerals		Phyllosilicate Minerals		Mafic Minerals
Browse Product: CAR	Browse Product: CR2	Browse Product: PHY	Browse Product: PFM	Browse Product: MAF
RGB channels: ○ MIN2295_2480 ○ MIN2345_2537 ○ CINDEK2	RGB channels: ○ D2300 ○ BD2500H2 ○ BD1900_2	RGB channels: ○ D2300 ○ D2200 ○ BD1900R2	RGB channels: ○ BD2355 ○ D2300 ○ BD2290	RGB channels: ○ OLINDEX3 ○ LCPINDEX2 ○ HCPINDEX2
Interpretation: ○ yellow/white: Mg-carbonate	Interpretation: ○ Red/Magenta: Mg-carbonate ○ green/cyan: Fe/Ca- Carbo.	Interpretation: ○ Red/Magenta: Fe/Mg-Smect.	Interpretation: ○ Cyan: Fe/Mg- Smect.	Interpretation: ○ Brown: Olivine ○ Blue/Magenta: HCP
				

FRT93BE image from Jezero crater depicts a high mineral diversity and serves as a better test for evaluating the performance of the proposed framework. The dominant minerals found by the supervised models in FRT93BE are Mg-Carbonate (bearing the Carbonate group of minerals), Fe/Mg-Smectite, or nontronite (bearing the Phyl-

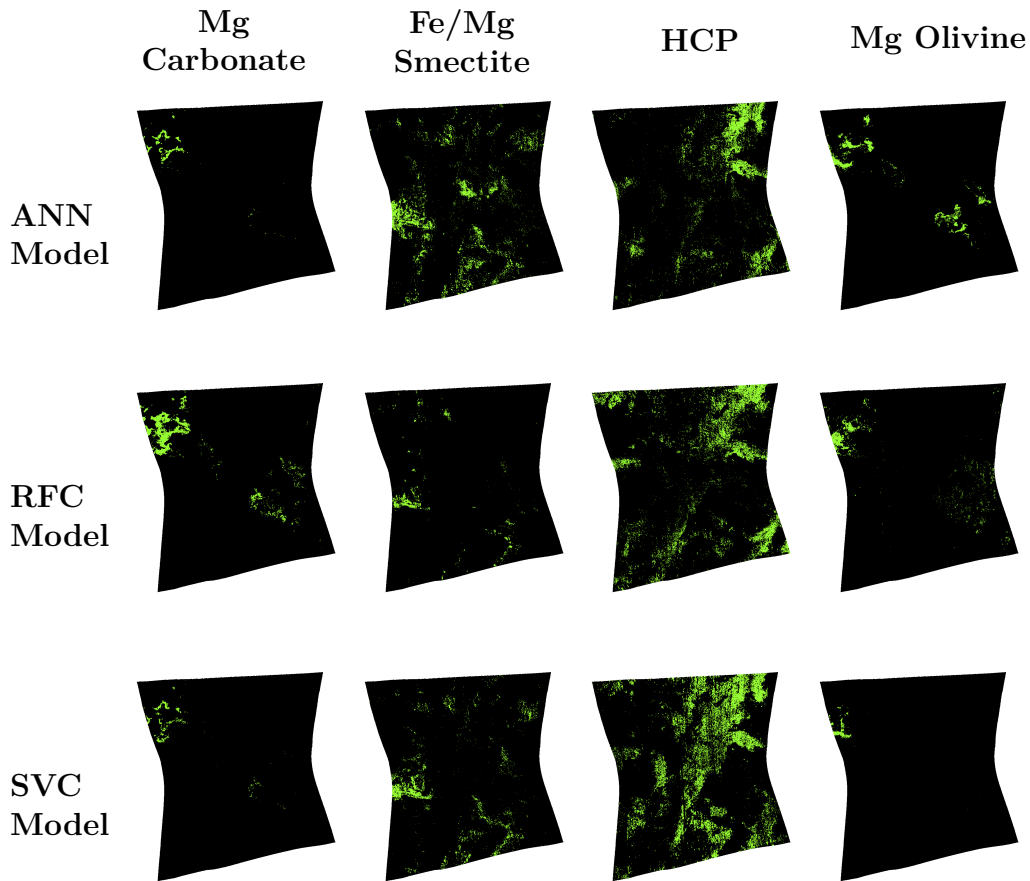


Figure 4.15: Classified pixels with in FRT93BE for the dominating minerals; Row-wise: Results of the supervised models; Column-wise: Detected minerals

losilicates group of minerals), HCP, and Mg-Olivine (bearing Mafic group of minerals) [figure 4.15]. Some other minerals outcrops such as plagioclase, serpentine, and chlorite are also detected in the image, but they are not considered for model evaluation.

Different false-colour composites, known as browse products, combine three RGB sets of thematically associated summary parameters to provide distinguished visualizations of the knowledge derived from the MTRDR image to identify the spatial distribution of minerals within a scene. Each browse product has its significance with its three-band components and colour interpretation. The information about the browse product used to identify each of the dominant minerals in FRT93BE is presented in Table 4.7.

Mg-Carbonate is more sensitive to subtle variability in the Carbonate group of minerals which has strong absorption near 2.3 and 2.5 micrometer and thus appear yellowish/white in CAR Browse Product; whereas CR2 browse product distinguishes Carbonate minerals tuned to the absorption features at 2.2-2.3 and 2.4-2.5 microme-

ter, thus differentiates between Mg-Carbonate and Fe/Ca Carbonate. The PHY and PFM browse products recognize patterns related to the cation composition of a hydroxylated and Phyllosilicate group of minerals. Indistinguishable Fe/Mg-Smectites appear in red/magenta colour in PHY product and cyan tinge in PFM product by considering hydration band of equivalent strength. The MAF Browse product gives knowledge associated with Mafic mineralogy. Both Fe-Phyllosilicate and Olivine have 1.0-1.7 micrometer bowl-shaped absorption in the MAF browsing product and can be visualized in red colour. HCPINDEX2 is sensitive to broad absorption at 2-micrometer Pyroxene and is less susceptible to false positives from other spectral signatures that display convexity centrally located at 1.3 and 1.5 micrometer. HCP appears in a blue/magenta shade in MAF composite.

In figure 4.15, the pixels classified as Mg-Carbonate, Fe/Mg-Smectite, HCP, and Olivine minerals in FRT93BE by ANN, SVC, and RFC models possess a solid resemblance with the corresponding regions as shown in Table 4.7. It is identified that the Carbonate-bearing mineral inside Jezero is more spatially diverse than previously detected.

Characterization of minerals can be validated using the MICA library based on their absorption features. The median spectra calculated from the set of labelled minerals in the image FRT93BE for each dominant mineral class by the supervised models are compared with the corresponding spectra in the MICA library to show that, both exhibit similar absorption features, which is shown in figure 4.16. Mg-Carbonates are characterized by combining 2.3 and 2.5 micrometer because of C-O bond vibration overtones, with Fe/Ca Carbonates dip concentrated at 2.33 and 2.53 micrometer and Mg abundant Carbonates shifted to 2.3 and 2.5 micrometer and hydration band at 1.93 micrometer Imanian et al. (2019). Nonetheless, these MICA spectra typically exhibit the same absorption at 1.93, 2.3, and 2.5 micrometer as the MICA library spectrum, shown in figure 4.16a. Fe/Mg-Smectites are a Phyllosilicate group of minerals that is more likely to be combined with Carbonates in a large abundance. Outside of Carbonate-bearing terrains, Fe/Mg-Smectites are identified by absorptions near 1.5, 2.3, and 2.4 micrometer which can be observed in figure 4.16b, where a 2.3 micrometer band center is consistent with Mg-rich Smectites Amador et al. (2018). Olivine has a wide absorption centered near 1.0 micrometer due to an increase in the content

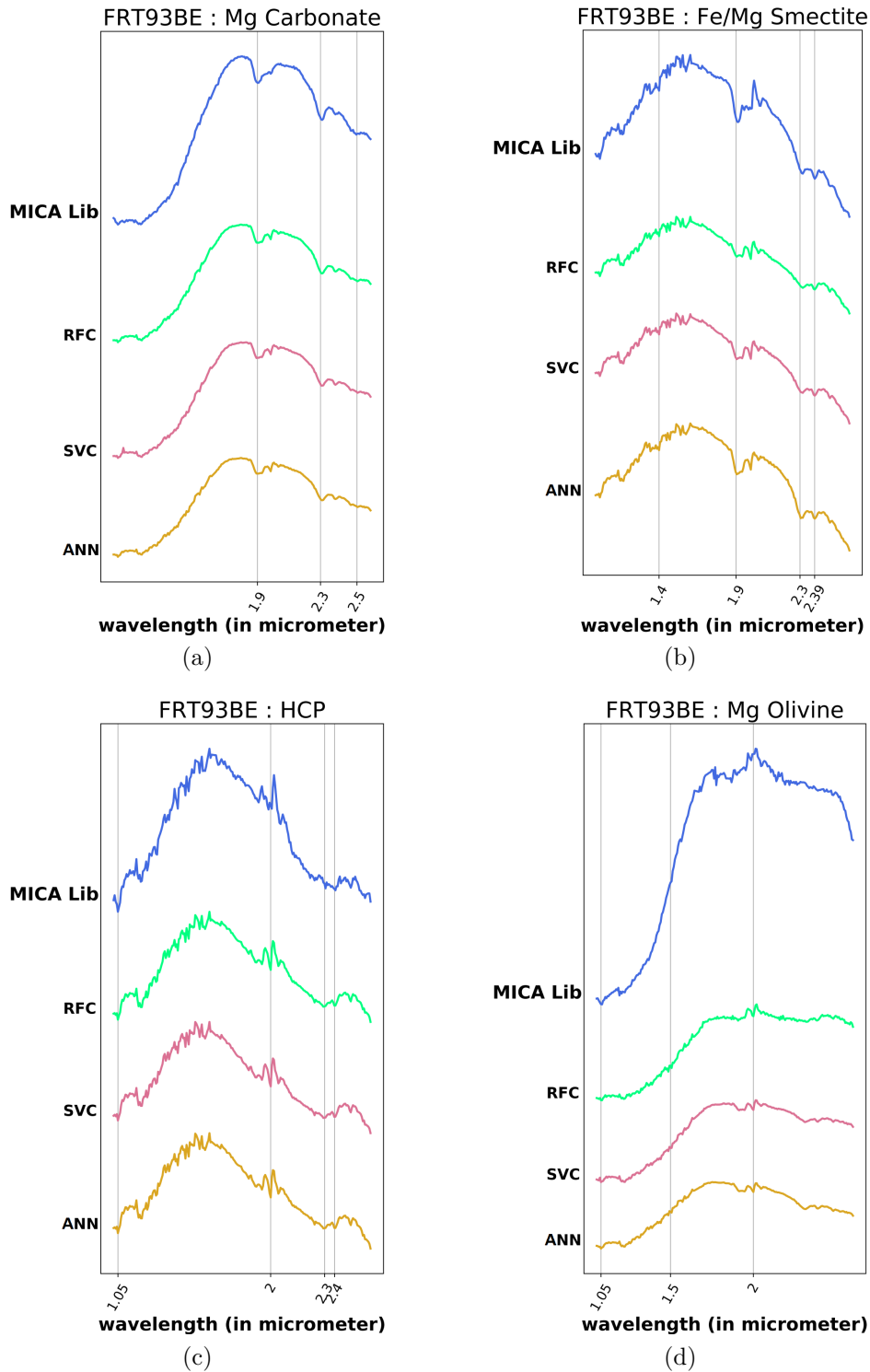


Figure 4.16: Absorption matching between median spectra of dominant minerals in FRT93BE and numerator spectra of corresponding minerals from the MICA library

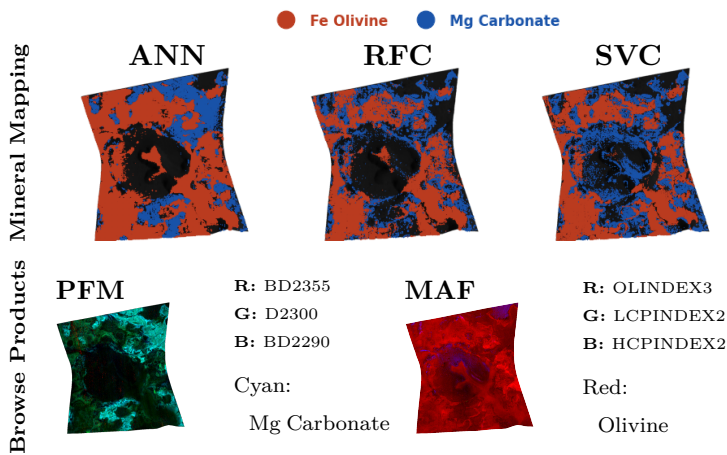
of iron, which automatically broadens and strengthens in-depth Viviano-Beck et al. (2014). Other absorptions to characterize Mg-Olivine mineral is 2.0, 2.4, and 2.5 micrometer, as shown in figure 4.16d. Pyroxenes (high-calcium and low-calcium) also

exhibit these features along with additional bands related to $\text{SiO}_{4/6}$ vibrational modes.

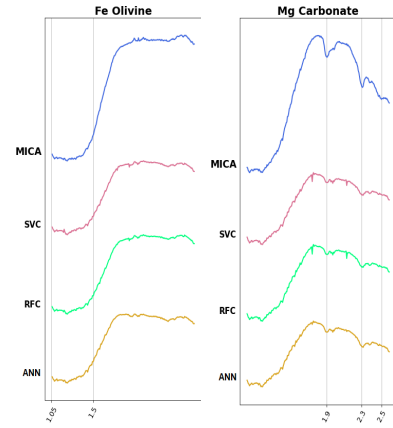
The discovery of minerals such as Mg-carbonate, Fe/Mg smectite, HCP, and Mg-Olivine in the FRT93BE CRISM hyperspectral image from Mars has significant implications for understanding the geological processes, environmental conditions, and potential resource exploration opportunities in the studied area. The presence of Mg-carbonate suggests past aqueous alteration processes, as carbonates typically form in the presence of liquid water and carbon dioxide. Fe/Mg smectites are clay minerals that form through the alteration of igneous rocks in the presence of water, providing evidence of past water-rock interactions. The formation of Mg-carbonate and Fe/Mg smectites implies the existence of past habitable environments with the presence of liquid water, potentially for extended periods. The presence of Mg-carbonate and Fe/Mg smectites also could indicate the existence of significant subsurface water reservoirs, which could be valuable resources for future human exploration and settlement on Mars. The stability of these minerals can provide constraints on the pH, temperature, and water chemistry conditions that existed during their formation. Mg-olivine and HCP are primarily igneous minerals, indicating the presence of mafic or ultramafic rocks, which can provide insights into the region's volcanic and magmatic history. Mg-olivine is a potential source of magnesium, which could be extracted and utilized for various purposes, such as construction materials or soil enhancement for future Martian agriculture. The identification of these minerals can help prioritize landing sites and regions of interest for future robotic and human exploration missions, as well as for resource prospecting and utilization.

A few additional results of the mineral mapping generated in the MTRDR images mentioned in the 4.3 section, along with the validation by the browse products and absorption matching are also presented here.

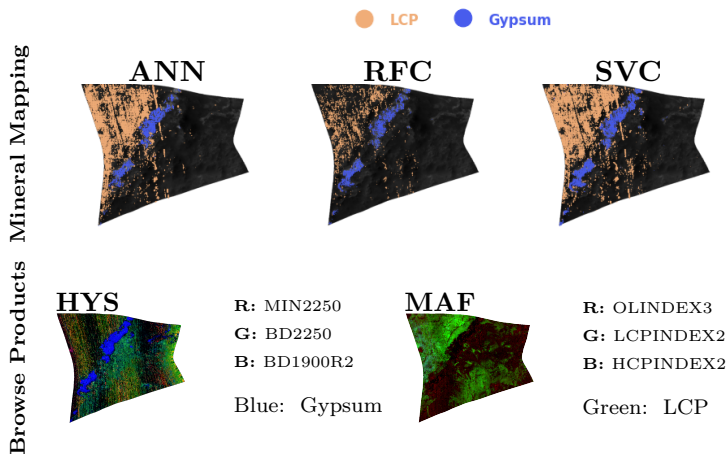
FRT3E12 (location: Nili Fossae)



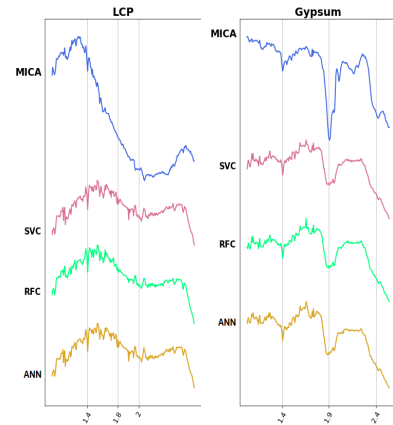
Spectra Matching



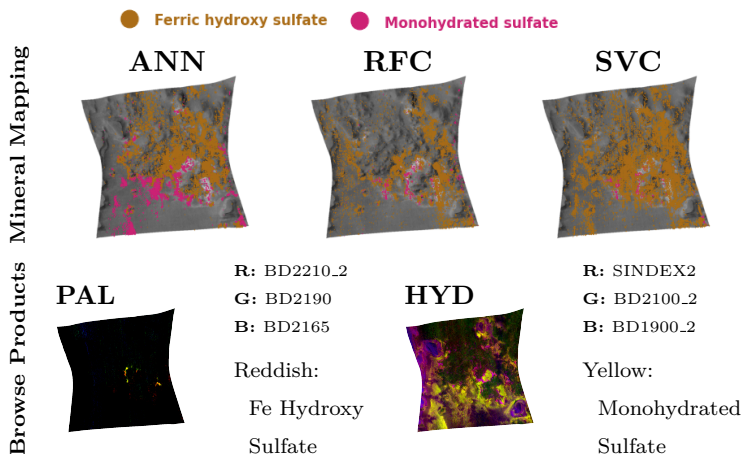
FRT131DF (location: Columbus Crater)



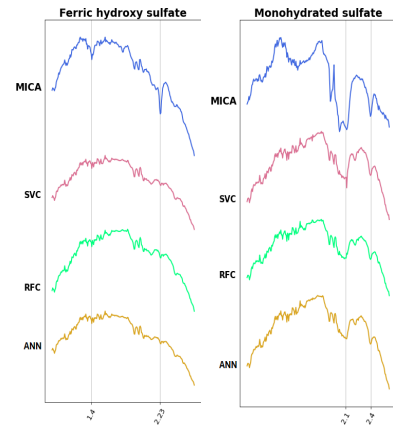
Spectra Matching



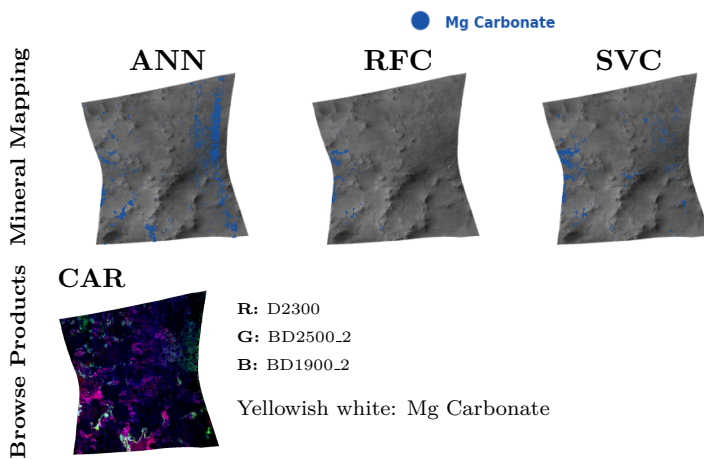
FRT98B2 (location: Aram Chaos)



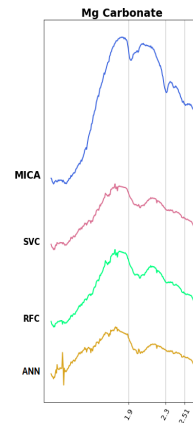
Spectra Matching



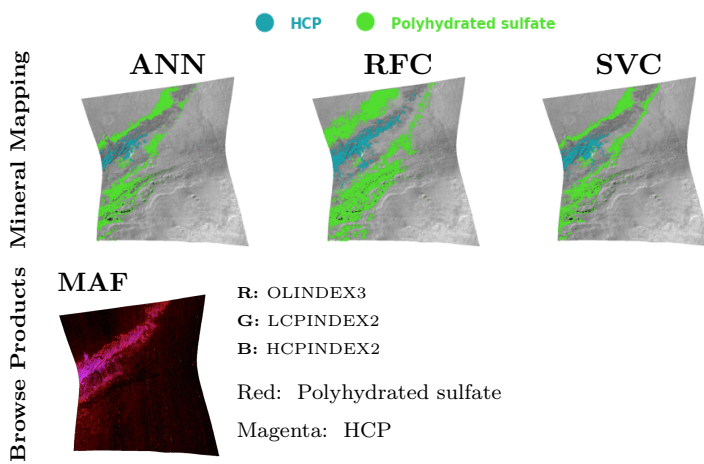
FRT19538 (location: NE Syrtis)



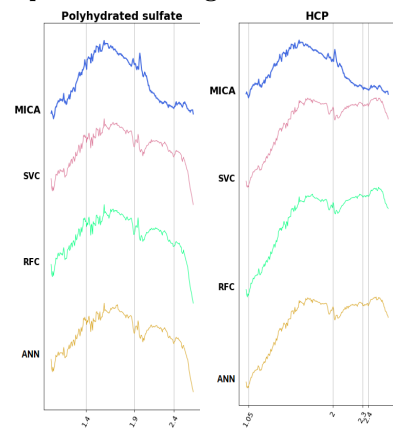
Spectra Matching



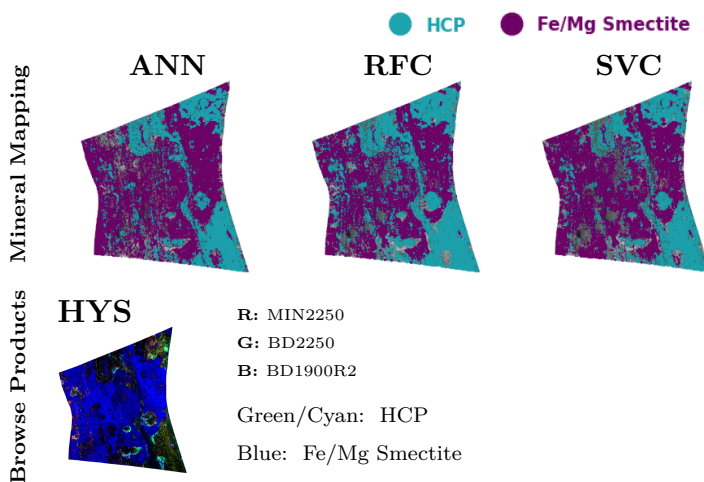
FRTC518 (location: Gale Crater)



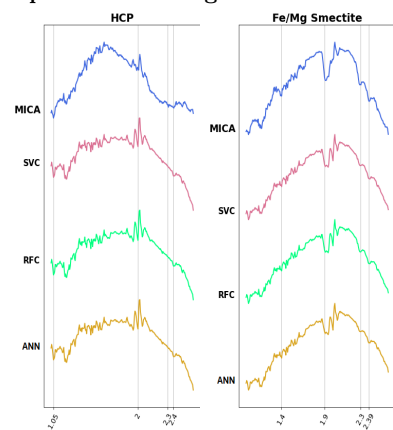
Spectra Matching



FRT9326 (location: Mawrth Vallis)



Spectra Matching



The minerals identified on the Martian surface exhibit a diverse array of diagnostic absorption features in the VNIR spectral range of 1 to 2.6 micrometers. Hydrated silicates, similar to Fe/Mg-smectites, show a combination of features, with a broad absorption around 1.4 micrometers due to OH stretching, a band near 1.9 micrometers from H₂O bending, and a feature around 2.2-2.3 micrometers associated with Al-OH and Mg-OH vibrations. Sulfates, such as gypsum, exhibit a suite of diagnostic features, including bands at 1.45, 1.75, 1.94, 2.22, and 2.48 micrometers, arising from combinations of H₂O stretching and bending, as well as SiO₄ stretching vibrations. Additionally, Fe-hydroxy sulfates and mono/poly-hydrated sulfates exhibit distinct absorptions related to OH, H₂O, and SiO₄ vibrational modes in this spectral region.

The detection of Fe-olivine and Mg-carbonate in the Nili Fossae region (FRT3E12) indicates the presence of mafic or ultramafic igneous rocks, providing insights into the region's volcanic and magmatic history, as well as potential aqueous alteration processes. The identification of gypsum and low-calcium pyroxene in the Columbus Crater region (FRT131DF) suggests the presence of sulfate-rich deposits, which could be indicative of past aqueous environments with specific chemical conditions. The presence of Fe-hydroxy sulfate and mono-hydrated sulfate in the Aram Chaos region (FRT98B2) also points to the existence of sulfate-rich deposits, potentially formed through the alteration of sulfide-bearing rocks or volcanic activity. The detection of Mg-carbonate in the NE Syrtis region (FRT19538) further supports the hypothesis of past aqueous alteration processes and the potential for habitable environments in this area. The identification of high-calcium pyroxene and poly-hydrated sulfate in the Gale Crater region (FRTC518) suggests the presence of mafic igneous rocks and sulfate-rich deposits, respectively, providing insights into the region's geological history and potential past environments. The presence of high-calcium pyroxene and Fe/Mg-smectites in the Mawrth Vallis region (FRT9326) indicates the presence of mafic igneous rocks and clay minerals, suggesting water-rock interactions and potential habitable environments in this region.

These findings highly contribute to our understanding of the geological composition, evolution, and potential past habitable environments in these regions, which is crucial for unraveling Mars' geological and potential biological history. They also highlight the importance of high-resolution spectral data and advanced mineral iden-

tification techniques in unraveling the mysteries of the Martian surface and paving the way for future exploration and habitation efforts.

4.5 Chapter Summary

- **Proposing a Robust Framework:** A comprehensive framework is proposed for mineral identification on the Martian surface. It ensures acceptable accuracy and can be effectively applied across diverse Martian regions.
- **Utilizing Supervised Learning:** The framework incorporates a supervised learning model. This model is trained using data obtained by augmenting spectra from the MICA spectral library. By leveraging this method, the framework gains a strong foundation for accurate mineral identification.
- **Effective Preprocessing Pipeline:** To address the complexities associated with CRISM data, a meticulous preprocessing pipeline is implemented. This pipeline not only tackles various challenges but also includes a novel feature extraction step. This step is compatible with advanced supervised learning models such as ANN, RFC, and SVC, enhancing the framework's precision.
- **Validation through Uncertainty Analysis:** The necessity of each step in the preprocessing pipeline is established through rigorous uncertainty analysis. This analytical approach ensures that every component is essential for accurate results. Additionally, the framework's effectiveness is verified by testing it with different types of supervised learning models, confirming its robustness and reliability.

In the next chapters, this study will be extended to enhance the performance of mineral identification. This will be achieved by implementing improved preprocessing steps in the pipeline, specifically by refining the continuum removal method. Additionally, a more advanced model, a DCNN architecture, will be utilized for more accurate and refined results.

Chapter 5

Segmented Curve-Fitting Method for Continuum Removal

A spectrum in a multiband remotely sensed image is generally a mixture of spectra of different materials present in the scene which can be distinguished by distinct absorption signatures. A mixed spectrum possesses a smooth baseline shape, known as a continuum, that masks the individual spectral features. Continuum can also appear due to instrument artifacts and topographic illumination effects. Eliminating the continuum from a spectrum being analyzed and correctly identifying its unique absorption characteristics are crucial for material identification, traditionally achieved by the Apparent Continuum Removal (ACR) methods like using an Upper Convex Hull (UCH). Nevertheless, most of these methods struggle when baseline curvature exceeds certain limits, often combining distinct absorptions. In this chapter, a new ACR technique called *Segmented Curve-Fitting* (SCF) is proposed, which requires no prior information about the spectrum but excels in accurately extracting distinct absorptions, even in the presence of significant curvature. The performance of SCF is compared with UCH and a few other ACR methods previously used in literature, using a collection of simulated data of varying complexity as well as the real CRISM TRDR hyperspectral dataset Plebani et al. (2022) used in previous chapter. Furthermore, an SCF-based mineral identification framework demonstrates its effectiveness in identifying the dominant minerals on CRISM MTRDR hyperspectral data collected from different locations on the Martian surface. Hyperspectral imaging system can detect subtle changes in the reflectance spectrum that are indicative of the presence of

specific minerals or other materials, such as clay minerals, which are difficult to detect with other remote sensing techniques Chabrilat et al. (2002). Every material has its own spectral signature, which is a unique pattern comprised of the reflectance values on light intensity across different wavelengths. When the reflectances are captured by the hyperspectral imaging system, the individual spectral signatures of all the materials in a target area are combined and stored in the pixels of hyperspectral data. The superposition of the individual spectral signatures forms a smooth background intensity of the scene, which is known as the continuum in hyperspectral imagery Clark and Lucey (1984); Clark and Roush (1984b); Atkinson et al. (2008); Filippi and Jensen (2007); Kumari et al. (2023b). While some hyperspectral data exhibit relatively straightforward continuums that require no explicit handling, others contain complex and nonlinear continuums influenced by various factors, including scattering, atmospheric effects, or variations in sensor response Zhang et al. (2004); Woodcock and Strahler (1987) significantly affecting the global background shape of the spectra Zhao et al. (2015). Understanding and characterizing the continuum is important in hyperspectral image analysis, as it serves as a reference for identifying and analyzing individual spectral features.

To effectively capture large surface areas, a collection of hyperspectral images is often arranged into a mosaic format. While these images might contain similar material compositions, they may have different continuums. Distinct continuum characteristics can be observed across various regions within a single hyperspectral image too. Furthermore, some materials have complex spectral shapes making it challenging to distinguish them from the continuum Boesche et al. (2015); Neave et al. (2016). Because of this, continuums in a hyperspectral image are typically estimated pixel-by-pixel and are generally considered to be independent of continuums in nearby pixels Viviano et al. (2014b).

As the materials are identified primarily based on the positions and shapes of their absorption features in the spectrum, a simple distance-based similarity-matching is unsuitable as it considers the whole spectral domain. Additionally, the presence of continuum can alter the global shape of a spectrum, making the material identification more challenging even though the absorptions within the spectrum are preserved Parente et al. (2011). Figure 5.1a-5.1b presents a comparison between a sample Mg-

Smectite spectrum extracted from a CRISM TRDR image and the corresponding spectrum in the MICA library. This comparison highlights the distinct global curvatures of the two spectra, in addition to the differences in the scales of their reflectance values. After applying a normalization operation to align their scales, these variations in global curvatures become more apparent visually.

Continuum removal is often present as an essential pre-processing step in hyperspectral data analysis, serving two primary purposes: mitigating spectral baseline effects from environmental conditions and instrumental artifacts (Imposed Continuum Removal (ICR)), and also isolating the distinct absorption features in the spectrum (ACR). The choice of method depends on the specific requirements of the analysis and the characteristics of the data being analyzed. The ICR methods involve fitting a polynomial curve or a power-law model to the entire spectrum to estimate the spectral baseline assuming a functional form for the continuum Brown (2006). ICR can be more accurate when the continuum shape is known or can be assumed correctly. On the other hand, ACR methods involve identifying spectral regions without discernible features, assuming these as part of the underlying continuum. The continuum for the full spectrum domain is estimated by connecting the end-points of those blunt regions McCraig et al. (2017). Between a pair of consecutive blunt regions, there is an absorption feature. The endpoints of absorptions are termed as *shoulder-points*. In ACR continuums are commonly estimated using a hull over the spectrum, where the shoulder points are identified as the locations where the hull touches with the spectrum. The spectrum is either subtracted by or divided by the estimated continuum [eq. 5.1.1] to nullify the effects of the continuum. All the shoulder-points in a continuum-removed spectrum remain at the same level. Figure ?? illustrates the Upper Convex Hulls over the library and test Mg-Smectite spectra, with the corresponding continuum-removed spectra displayed in figure 5.1e, showcasing how absorption signatures are automatically extracted between pairs of consecutive shoulder points if the absorption size exceeds a threshold. On the other hand, figure 5.1f depicts the absorptions detected by the proposed method, showing a better similarity between the absorptions extracted from the library spectrum and the test spectrum.

An effective ACR method should be resilient to the variations in the continuum shape. Existing ACR methods in the literature offer distinct advantages and limita-

tions, broadly falling into two following categories:

i. Without prior information about spectra: Clark et al. proposed an approach employing an *Upper Convex Hull (UCH)* in Clark and Roush (1984b), as the continuums in hyperspectral images commonly exhibit a convex shape. In Clark and King (1987) a *segmented Upper Hull (SUH)* is used to estimate continuums of non-convex shapes. However, this hull restricts the change of slope at both sides of the global maximum. These two methods are still well-used in literature. In the methods described in Milliken and Mustard (2005); Rice et al. (2013), the spectrally uninformative portions are identified visually and the absorption shoulders, termed as pin-points, are determined at the extremities of each of such continuum portions. These are then stretched through the spectrum domain by linear interpolations to estimate the full continuum. This may not effectively remove the continuum from spectra with low-intensity signals. More recently Mielke et al. (2015) introduced a novel approach incorporating *scale-space filtered alpha hulls* and robust *Geometric Hull (GH)* for continuum estimation. In this method, initial shoulder points are identified using a lower hull, and iteratively additional shoulder points are detected within each identified absorption until convergence.

ii. With known positions of absorptions in spectra: With prior knowledge of the position of the absorption shoulders in Craig et al. (2008); Dunn et al. (2010) continuum is determined by connecting the shoulder-points by straight lines. The *piecewise cubic spline* Clark and Lucey (1984) method fits cubic curves between some preset points, not necessarily shoulder points on the spectrum. With prior knowledge of the endmembers, a similar method *reference spectral background removal* is applied in Zhao et al. (2015) to eliminate the global curvature in a mixed spectrum by simulating a background curve itself.

The traditional ACR methods, such as utilizing a UCH, perform satisfactorily within certain limits of continuum curvature. However, beyond these limits, they may struggle to accurately extract absorptions and may tend to merge distinct features into a single entity. In contrast, the ACR method introduced in this paper named Segmented Curve-Fitting (SCF), also operates without prior information about a test spectrum, but more effectively extracts distinct absorptions, even in the presence of significant curvature. Figure 5.1 provides an example where the extracted absorptions

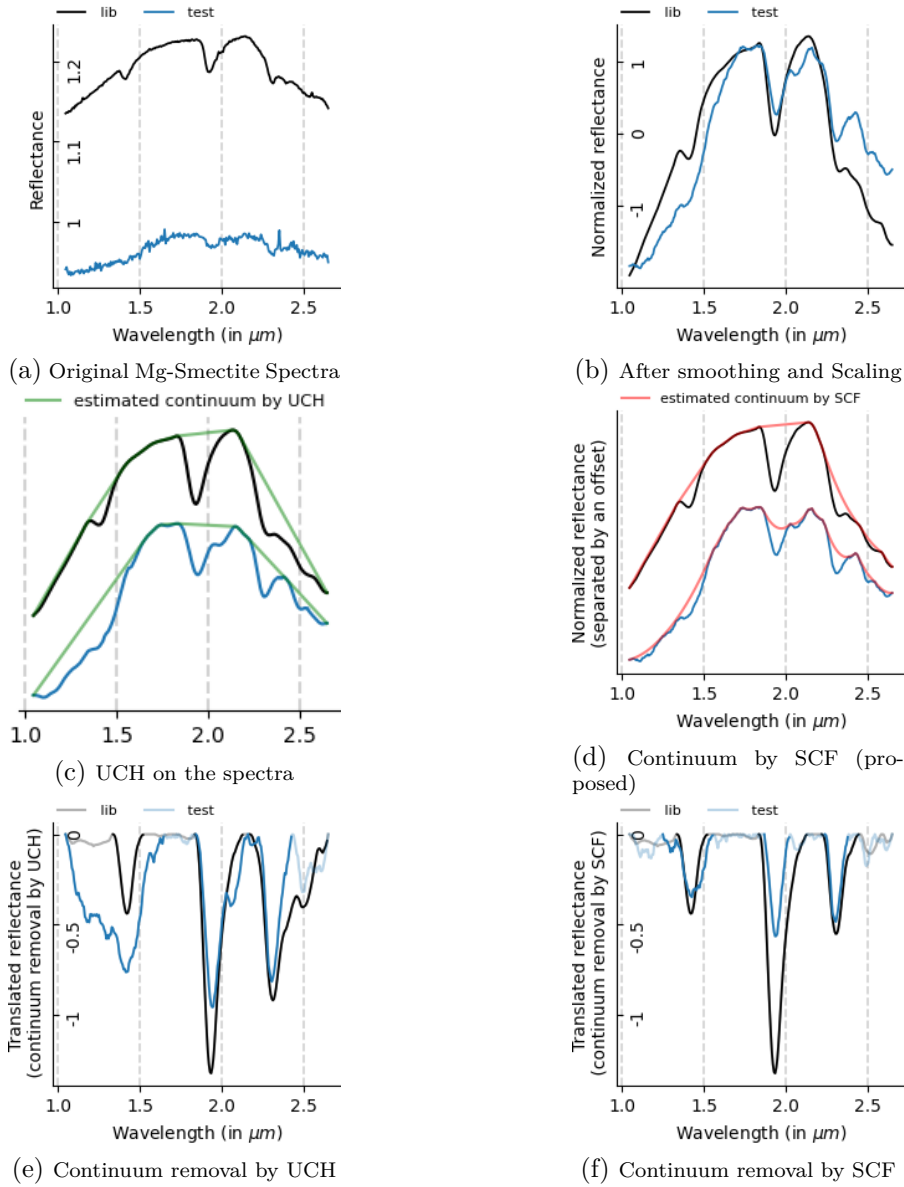


Figure 5.1: **(a)** Mg-Smectite spectra, with one sourced from the MICA spectral library and another from the CRISM TRDR dataset Plebani et al. (2022); **(b)** The disparity in global curvatures between the two Mg-Smectite spectra is noticeable after the scaling operation; **(c)** The estimated continua using Upper Convex Hulls (UCH) on the preprocessed library and test spectrum in (b); **(d)** The estimated continua by the proposed Segmented Curve Fitting (SCF) method; **(e)** Continuum removed spectra obtained by subtracting the UCH from the preprocessed spectra in (c); **(f)** Continuum removed spectra of the spectra in (b) by the proposed method SCF. In (e) and (f), extracted absorptions (considering those larger than a specific threshold) in the continuum-removed spectra are highlighted with darker colours. **Note-1:** The extracted absorptions in the continuum-removed library and test spectra by SCF in (f) exhibit more resemblance than those by UCH in (e). **Note-2:** The proposed SCF method directly determines continuum-removed spectra in (f) from the spectra in (b), without computing the estimated continua in (d). These are provided here for visual comparison only. **Note-3:** The figures in the top and bottom row are presented with actual scales on the y-axis, while those in the middle row have the same scale as in (b), although are separated by an offset for visual clarity.

in the continuum-removed library and test Mg-Smectite spectra by SCF show a better similarity than those achieved by UCH. In SCF, a set of initial shoulder points in the analyzed spectrum is determined first by the UCH, and then the derived segments are processed independently to extract more shoulder points. These second-level shoulder points are identified by fitting separate parabolic curves in the segments. The resulting continuum does not consist of straight lines connecting shoulder points like the usual methods; instead, it exhibits a parabolic shape between consecutive shoulder points, offering a more realistic estimation of the continuum. This approach although adapts a piece-wise approach like SUH, is not constrained by the limitations concerning the slope in the estimated continuum, thus providing a greater flexibility to handle both concave and convex shapes in any portion of the test spectrum. Also, the non-iterative approach, unlike GH, of the proposed method minimizes the risk of the estimated continuum over-fitting the spectrum and deducing a large number of small segments. Though different researchers vouch for using simple continuum removal techniques like UCH, the proposed method Segmented Curve-Fitting (SCF) separates the distinct absorption features present in a spectrum more accurately, and thus the segmented correlations between library spectra and a test spectrum are determined more correctly.

To establish the efficacy of SCF, it is tested on synthetic datasets with different levels of complexity prepared from Martian CRISM MTRDR hyperspectral data, although real data rarely possess this high error. SCF's performance is assessed in comparison to the other ACR methods UCH, SUH, and GH, which also does not require any prior information about the test spectrum, across various aspects, such as measuring the similarity between band-center positions and FWHMs (Full Width at Half Maximum) of different absorptions present in a test spectrum and its true label in a spectral library. Additionally, the accuracy of a mineral identification framework is evaluated, having continuum removal in the data preprocessing pipeline, with different classification methods like a CNN model or correlation matching. Finally some experimental results of the proposed method, i.e., the same framework described in chapter 4 with the continuum removal being done by SCF and the classification being done by WSSC is applied for mineral mapping in some of the MTRDR dataset used in 4 to provide a visual comparison of the obtained results.

5.1 Notations

A spectrum and its corresponding wavelength domain are represented as vectors denoted by bold lowercase letters. Consider a spectrum, denoted as \mathbf{r} , spanning the wavelength domain \mathbf{w} with wavelengths sorted in ascending order. The i -th element in \mathbf{r} and \mathbf{w} is represented as \mathbf{r}_i and \mathbf{w}_i , respectively. For a given wavelength w ($\in \mathbf{w}$) the corresponding element in the spectrum is $\mathbf{r}_{(w)}$. Similarly, for a wavelength portion \mathbf{w}' of \mathbf{w} (where \mathbf{w}' contains some consecutive wavelengths of \mathbf{w}), the corresponding spectra portion is denoted as $\mathbf{r}_{(\mathbf{w}')}$. A subset of a wavelength portion (which may not necessarily contain consecutive wavelengths) is denoted by \mathbf{w}'' , while a collection of such wavelength portions \mathbf{w}' is represented by \mathcal{W} . For set of wavelengths \mathbf{w}'' ($\subseteq \mathbf{w}'$ or $\subseteq \mathbf{w}$), the corresponding spectrum elements are denoted by $\mathbf{r}_{(\mathbf{w}'')}$. When a spectrum is not subscripted with an index, a specific wavelength, or a set of wavelengths, it indicates that the spectrum is considered for the entire wavelength domain. On the other hand, if a spectrum or a curve (let \mathbf{t}) is defined over a wavelength portion \mathbf{w}' only, rather than the entire wavelength domain, the spectrum is denoted with a superscripted \mathbf{w}' (e.g. $\mathbf{t}^{(\mathbf{w}')}$).

Let \mathbf{c} be an estimated continuum of \mathbf{r} , then the continuum removed spectrum can be calculated by the operation $\mathcal{C}_{\mathbf{c}}(\mathbf{r})$ using division or subtraction as given in eq. 5.1.1.

$$\begin{aligned}\mathcal{C}_{\mathbf{c}}^{div}(\mathbf{r}) &= \mathbf{r}/\mathbf{c} \\ \mathcal{C}_{\mathbf{c}}^{sub}(\mathbf{r}) &= \mathbf{r} - \mathbf{c}\end{aligned}\tag{5.1.1}$$

In this paper, if the removal method is not specified at the superscript level for a continuum removing function \mathcal{C} , it is assumed that both subtraction and division can be applied. Similarly, if a continuum \mathbf{c} is not specified at the subscript level, it is assumed that the continuum is estimated by an upper convex hull.

In section 5.2 while describing the proposed Segmented Curve-Fitting method three translated spectra \mathbf{t}^1 , \mathbf{t}^2 and \mathbf{t}^3 are utilized. Specifically, \mathbf{t}^1 is defined over the entire wavelength domain, while \mathbf{t}^2 and \mathbf{t}^3 are defined over specific wavelength portions. Furthermore, a fitted curve, denoted as \mathbf{p} is defined for each of these wavelength portions. In section 5.3.1.1, to construct synthesized datasets for performance evaluation, a noisy spectrum \mathbf{r}^n is created by imposing noise \mathbf{n} with \mathbf{r} across the entire wavelength domain.

The noise \mathbf{n} consists of three types of synthetic noises, specifically curvature noise denoted by \mathbf{v}^p , fluctuation noise denoted by \mathbf{f}^σ , and mixed-spectrum noise denoted by \mathbf{m}^k . The parameters p , σ and k associated with these noises are explained alongside other relevant notations in the section. Some additional notations are introduced in section 5.3.1.2 and 5.3.1.3 pertaining to different evaluation measures for assessing a preprocessed test spectrum \mathbf{t} in comparison to the corresponding preprocessed library spectrum \mathbf{l} .

5.2 Segmented Curve-fit for Continuum Removal

Since the form of the continuum in a hyper-spectral image is considered to have a convex curvature most often, the convex upper hull approach is typically used in literature. However, in reality, the structure of a continuum may not be confined to that and can unevenly affect distinct localized wavelength ranges in a spectrum. The suggested approach specifically addresses this issue by dividing the spectrum into multiple segments and predicting the shape of the continuum for each segment independently. Although this approach disregards the global pattern of the spectrum to some extent, the benefit of this approach is to enhance the weaker band-depths more precisely. The step-by-step process of the proposed method is now outlined in detail, with each step illustrated in figure 5.2 using a sample spectrum of H₂O-Ice from MICA spectral library Viviano et al. (2014b). Note that, a continuum removal method can also be applied on a pure spectrum too, to extract its distinct absorption signatures.

○ *Step-1 (Segmenting the spectrum):*

The first step of the proposed method is to extract the initial shoulder points from the spectra and by that determine the exclusive partitions in the translated spectrum, on which parabolic curves are fitted to extract more shoulder points and continuums are estimated for each segment. The Upper Convex Hull (UCH) method is used here for the initial segmenting of the spectra. An algorithmic outline for UCH function, UPPERCONVEXHULL(\mathbf{r}, \mathbf{w}), is given below which works in linear time. The same function is used in step-3 as well, to extract shoulder points from each of the initial segments.

Algorithm 1 Pseudocode to calculate the UCH

```

1: function UPPERCONVEXHULL( $\mathbf{r}, \mathbf{w}$ )
2:   initialize Empty stack  $\mathcal{S}$ 
3:    $\mathcal{S}.push(1), \mathcal{S}.push(2)$ 
4:   for  $i \in 3, 4, \dots, \mathbf{r}.length$  do:
5:     if  $\frac{\mathbf{r}_{\mathcal{S}_{-1}} - \mathbf{r}_{\mathcal{S}_{-2}}}{\mathbf{w}_{\mathcal{S}_{-1}} - \mathbf{w}_{\mathcal{S}_{-2}}} \geq \frac{\mathbf{r}_i - \mathbf{r}_{\mathcal{S}_{-2}}}{\mathbf{w}_i - \mathbf{w}_{\mathcal{S}_{-2}}}$  then
6:        $\mathcal{S}.push(i)$   $\triangleright \mathcal{S}_{-k}$  is the  $k$ -th element from top in  $\mathcal{S}$ 
7:     else
8:        $\mathcal{S}.pop()$ 
9:       if  $\mathcal{S}.length == 1$  then
10:         $\mathcal{S}.push(i)$ 
11:   return  $linear\_interpolation(\mathcal{S}, \mathbf{r}, \mathbf{w})$ 

```

In algorithm 1, *push*, *pop* and *length* are the general stack operations ? applied on the stack \mathcal{S} to insert an item at the top of \mathcal{S} , to extract/remove an item from the top of \mathcal{S} , and to determine the size of \mathcal{S} respectively. The condition in line 5 checks if the top element in the stack \mathcal{S}_{-1} stays on or at the negative side of the straight line connecting the second-top element \mathcal{S}_{-2} and $(\mathbf{r}_i, \mathbf{w}_i)$. The function *linear_interpolation* in line 11 interpolates between the indices of \mathbf{r} stored in the stack \mathcal{S} on the wavelength domain \mathbf{w} . Fig. 5.2(a) shows the example spectrum and its UCH. Fig. 5.2(b) depicts the continuum-removed spectra by the usual process, that is, dividing the spectrum by its UCH to obtain a translated spectrum, as

$$\mathbf{t}^1 = \mathcal{C}(\mathbf{r}) \quad (5.2.1)$$

Let m be the highest value in \mathbf{t}^1 ($m = 1$ for \mathcal{C}^{div} and $m = 0$ for \mathcal{C}^{sub} in eq. 5.1.1). A wavelength segment \mathbf{w}' characterized by lesser than m values between two m -valued wavelengths in \mathbf{t}^1 contains an absorption in \mathbf{r} , where the m -valued wavelengths at the two ends contain the shoulder-points of the absorption. Fig. 5.2(c) shows such spectrum segments of \mathbf{t}^1 for the example spectrum. When a parabolic curve $\mathbf{p}^{(\mathbf{w}')}$ is fitted through a spectrum segment $\mathbf{t}_{(\mathbf{w}')}^1$, by minimizing the quadratic error while ensuring it passes through the end-points of the segment, some points within the segment lie above this curve. If $\mathbf{t}_{(\mathbf{w}')}^1$ is divided or subtracted by $\mathbf{p}^{(\mathbf{w}')}$ to generate a translated spectra segment $\mathbf{t}^{2(\mathbf{w}')}$, translated points of those remain above the m level in $\mathbf{t}^{2(\mathbf{w}')}$ too. Now, on $\mathbf{t}^{2(\mathbf{w}')}$ another continuum removal operation can be performed

to extract more shoulder points.

Now, the parabolic curve can be fitted through various sets of points in a segment of \mathbf{t}^1 . The fitting points can be all the points in the segment, all the local maxima, all the local minima, or some points selected on some conditions. Alternatively, a lower convex hull also can be used for this purpose. As in the experiments better results are observed if the curves are fitted through the local maxima, in this paper all the local maxima are considered as the fitting points. By this, the method doesn't rely on specific thresholds for selecting the fitting points, making it robust across different types of data. Note that, in the example shown in figure 5.2, a detected segment around $2.6\mu m$ is not considered for further processing as it does not have any local maxima. Specifically, only the segments having at least one local peak are selected for further processing. The words 'maxima' and 'minima' in this paper indicate both singular and plural forms.

○ *Step-2 (Segment-wise fitting of parabolic curves)*

To obtain a functional form of the fitted curve, rather than the original spectrum, the translated spectrum is used, on which such parabolas facing the positive y-axis can exist as functions. Let \mathbf{w}' be a wavelength segment picked for further processing and \mathcal{W} be the set of all picked wavelength segments. Considering w_s and w_t as the two end-wavelengths of \mathbf{w}' , the general equation of the parabolic curve fitted in \mathbf{w}' becomes

$$\mathbf{p}_{(w)}^{(\mathbf{w}')} = a(w - w_s)(w - w_t) + m \text{ for } w \in \mathbf{w}' \quad (5.2.2)$$

The value of a in 5.2.2 can be calculated from $\mathbf{t}_{(\mathbf{w}')}^1$ minimizing the quadratic error as following, where $\mathbf{w}'' (\subset \mathbf{w}')$ contains the wavelengths of the local maxima in $\mathbf{t}_{(\mathbf{w}')}^1$.

Let $p = (w - w_s)(w - w_t)$. Then the quadratic error $J = \sum_{w \in \mathbf{w}''} (\mathbf{t}_{(w)}^1 - ap - m)^2$.

With optimum fitting $\frac{\delta J}{\delta a} = 0$.

$$\begin{aligned} \implies & \sum_{w \in \mathbf{w}''} (\mathbf{t}_{(w)}^1 - ap - m)p = 0 \\ \implies & \sum_{w \in \mathbf{w}''} \mathbf{t}_{(w)}^1 p - a \sum_{w \in \mathbf{w}''} p^2 - m \sum_{w \in \mathbf{w}''} p = 0 \\ \implies & a = \frac{\sum_{w \in \mathbf{w}''} \mathbf{t}_{(w)}^1 p - m \sum_{w \in \mathbf{w}''} p}{\sum_{w \in \mathbf{w}''} p^2} \end{aligned} \quad (5.2.3)$$

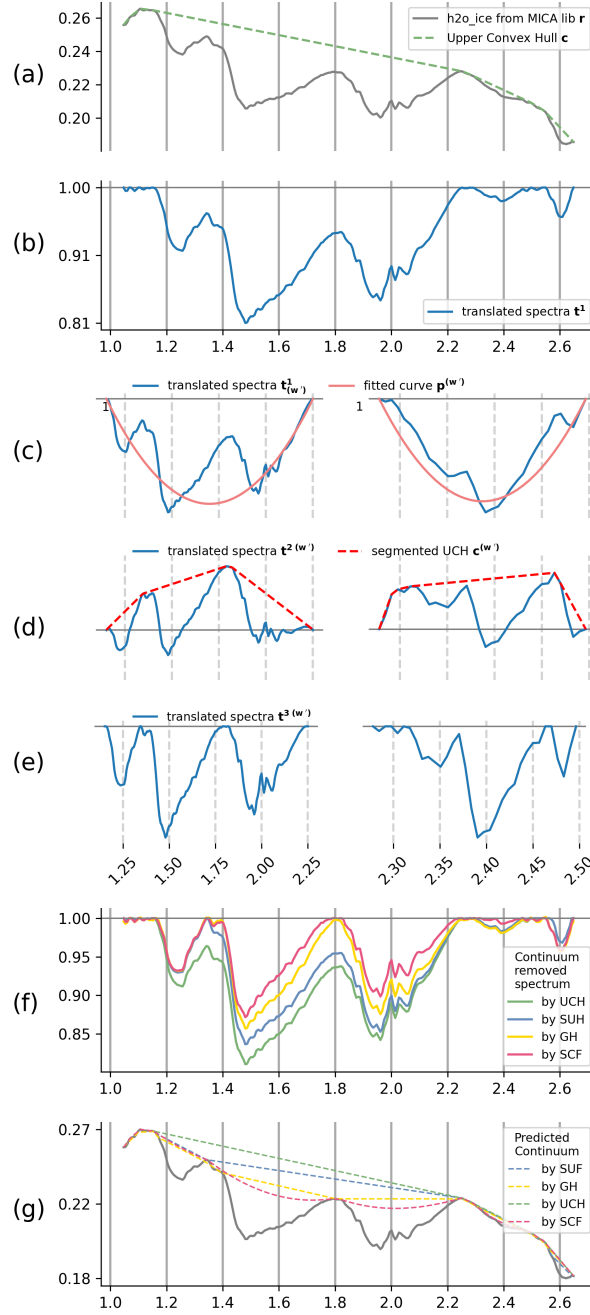


Figure 5.2: **(a)** H₂O-Ice spectrum R from MICA library and the UCH of it; **(b)** Translated spectrum t^1 using division method of eq 5.1.1; **(c)** segments are extracted from t^1 and parabolic curves as in eq.-5.2.2 are fitted; **(d)** Translated spectra $t^2(w')$ from 5.2.4 and corresponding UCHs; **(e)** Translated spectra $t^3(w')$ from eq.-5.2.5; **(f)** Merging the segments from t^3 s and the unchanged spectra portions from t^1 to get continuum removed spectra by SCF method. The continuum removed spectra by UCH, SUH and GH are also provided for visual comparison; **(g)** A visual comparison between the predicted continuums by the proposed method, UCH, SUH and GH. **Note-1:** X-axis represents the wavelength domain. The domain is same for the full spectra in (a), (b), (f) and (g), whereas the domain is same for the spectra segments in (c), (d) and (e). Y-axis in (a) and (g) represents the reflectance values in the input spectra, and the continuum-removed normalized spectra in the others. **Note-2:** Only the local peaks for each segment are used to fit the parabolic curves in (c), as these points could be new shoulder points or being part of the estimated continuum could be close to the new shoulder points in (d-e). **Note-3:** The ontinuum estimated by SCF in (g) has a parabolic shape between the new shoulder-points extracted in (d).

Fig. 5.2(c) shows the fitted curves for the different segments of the translated spectra.

○ *Step-3 (Segment-wise Translation)*

The next step is to calculate another segment-wise translation for all the segments \mathbf{w}' in \mathcal{W} that generates $\mathbf{t}^{2(\mathbf{w}')}$ from $\mathbf{t}_{(\mathbf{w}')}^1$ and $\mathbf{p}_{(\mathbf{w}')}$. To extract additional shoulder-points, another step of continuum removal is performed on each of the translated segments $\mathbf{t}^{2(\mathbf{w}')}$ by UCH.

$$\mathbf{t}^{2(\mathbf{w}')} = \mathcal{E}_{\mathbf{p}_{(\mathbf{w}')}}(\mathbf{t}_{(\mathbf{w}')}^1) \quad (5.2.4)$$

$$\mathbf{t}^{3(\mathbf{w}')} = \mathcal{E}(\mathbf{t}^{2(\mathbf{w}')}) \quad (5.2.5)$$

Fig. 5.2(d) shows $\mathbf{t}^{2(\mathbf{w}')}$ and UCH for the selected segments, and fig. 5.2(e) shows $\mathbf{t}^{3(\mathbf{w}')}$ for each of these segments. Note that, to ensure continuity in the continuum-removed spectra, i.e., to keep all the shoulder-points on the continuum-removed spectrum at the same level, in all continuum removal operations (\mathcal{E}), employing the same translation method is necessary, that is, employing either only divisions or only subtractions.

○ *Step-4 (Merging the translated segments)*

The final step of the procedure involves combining the independently translated segments of \mathbf{t}^3 with the unpicked portions in step-2 from the initially translated spectrum \mathbf{t}^1 on the entire wavelength domain \mathbf{w} to generate the continuum-removed spectrum.

$$SCF(\mathbf{r}, \mathbf{w})_{(w)} = \begin{cases} \mathbf{t}_{(w)}^{3(\mathbf{w}')} & \text{if } \exists \mathbf{w}' \in \mathcal{W} \mid w \in \mathbf{w}' \\ \mathbf{t}_{(w)}^1 & \text{otherwise} \end{cases} \quad \forall w \in \mathbf{w} \quad (5.2.6)$$

Fig. 5.2(f) shows the continuum-removed spectrum by the proposed method, and in fig. 5.2(g) a visualization of the predicted continuum is given. The predicted continuum could separate almost all the prominent absorptions which the previous method was unable to.

The usual methods of continuum removal like UCH and SUH determine the continuum from the full spectrum first, then eliminate its effect from the spectrum by subtraction or division operation as given in eq 5.1.1; on the other hand, the proposed method directly removes the effect of the continuum from the spectra by eq 5.2.6 without estimating the continuum particularly, i.e., the continuum shown in fig.

5.2(g) is not needed to be computed to get the continuum-removed spectrum shown in fig. 5.2(f). The continuum-removed spectrum $SCF(\mathbf{r}, \mathbf{w})$ can be calculated in linear computational time, because, the initial segmentation in step-1 takes linear time, and the segments consist of distinct wavelength ranges which are processed further (eq. (5.2.3-5.2.6)) in linear computational time independently and each in linear time. Note that, while it may appear reasonable to limit the computation by considering only the local peaks from \mathbf{r} to further reduce the runtime, this approach would not be suitable for detecting the shoulder points correctly.

5.3 Performance Evaluation

To evaluate the performance of the proposed continuum removal method SCF, four datasets with different levels of complexity are used. The first three datasets are synthesized from the MICA spectral library, which was created by collecting spectral data from a variety of mineral samples using CRISM spectrometer from different locations of Martian surface Viviano et al. (2014b), and the fourth dataset is the recently released labelled TRDR spectra by Plebani et al Plebani et al. (2022). The datasets and the true spectra in the MICA spectral library undergo a preprocessing pipeline,

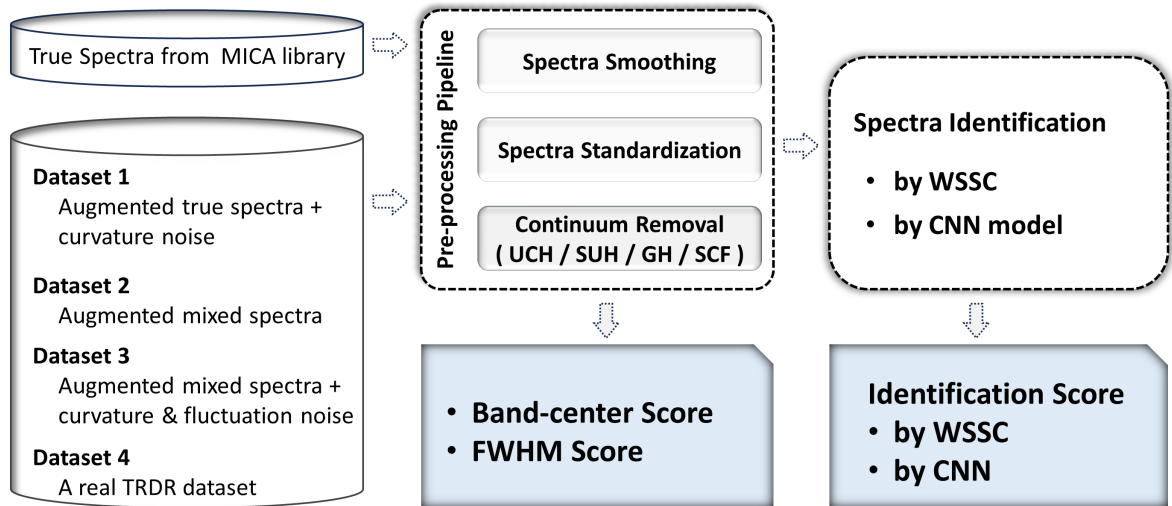


Figure 5.3: Four datasets with varying complexity and the true mineral spectra in the MICA library undergo the same preprocessing pipeline, to obtain the measures of misfit (the band-center score and the FWHM score) and the measure of identification (the identification score obtained once using WSSC, once using a CNN model). Different continuum removal methods including the proposed SCF method are used in this setup for a comparative performance analysis based on these evaluation measures.

that includes a continuum removal step. Finally, the following evaluation measures are generated.

- i. Band-center score
- ii. FWHM score
- iii. Identification score

The band-center and FWHM scores indicate the level of misfit (higher the score, lesser the misfits) compared to the true spectra, while the identification score assesses SCF’s applicability in material identification. SCF’s performance is compared with different state-of-the-art continuum removal methods by calculating the measures using those in the preprocessing pipeline. The identification score is calculated using two approaches, the first one, the Weighted Sum of Segmented Correlation (WSSC) utilizes a curve-matching procedure to calculate a matching index of a test spectrum to a library spectrum, while the second method employs a shallow convolutional neural network (CNN) model, providing insights into SCF’s performance across different genres of classification methods. Figure 5.3 outlines the performance evaluation procedure.

In the following, first, a detailed description of the synthetic data generation process is provided, along with a succinct overview of the real TRDR dataset and the preprocessing pipeline. Subsequently, it provides an in-detail explanation of the evaluation measures employed. The identification procedures, namely the WSSC method and the CNN model, are then outlined. Finally, the performance of the model is analyzed using the comprehensive results. All the related codes of this work are available at Soor (2023a).

5.3.1 Experimental Setup

5.3.1.1 Data Specifications

MICA spectral library contains 31 different mineral spectra from 6 mineral groups like Iron oxides and primary silicates, ices, sulfates, phyllosilicates, carbonates, and other hydrated silicates and halides. To recreate three different degrees of complex datasets that might be in accordance with real-life data, varying magnitudes of shape change

and noise are applied to the spectra of this library, also different spectra from it are mixed together to get the first three datasets.

5.3.1.1.1 Synthetic Data (dataset- 1, 2, 3) Primarily a random noise N is generated by the composition of the following.

- i. A curvature noise C , which is predicted by adding multiple Gaussian curves of $\Phi(w, 0.65)$, where the wavelength w is the position of the peak in a curve and is picked randomly within the selected range of the wavelengths. If p number of such curves are combined, the resultant curvature (Φ_p) can have a maximum p number of peaks.
- ii. A fluctuation noise N , which is predicted by randomly chosen values from a Gaussian distribution $\Phi(0, \sigma_N^2)$ for each wavelength of the spectra domain. If σ_N is higher, the noise fluctuation is higher.
- iii. A mixed-spectrum S formed by adding scaled spectra of a number of randomly chosen different minerals other than the mineral to which noise is put. The primary mineral is combined with all of the other minerals in a 60-40 ratio. S_k denotes the mixed-spectrum with $k(\geq 0)$ secondary spectra, where S_0 indicates no other spectrum is mixed with the primary spectrum.

The general equation of spectrum R with noise is given by,

$$R^N(p, k, \sigma_N) = \textit{scaled}R + \textit{scaled}(C_p + S_k + N_{\sigma_N}) \text{ for } p, \sigma_N, k \geq 0 \quad (5.3.1)$$

The prefix *scaled* denotes a min-max scaling operation on the data. Note that, though the reflectance values in the generated spectrum are not entirely coherent with the original spectrum, that will not affect the evaluation process due to the continuum removal process applied to it. Following are the specification of the first three datasets.

dataset-1	dataset-2	dataset-3
$p = 1, 2, 3, 4$	$p = 0$	$p = 1, 2$
$k = 0$	$k = 1, 2, 3, 4$	$k = 1, 2$
$\sigma_N = 0$	$\sigma_N = 0$	$\sigma_N = .01, .02, .03, .04$

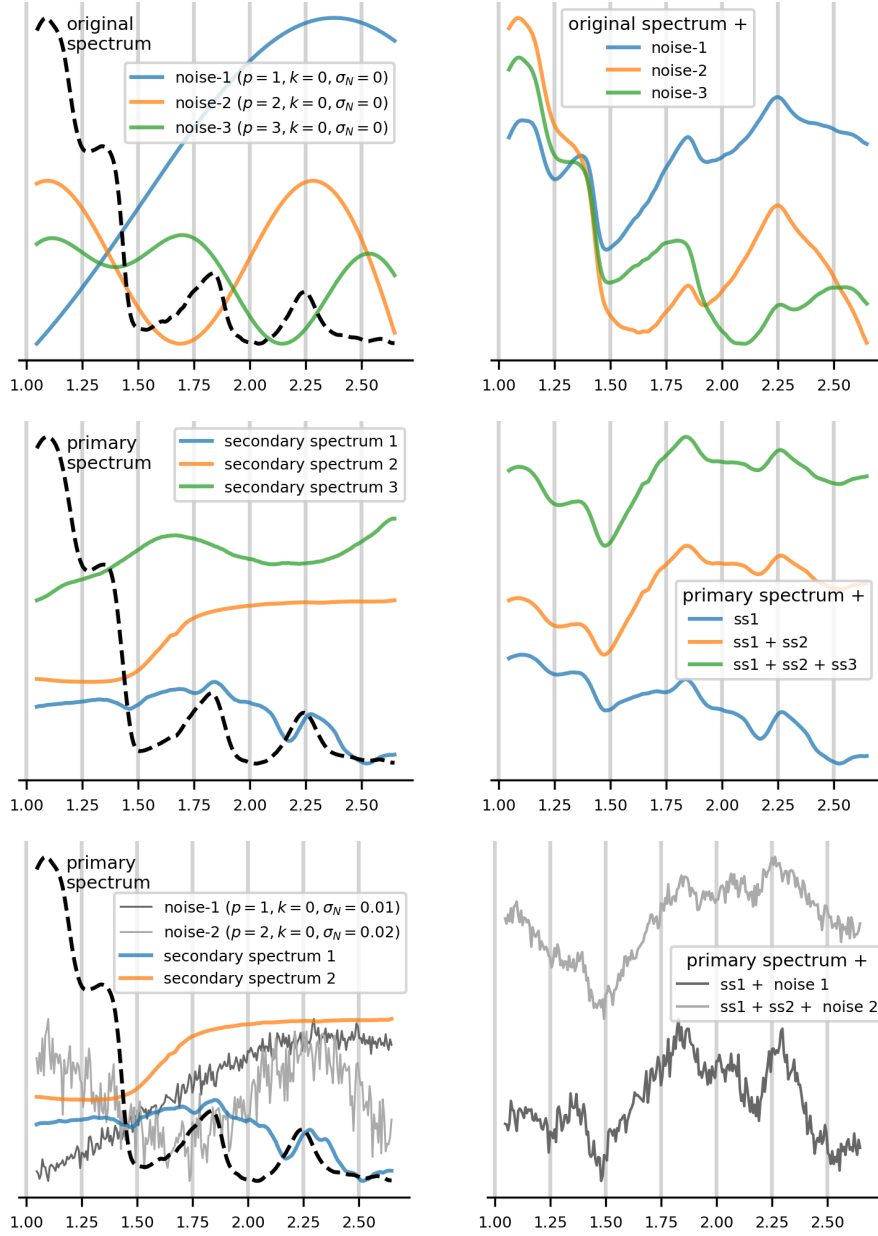


Figure 5.4: Example of synthesizing dataset-1 (top row) dataset-2 (middle row) and dataset-3 (bottom row) for different noise parameters are shown using H₂O-Ice spectrum from MICA spectral library.

Dataset-1 can be used to test the performance of the continuum removal process on spectra affected by non-convex continuum that could be generated by the instrumental artifacts and environmental noises in real spectra. Dataset-2, on the other hand, can test the same if there is mixed-spectra. Dataset-3 includes both of these types of noise in a spectrum and can additionally test for fluctuation noise in the spectrum. For each mineral class, 100 samples were generated for each combination of specifications in each dataset. The generation process involved randomness (eq. 5.3.1), resulting in each sample being unique. Figure 5.4 illustrates the process for creating these

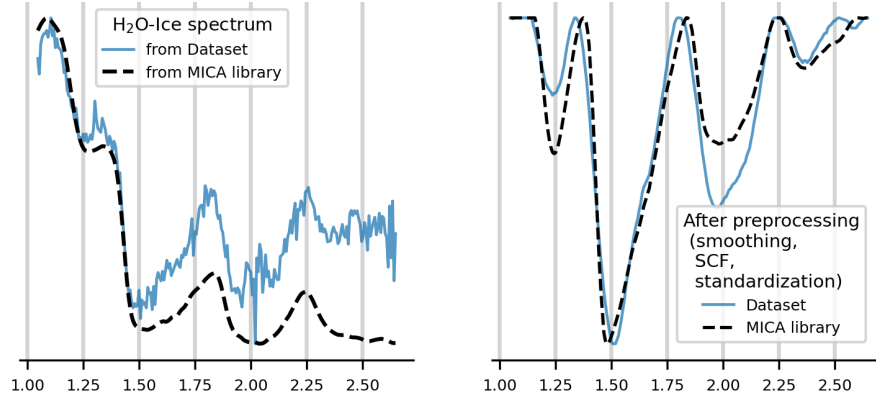


Figure 5.5: A preprocessing pipeline that includes SCF as the continuum removal operation can translate the two H₂O-Ice spectrum (from MICA spectral library and CRISM TRDR dataset) in the left image to the right image.

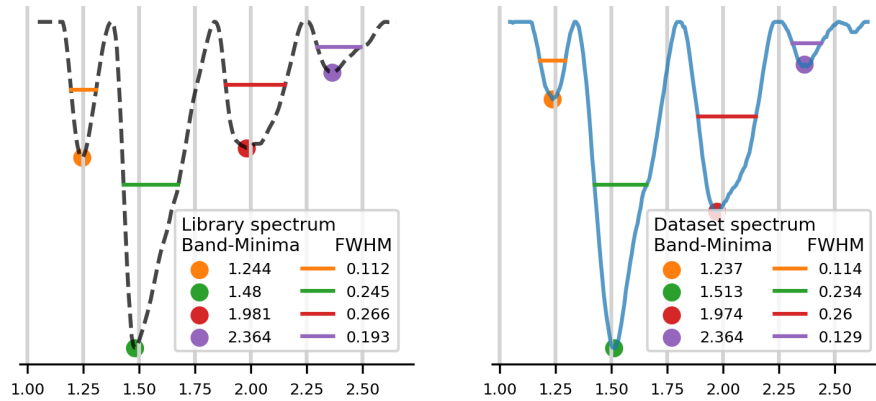


Figure 5.6: The band-minima and FWHM for all the prominent segments of the processed spectra given in figure 6.1

three datasets. The final dataset, dataset-4, consists of real spectra captured from the Martian surface by the CRISM sensor.

5.3.1.1.2 CRISM TRDR Data (dataset-4) Plebani et al in Plebani et al. (2022) using a hierarchical Bayesian model classified a collection of 592413 TRDR spectra, that is from more than 70 different images, with 39 different labels including some spectra for artifacts and some bland pixels, of which 28 labels are common with MICA library. The evaluation process here is restricted to these minerals only, randomly sampling 200 spectra from each label. In this experiment, only the bands within the 1-2.6 μm wavelength range were considered, from the given bands for the 1-3.47 μm range.

In Kumari et al. (2023a) a preprocessing pipeline is used for mineral identification in CRISM MTRDR (Map-Projected Targeted Reduced Data Record) data. The

pipeline includes spectra smoothing, spike removal, continuum removal, and spectra standardization. Similar steps are applied to the datasets used here. To eliminate fluctuation noise, dataset-4 and dataset-3 essentially undergo spectra smoothing and spike removal steps, while all four datasets are standardized and undergo continuum removal. Proper smoothing is crucial for the SCF method, which fits a parabola through local maxima in a segment, and smoothing helps remove unwanted kinks from spectra. Figure 6.1 illustrates the effect of the preprocessing steps applied on H₂O-Ice spectrum from the MICA library and dataset-4. To analyze the effectiveness of the proposed SCF in comparison with UCH, all the evaluation measures described below are calculated with SCF and UCH each used once in the pipeline while keeping all other steps the same.

5.3.1.2 Evaluation Measures

5.3.1.2.1 Band-minima Score A band-minima refers to the position of minimum reflectance value at a spectral region, generally an absorption, in a non-translated spectrum, that is before the continuum removal operation on it. On the contrary, the band-center is the position of the minimum reflectance value in an absorption after the translation. There can be a minor shift between the band-minima and band-center positions for absorptions. The amalgamation of the positions of band-center in different absorptions or segments of a spectrum is a useful identifier for distinguishing materials as each of them has a unique set of positions and shapes of the absorptions over the wavelength domain. In spectroscopy, FWHM (Full Width at Half Maximum) is a measurement used to describe the shape of absorption in a translated spectrum, that measures the width of absorption in terms of the range of wavelengths at which the depth of the absorption is half of its maximum value. As the datasets in the experiments are either TRDR/MTRDR or synthetic data derived from them, all characterized by a nearly constant spectral resolution ($0.00655 \mu m$) within the 1-2.6 μm wavelength range, the accuracies of absorption detection are assessed using thresholds related to the spectral resolution. Specifically, a 3-band difference (approximately $0.02 \mu m$) from the expected position is considered to evaluate the correct detection of band-center and a 6-band difference (approximately $0.06 \mu m$) for FWHM. These thresholds are chosen through experiments to ensure they do not significantly impact

mineral identification accuracy. From both the preprocessed test spectrum \mathbf{t} and the corresponding library spectrum \mathbf{l} , the absorptions are extracted first. Subsequently, tiny absorptions are filtered out using a threshold. The positions of the band-center and the FWHMs in the remaining absorptions are compared to assess their similarity.

Let $\mathcal{A}^{\mathbf{t}}$ and $\mathcal{A}^{\mathbf{l}}$ be the set of absorptions in \mathbf{t} and \mathbf{l} respectively. Let $BM(\mathcal{A}_k^{\mathbf{l}})$ and $FWHM(\mathcal{A}_k^{\mathbf{l}})$ represent the band-center position and FWHM respectively in the k -th absorption in \mathbf{l} . Similarly, $BM(\mathcal{A}_k^{\mathbf{t}})$ and $FWHM(\mathcal{A}_k^{\mathbf{t}})$ respectively are the band-center position and FWHM in the k -th absorption in \mathbf{t} . An example of this is shown in figure 5.6.

Through a one-to-one mapping based on the nearest band-center positions a bijection of the highest possible cardinality is established from $\mathcal{A}^{\mathbf{l}}$ ($\subseteq \mathcal{A}^{\mathbf{l}}$) to $\mathcal{A}^{\mathbf{t}}$ ($\subseteq \mathcal{A}^{\mathbf{t}}$). Let i -th absorption in $\mathcal{A}^{\mathbf{l}}$ is mapped with b_i -th absorption in $\mathcal{A}^{\mathbf{t}}$. With this, the two measures band-center Score and FWHM Score are defined as below.

5.3.1.2.2 Band-center Score The mean-shift in the band-center position in \mathbf{t} is defined as,

$$M_{BM}(\mathbf{t}) = \frac{\sum_{\forall \mathcal{A}_i^{\mathbf{l}} \in \mathcal{A}^{\mathbf{l}}} |BM(\mathcal{A}_i^{\mathbf{l}}) - BM(\mathcal{A}_{b_i}^{\mathbf{t}})|}{|\mathcal{A}^{\mathbf{l}}|} \quad (5.3.2)$$

$|\cdot|$ in the numerator denotes the absolute difference and in the denominator denotes the cardinality.

For a set of test spectra \mathcal{T} the band-center score is obtained by the fraction of the set for which the mean-shift in the positions of band-center is lesser than $0.02 \mu m$. Formally,

$$\frac{count(M_{BM}(\mathbf{t}) \leq 0.02), \forall \mathbf{t} \in \mathcal{T}}{|\mathcal{T}|} \quad (5.3.3)$$

5.3.1.2.3 FWHM Score Similarly, the mean-change in the FWHM in \mathbf{t} is defined as,

$$M_{FWHM}(\mathbf{t}) = \frac{\sum_{\forall \mathcal{A}_i^{\mathbf{l}} \in \mathcal{A}^{\mathbf{l}}} |FWHM(\mathcal{A}_i^{\mathbf{l}}) - FWHM(\mathcal{A}_{b_i}^{\mathbf{t}})|}{|\mathcal{A}^{\mathbf{l}}|} \quad (5.3.4)$$

and FWHM score of \mathcal{T} is obtained by,

$$\frac{count(M_{FWHM}(\mathbf{t}) \leq 0.06), \forall \mathbf{t} \in \mathcal{T}}{|\mathcal{T}|} \quad (5.3.5)$$

Both the band-center score and FWHM score can be computed in percentage also, as given in table 5.1, 5.2 and 5.3.

5.3.1.2.4 Identification Score Identification accuracy refers to the percentage of correctly identified spectra in the experiment. Datasets 1, 2, and 3 use the primary spectrum’s class as its true label, while dataset 4 is pre-labeled. In identification procedures, each class in a dataset is typically assigned a value based on a similarity measure or the likelihood of a test spectrum belonging to that class. The test data is then assigned to the class with the highest similarity measure or likelihood. Proper preprocessing is necessary before identification, and the Weighted Sum of Segment Correlation (WSSC) procedure used in this study is highly dependent on it. The identification process can be impacted by slight changes in the preprocessing parameters, which may result in assigning a lower similarity measure or likelihood to the true-label class. As determining the most precise parameters for the preprocessing is beyond the scope of this study, here a general set of parameters as given in Kumari et al. (2023a) is applied to the datasets. The identification score in this experiment is calculated based on the percentage of spectra in a dataset for which the true label is assigned a value within 5% of the highest assigned value for any class. The classification techniques used to identify a spectrum are described below.

5.3.1.3 Identification Procedures

In addition to the neural network-based model CNN LeCun et al. (2015), the accuracy of mineral identification is also determined by a novel spectra-matching method called Weighted Sum of Segment Correlation (WSSC). It shares some similarities with the shape-matching algorithm described in Clark et al.’s work on imaging spectroscopy Clark et al. (2003), which uses a condition-driven and sophisticated framework for mineral identification for hyperspectral images. Unlike imaging spectroscopy, the method WSSC relies more on extracting the prominent absorptions without any pre-knowledge about the absorption features in the spectral library, by calculating a match index between any two spectra based on a new correlation measure. WSSC also differs in the process of calculating the spectra correlation coefficient and the match index. This method is described in detail before briefly discussing the specifications of the CNN

model.

5.3.1.3.1 Weighted Sum of Segment Correlation (WSSC) In this method, first, the absorptions in the preprocessed library spectrum are extracted. Then spectrum portion in each absorption is compared with the corresponding spectrum portion in the preprocessed test spectrum to calculate correlation coefficients. A matching index is then calculated by summing all the correlation coefficients weighted by a measure of the shape of the absorptions in the preprocessed library spectrum.

Let, in the preprocessed library spectrum \mathbf{l} , there exists an absorption within the wavelength segment \mathbf{w}' characterized by shoulder-points at both ends. Then, $\mathbf{l}_{(\mathbf{w}')}$ represents the corresponding spectrum segment in \mathbf{l} , and $\mathbf{t}_{(\mathbf{w}')}$ denotes the spectrum segment in the preprocessed test spectrum \mathbf{t} . Now, these two spectrum segments can be most matched with the other by a translation involving shifting towards the other and enhancing/reducing its curvature. For $\mathbf{t}_{(\mathbf{w}')}$, the most effective translation to match with $\mathbf{l}_{(\mathbf{w}')}$ is given by eq. 5.3.6, while for $\mathbf{l}_{(\mathbf{w}')}$ to match with $\mathbf{t}_{(\mathbf{w}')}$ the same is given by eq. 5.3.7.

$$\mathbf{l}_{(\mathbf{w}')} = a_1 + b_1 * \mathbf{t}_{(\mathbf{w}')} \quad (5.3.6)$$

$$\mathbf{t}_{(\mathbf{w}')} = a_2 + b_2 * \mathbf{l}_{(\mathbf{w}')} \quad (5.3.7)$$

where the coefficients a_1 and a_2 adjust the shift of the spectra segments, and b_1 and b_2 to modify the curvature during the translation process. The values of these coefficients are derived by minimizing the quadratic error between one spectrum segment and the translated other spectrum segment.

Considering $l = \mathbf{l}_{(\mathbf{w}')(w)}$ and $t = \mathbf{t}_{(\mathbf{w}')(w)}$ (the value at wavelength $w (\in \mathbf{w}')$ in the spectrua segments), from eq. 5.3.6, the quadratic error can be minimized as follows.

$$\frac{\partial}{\partial a_1} \left(\sum_{w \in \mathbf{w}'} (l - a_1 - b_1 * t)^2 \right) = 0 \quad \frac{\partial}{\partial b_1} \left(\sum_{w \in \mathbf{w}'} (l - a_1 - b_1 * t)^2 \right) = 0 \quad (5.3.8)$$

Considering $n = |\mathbf{w}'|$ (the size of the segment), solving 5.3.8, b_1 and a_1 is derived as

$$b_1 = \frac{\sum_{w \in \mathbf{w}'} (l * t) - \left(\sum_{w \in \mathbf{w}'} l \right) * \left(\sum_{w \in \mathbf{w}'} t \right) / n}{\sum_{w \in \mathbf{w}'} (t)^2 - \left(\sum_{w \in \mathbf{w}'} t \right)^2 / n} \quad a_1 = \frac{\left(\sum_{w \in \mathbf{w}'} l \right) - b_2 * \left(\sum_{w \in \mathbf{w}'} t \right)}{n} \quad (5.3.9)$$

Similarly from eq. 5.3.7 b_2 and a_2 can be derived as

$$b_2 = \frac{\sum_{w \in \mathbf{w}'} (t * l) - \left(\sum_{w \in \mathbf{w}'} t \right) * \left(\sum_{w \in \mathbf{w}'} l \right) / n}{\sum_{w \in \mathbf{w}'} (l)^2 - \left(\sum_{w \in \mathbf{w}'} l \right)^2 / n} \quad a_2 = \frac{\left(\sum_{w \in \mathbf{w}'} t \right) - b_1 * \left(\sum_{w \in \mathbf{w}'} l \right)}{n} \quad (5.3.10)$$

Although the coefficients a_1 , a_2 , b_1 and b_2 vary across different spectrum segments in the preprocessed library spectrum, for improved readability, the notation (\mathbf{w}') is not superscripted with the coefficients. However, the intended meaning is considered the same when it is superscripted.

The correlation coefficient $c^{(\mathbf{w}')}$ between the two segments $\mathbf{t}_{(\mathbf{w}')}$ and $\mathbf{l}_{(\mathbf{w}')}$ on the wavelength segment \mathbf{w}' is calculated as

$$c^{(\mathbf{w}')} = \begin{cases} \sqrt{b_1^{(\mathbf{w}')} * b_2^{(\mathbf{w}')}} & \text{if } b_1^{(\mathbf{w}')} , b_2^{(\mathbf{w}')} > 0 \\ 0 & \text{otherwise} \end{cases} \quad (5.3.11)$$

Let \mathcal{W} be the set of wavelength segments of the extracted distinct absorptions in \mathbf{l} . Let $f^{(\mathbf{w}')}$ and $d^{(\mathbf{w}')}$ respectively be the FWHM and the depth at the band-center of such a segment $\mathbf{w}' \in \mathcal{W}$. A weight $wt^{(\mathbf{w}')}$ associated with the segment \mathbf{w}' can be defined as the proportion of the sum of products of $f^{(\mathbf{w}')}$ and $d^{(\mathbf{w}')}$ over all the segments in \mathcal{W} .

$$wt^{(\mathbf{w}')} = \frac{f^{(\mathbf{w}')} * d^{(\mathbf{w}')}}{\sum_{\forall \mathbf{w} \in \mathcal{W}} (f^{(\mathbf{w}')} * d^{(\mathbf{w}')})} \quad (5.3.12)$$

The matching index I between \mathbf{l} and \mathbf{t} can be defined as,

$$I = \sum_{\forall \mathbf{w} \in \mathcal{W}} (wt^{(\mathbf{w}')} * c^{(\mathbf{w}')}) \quad (5.3.13)$$

Figure 5.7 depicts a demonstration of calculating I .

The mineral type of a test spectrum can be identified by selecting the library mineral with the highest match index. The matching index I , constrained by the non-negativity of $c^{(\mathbf{w}')}$, does not penalize non-correlated segments in the two spectra being matched. This feature increases the chances of correctly identifying the mineral group, where the exact end-member class is not identified.

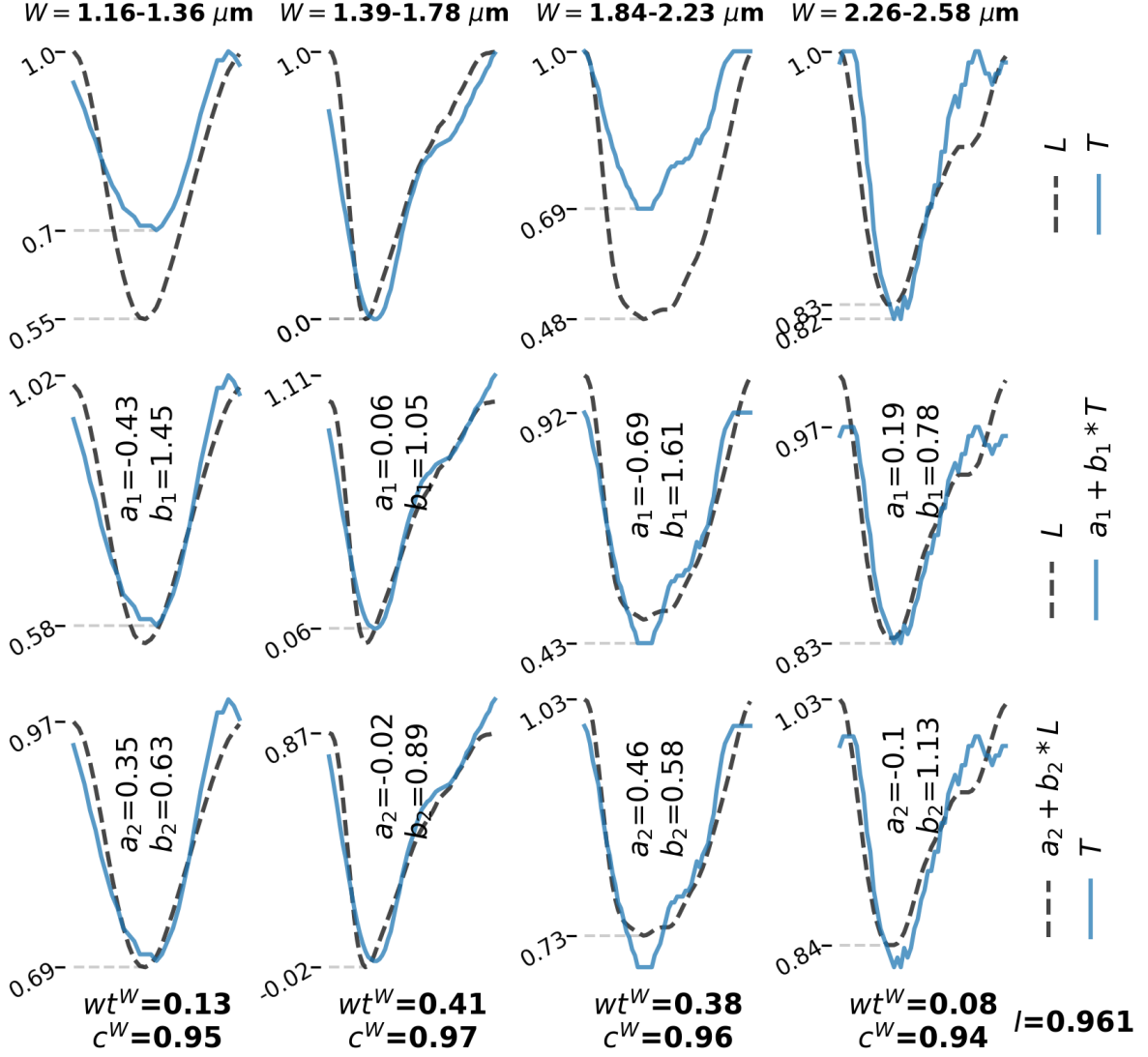


Figure 5.7: **Top Row:** The absorptions ($\mathbf{l}_{(w')}$) on the library spectrum (\mathbf{l}) and their corresponding segments ($\mathbf{t}_{(w')}$) in the test spectrum (\mathbf{t}) from figure 5.6. **Middle Row:** $\mathbf{t}_{(w')}$ are translated to align with $\mathbf{l}_{(w')}$, with the associated translation coefficients (a_1 and b_1) provided. **Bottom Row:** The translation of $\mathbf{l}_{(w')}$ to align with $\mathbf{t}_{(w')}$, accompanied by the respective translation coefficients (a_2 and b_2). Correlation coefficients (c^W) calculated from these translation coefficients are presented at the bottom. Also, the weights of the absorptions (wt^W), calculated using the FWHMs of the absorption segments (as shown in figure 5.6) and the depth at the absorption minima (as shown in the top row), are shown. Ultimately, the matching index (I) between \mathbf{l} and \mathbf{t} is calculated.

Note: The absorptions in top-row are extracted from \mathbf{l} , and the corresponding portion in \mathbf{t} are considered.

5.3.1.3.2 CNN Model The experiment employs a shallow sequential CNN model as described in chapter 4. The model consists of three sets of convolution, max-pool, and drop-out layers, followed by a flatten layer and a dense output layer. The optimal parameter values for the model are determined using hyper-parameter tuning. The number of epochs is set to 50 with a batch size of 150. Leaky ReLU activation is

utilized in all layers except the last one, which uses SoftMax activation. The loss function is categorical cross-entropy, and the optimizer is RAdam with a learning rate of 1×10^{-5} . The datasets are split into 60-20-20 ratio for training, validation and testing. The test accuracies are evaluated to assess the performance.

5.3.2 Performance Analysis

The Upper Convex Hull and the Segmented Upper Hull, as defined in the literature, do not have the provision of customizability. In contrast, the Geometric Hull, although presented in the literature to consider all local minima in an intermediate step, tends to overfit a real input spectrum if all local minima are considered due to its iterative nature and presence of fluctuations in a real spectrum, resulting in a limited ability to detect absorption features, particularly for the minerals having distinguishable broad absorptions. Lastly, SCF, described in Section 4.1 as a non-parametric approach, exhibits various forms based on factors such as whether selective or all local minima are used to fit the curve, the minimum required number of local maxima in a segment for consideration in further processing, whether a recursive approach is employed to detect more shoulder points, and so on. To prevent overfitting in GH, only the local minima beyond a specified threshold depth from its shoulder points are taken into consideration. SCF also, in the crude form does not perform optimally when dealing with minerals that exhibit a broad absorption feature like mafic minerals and halides. For such minerals specifically, SCF considers a segment for further division only if it contains at least 3 local minima.

Table 5.1 contains the experimental results of band-center score and FWHM score from dataset-1, 2 and 3 for different values of p , k and σ . The performances of the datasets in table 5.1 with thresholds of $0.02 \mu m$ for band-center score and $0.06 \mu m$ for FWHM score align with the performances with accuracy scores by WSSC method presented in table 5.2 for the same datasets and specifications. Table 5.3 contains all these evaluation results of dataset-4. The primary objective of the analysis is to understand the effectiveness of the proposed method on some data with certain characteristics, and therefore, the degree of change in scores for a change in parameters of the data is more important than the exact scores themselves. However, achieving satisfactory high scores on an evaluation metric can provide evidence for the effec-

tiveness of the method. The experimental results provide various insights, which are summarized below.

Table 5.1 shows that for each of the methods, as the number of peaks in the estimated instrumental noise (p) increases, the band-center and FWHM scores decrease (dataset-1 part). On the other hand, as the number of secondary spectra mixed with the primary spectra (k) increases, both the band-center and FWHM scores increase (dataset-2 part), indicating that a smoother background curvature is formed when more spectra are mixed with the primary spectrum. If both instrumental artifacts (p) and the presence of other spectra (k) distort the primary spectra, as presented in dataset-3 part of table 5.1, the scores become more dependent on k . This means that if both k and p are increased both scores increase. But, similar to the outcome of dataset-1 and 2, for a constant p value, the scores increase as k increases, and, the scores decrease for a constant k value as p value increases. This trend is evident in each row of the dataset-3 part. As environmental noise (σ_N) increases the scores decrease, which is expected as high levels of environmental noise distort local small absorption signatures in the spectra and require objective-specific preprocessing steps to handle them. The applied smoothing may not be sufficient for this task. In all of the specifications considered in these three datasets, the SCF outperformed both UCH, SUH, and GH in terms of both the band-center and FWHM scores. Specifically, for UCH, the low FWHM scores indicate that UCH is more reliant on global shapes, and if the curvature is distorted by the noises, the shape of the extracted absorption signatures could deviate significantly from the library spectra. The inferior performance of SUH primarily is due to its inconsistency in separating specific absorptions similar to those in the library spectrum within the synthetic data with the imposed curvature. This inconsistency is exacerbated as tends to detect more shoulder points than UCH, but with the limitation of not adapting the change of slope of the estimated continuum. Conversely, SCF relies more on local shapes and can compare more accurately with the library spectra by extracting more spectral regions with small absorption signatures.

Table 5.2 shows a strong correlation between the accuracy of mineral class identification using the WSSC method and the correct determination of the position of the band-center. This means that as the accuracy of band-center determination increases or decreases, so does the accuracy of mineral class identification using the

Table 5.1: Band-center and FWHM scores (in %) using **data-1**, **data-2**, and **data-3** for different p , k and σ

CR Method	dataset-1			dataset-2			dataset-3													
	p	Band-center	FWHM	k	Band-center	FWHM	Band-center			FWHM										
							$p = 1$	$p = 2$	$k = 1$	$p = 1$	$p = 2$	$k = 2$								
UCH		96.8	80.0		65.2	70.0														
SUH	1	79.5	77.1	1	72.6	76.8	0.01	69.5	69.2	78.5	74.0	58.5	56.6	59.7	57.0					
GH		96.0	87.3		76.1	81.3		72.5	67.5	75.5	68.0	63.0	60.3	62.3	60.8					
SCF		96.9	96.0		74.3	83.4		78.0	68.7	81.3	80.5	82.0	81.3	84.8	83.8					
UCH		90.0	72.0		71.6	78.0		77.5	73.2	84.4	81.3	82.3	82.3	85.9	85.7					
SUH	2	84.6	80.0	2	78.4	82.7	0.02	68.4	65.6	73.7	70.8	52.4	51.2	56.0	52.1					
GH		91.4	85.7		76.6	83.6		64.2	58.2	67.7	59.0	57.7	56.3	58.8	58.3					
SCF		94.0	93.0		78.1	85.1		73.5	74.7	77.5	78.5	77.7	76.3	81.8	82.5					
UCH		89.0	73.0		75.2	81.0		75.1	73.0	81.7	80.2	79.5	79.0	82.6	83.4					
SUH	3	84.7	83.8	3	81.0	84.4	0.03	66.2	62.1	74.7	66.0	52.9	47.5	52.1	49.3					
GH		93.8	82.8		77.5	86.7		58.5	52.5	57.8	53.1	55.5	53.5	56.7	52.8					
SCF		92.6	91.3		80.5	88.0		71.0	61.7	78.0	70.7	76.5	74.7	78.7	76.8					
UCH		88.5	75.0		78.2	84.0		74.0	69.0	81.2	73.0	75.4	76.0	81.8	78.0					
SUH	4	83.8	85.5	4	82.1	84.3	0.04	65.2	59.0	69.7	63.3	46.7	45.6	51.1	46.3					
GH		90.1	81.5		81.7	87.0		54.0	48.3	55.7	49.9	54.3	51.7	54.9	53.0					
SCF		92.0	91.0		81.1	88.4		60.8	62.7	71.5	73.5	73.0	69.9	77.9	76.4					
								72.1	65.5	78.7	71.2	73.5	72.0	78.8	76.0					

WSSC method. This is because both of these scores rely on accurately extracting the segments and are similarly impacted by the data specifications. The SCF method showed better performance in terms of identification score by the WSSC method for each of the datasets, similar to the band-center and FWHM scores. This suggests that using a higher number of segments with small spectral ranges in the SCF method can yield more precise information compared to using a lesser number of segments with long spectral ranges in the UCH method. Although the test accuracy scores of the CNN model for all the models are relatively higher than WSSC, unlike WSSC, the accuracy scores obtained by the CNN model do not consistently favour SCF over the other methods. This suggests that shallow neural network models can more effectively learn hidden features when the original curvature of the unprocessed spectra is better preserved. UCH preserves the curvature better than SCF by extracting a lesser number of shoulder points. Also, when σ is higher, generally SCF performs better than the other two continuum removal methods using both WSSC and the CNN model, suggesting its resilience over noisy data.

Table 5.3 shows the evaluation metric scores for each mineral group separately. The experiments have indicated that, for each method, while there may be some mineral spectra whose true labels are not detected, a large portion of those spectra are still classified into the correct mineral group. This indicates that, at the very least, the WSSC method with SCF to detect the absorption can detect mineral groups with a high degree of accuracy, even if the detection of individual minerals may not be as precise. The relatively high scores for all the mineral groups in table-5.3 compared to the scores in table-5.2 suggest that the synthetic dataset-3 has similar or even more noise than the TRDR dataset of real spectra. This indicates that similar synthetic datasets can be used effectively to determine the efficacy of such methods. The presented accuracy scores of WSSC in the table suggest that WSSC is not very accurate in detecting minerals that have prominent absorption signatures in the form of broad spectral segments, termed as broad-bands, or sharp absorptions within a broad band in the spectrum, such as silicates and carbonates. For dataset-4, it was observed that the accuracy scores of CNN obtained by using SCF are not always greater than the scores obtained by using UCH, SUH, and GH, similar to the results for dataset-3 in table-5.2. However, for most of the mineral groups, the SCF method yields higher

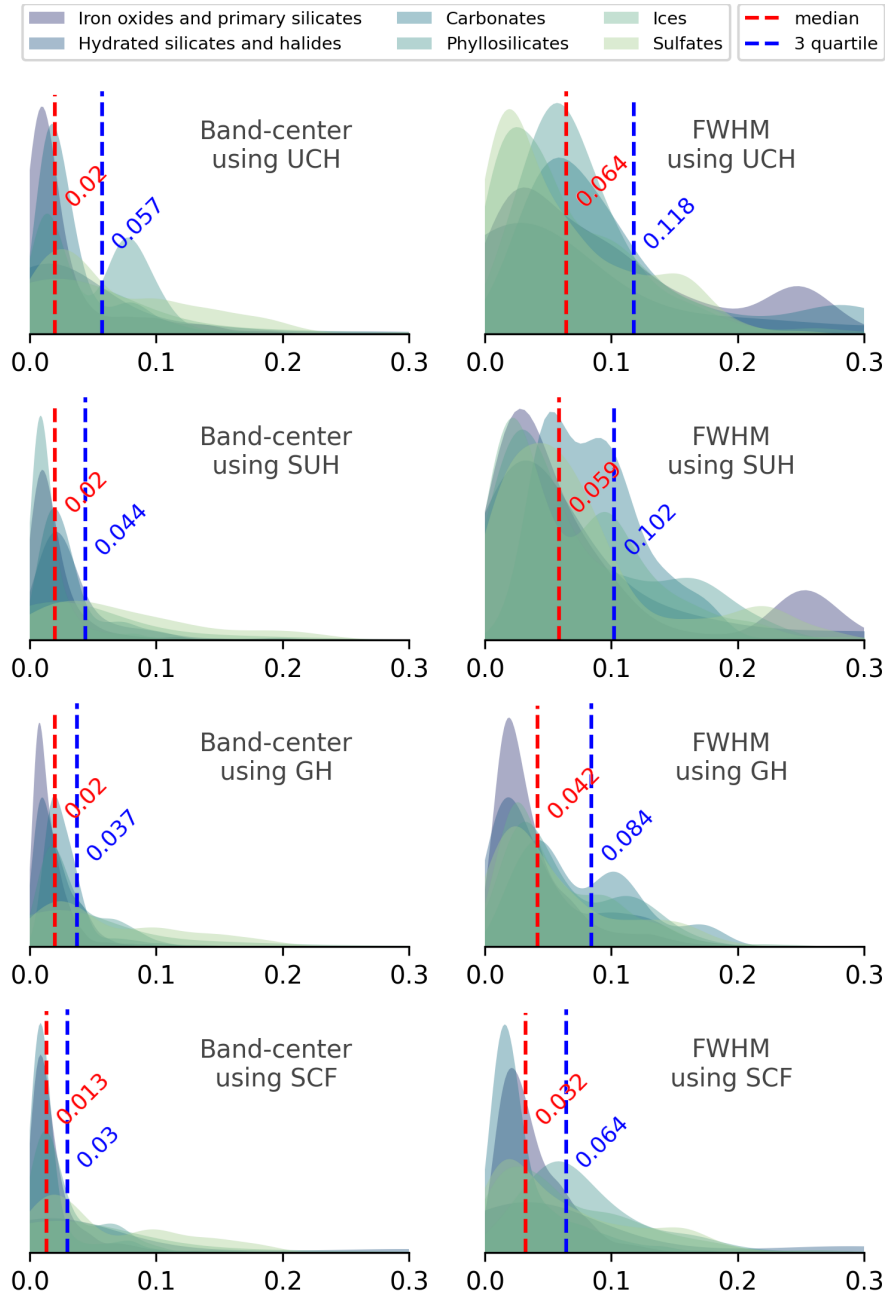


Figure 5.8: The density plots of the differences in band-center and FWHM values between the processed spectra of dataset-4 and the corresponding spectra from the MICA library, using UCH, SUH and SCF in preprocessing. The plots are colour-coded by the mineral groups. The lesser quartile-2 (median) and quartile-3 values indicate that the band-center and FWHM values are more accurate when SCF is applied.

accuracy scores, resulting in an overall improvement in the performance of around 1.5%, where as by the described method WSSC, where local shape-matching is considered, the betterment is more than 8%. Figure 5.8 represents the density plots of the calculated mean shift in band-center and mean change in FWHM for the spectra in dataset-4. It is evident from the figure that SCF detects the band-centers of the

absorptions more accurately and preserves the shape of the absorptions (FWHMs) more precisely similar to the library than the compared methods UCH, SUH, and GH.

The following is the summary of the experiments:

- SCF relies on local spectral shapes, and exhibits enhanced noise resilience in terms of preserving more precise spectral information like band-center and FWHM of the absorption features.
- There is a strong correlation between the preservation of band-center and FWHM and the mineral identification accuracy. Preprocessing the spectra with SCF continuum removal yielded satisfactory accuracy gains over the other methods for mineral identification using the spectra matching technique WSSC and also using a shallow CNN model. Performance gains were consistent across the mineral groups.
- While WSSC with SCF may encounter challenges in accurately identifying minerals with broad or sharp absorptions within broad bands, the methods generally maintain accuracy in identifying mineral groups, even if some mineral labels are detected incorrectly.
- The experiments conducted on both synthesized and real spectra from the CRISM instrument, obtained from the Martian surface, demonstrate adequate results. This outcome instills reliability for applying SCF in mineral identification tasks on similar hyperspectral data, particularly for mineral mappings on the Martian surface.

5.3.2.1 Performance Comparison with Previously Introduced Models

Recall the feature extraction approach introduced in chapter 4. Let, \mathbf{w} be a wavelength segment and the corresponding reflectance values in the spectra is \mathbf{r} . Let, in \mathbf{w} the starting and ending wavelengths are s and t . Let, \mathbf{l} be the straight line connecting \mathbf{r}_s and \mathbf{r}_t , that is, connecting the endpoints in the spectra segment. Then the position of the band-center can be calculated as $\mathit{argmin}(\mathbf{l} - \mathbf{r})$, and the band-area within this range can be estimated by $\sum(\mathbf{l} - \mathbf{r})$. Note that, by this definition of band-area the values can be negative too.

The correct selection of segments, guided by setting the Segmented Curve Fitting (SCF) based on mineral group characteristics, results in the accurate identification

of the most distinguishable wavelengths. The two features, the position of band-center and band-area, were extracted for each wavelength segment in each of the true spectra in MICA library, comprising the domain of a total 150 features. Each feature is standardized to get rid of any scale mismatch before passing into the model. In contrast to the feature selection approach presented in chapter 4, where the most diverse wavelength ranges were chosen, SCF emphasizes the absorption shape itself. This is evident in the improved accuracy across almost all mineral groups in table 6.3 with particular efficacy in detecting broad absorptions characteristic of halides.

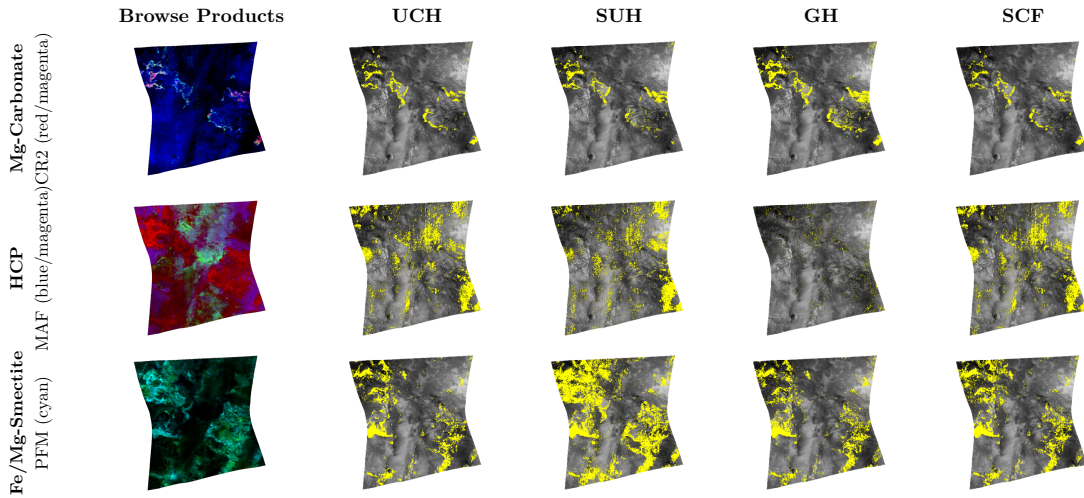
Table 5.4: Mineral-groupwise accuracy comparison with previously proposed models

Mineral Group	Proposed ANN	ANN in chapter 4	CNN in chapter 4
Sulfates	88.7	84.2	85.4
Phyllosilicates	91.2	89.2	78.1
Hydrated silicates	81.7	69.4	68.8
Ices	96.2	90.2	97.5
Carbonates	74.5	73.3	77.1
Primary silicates	83.2	82.8	86.4

5.4 Results and Discussion

In this section, the result of mineral identification on CRISM MTRDR data of martian-surface are presented, which were obtained by using the previously described WSSC method to match the wavelength position and shape of characteristic absorption features with the spectra in MICA library. SCF is applied as a preprocessing step on the data to remove the continuum and produce scaled spectra. Two of the CRISM hyperspectral image (FRT93BE) used in chapter 4 for detailed evaluation of the model are used here also. FRT93BE contains 804×832 pixels and FRT13D1F contains 800×648 pixels, with 489 bands covering a wavelength range of $0.43\text{-}3.89 \mu\text{m}$. However, in this experiment, similar to the CRISM MTRDR and TRDR data described in section 5.3, the wavelength range of $1\text{-}2.6 \mu\text{m}$ is considered. Similar to the results shown in chapter 4, the detected dominant minerals in FRT93BE are Mg-Carbonate, High-Calcium Pyroxene (HCP) and Mg-Smectite, and in FRT13D1F are Low-Calcium Pyroxene (LCP) and gypsum.

FRT93BE (from Jezero Crater region of Mars)



FRT13D1F (from Columbus Crater region of Mars)

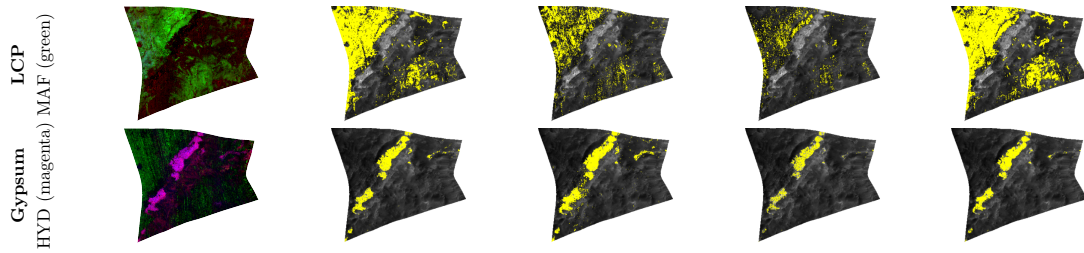


Figure 5.9: Detected dominant minerals in CRISM MTRDR data FRT93BE and FRT13D1F. For each mineral, the pixels with a match index of more than 0.7 with the corresponding library spectrum are highlighted. The first column contains the browse products with colours indicated for visual verification.

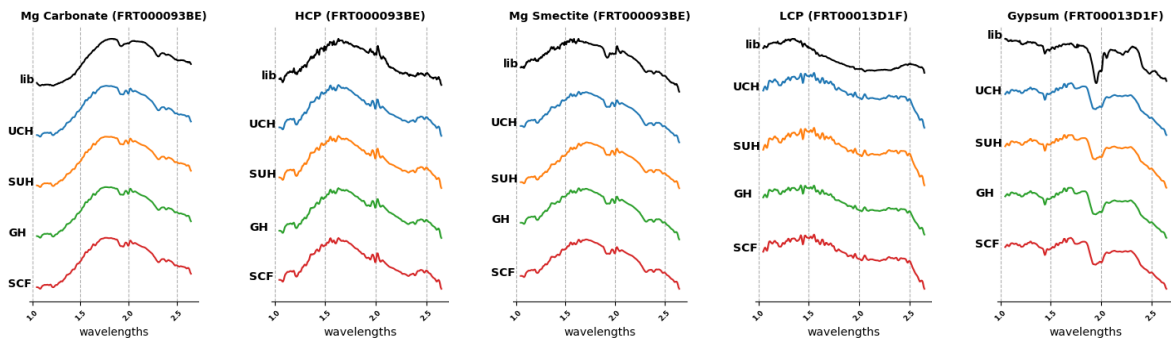


Figure 5.10: Approximately 5% of detected minerals for each method are randomly sampled to calculate mean spectra, which are compared with the corresponding true spectra in the MICA spectral library.

Figure 5.9 shows the distributions of the dominant minerals found in the two images. To compare the proposed continuum removal method SCF's ability to accurately detect the absorption features and match those with the library, the results are also

obtained by using other continuum removal methods like UCH, SUH and GH. The pixels with a match index exceeding 0.7 with the corresponding library spectrum are highlighted in figure 5.9. This approach allows a pixel to be associated with more than one mineral class, offering a soft classification suitable for hyperspectral data like CRISM, where pixels often contain mixed spectra. Figure 5.9 shows that, with the specified matching threshold, mineral distributions determined by SUH and GH exhibit limitations for minerals with broad absorption features, whereas UCH and SCF consistently hold the most resemblance with the mineral distributions provided in the browse products for all the minerals. In figure 5.10 for each method around 5% of each of the detected minerals are randomly sampled to calculate the mean spectra and are compared with the corresponding true spectrum in the library, confirming the presence of distinguishable features at expected wavelengths.

5.5 Chapter Summary

- **Introducing Segmented Curve-Fitting for continuum removal:** The Segmented Curve Fitting (SCF) is a linear time continuum removal technique that extracts more number of distinct absorptions than the traditional methods.
- **Precision in Absorption Detection:** SCF excels in detecting the positions and shapes of the absorptions in the spectra in comparison to those in the corresponding library spectra more accurately.
- **Effective Spectra Classification:** SCF surpasses traditional methods of continuum removal in classifying spectra notably when using shape matching algorithms, demonstrating its superiority in spectral analysis.

In the next chapter, a deep convolutional neural network architecture is used into the proposed mineral detection framework to enhance the mineral identification accuracy.

Chapter 6

MICAnet: A Deep Neural Network for Mineral Identification

This chapter introduces MICAnet, a novel Deep Convolutional Neural Network (DCNN) architecture inspired by renowned models like Inception-v3 and InceptionResNet-V1, designed for mineral identification from CRISM hyperspectral data. Unlike conventional DCNNs tailored for spatial inputs (image-level), MICAnet operates on spectral inputs (pixel-level), analyzing spectral information directly. Remarkably, MICAnet is the first DCNN architecture specifically developed for mineral identification using CRISM hyperspectral data. The chapter details MICAnet’s architecture and provides a thorough performance analysis comparing it to previously used models.

6.1 Dataset preparation and Methodology

Recall the MICA spectral library Viviano et al. (2014a), comprising reflectance spectra of 31 minerals obtained from CRISM hyperspectral imagery, was augmented in chapter 4 by introducing controlled local dissimilarities and larger variability along the spectral domain. This augmentation procedure, designed to better represent real-world scenarios, improved model performance and generalization for mineral identification. The optimal augmentation parameters and a comprehensive preprocessing pipeline were also established in the previous work. For continuum removal in the study, the Segmented Curve-Fitting method is employed to effectively handle differences in spectral curvatures, whereas the other preprocessing steps in the pipeline remains same as the

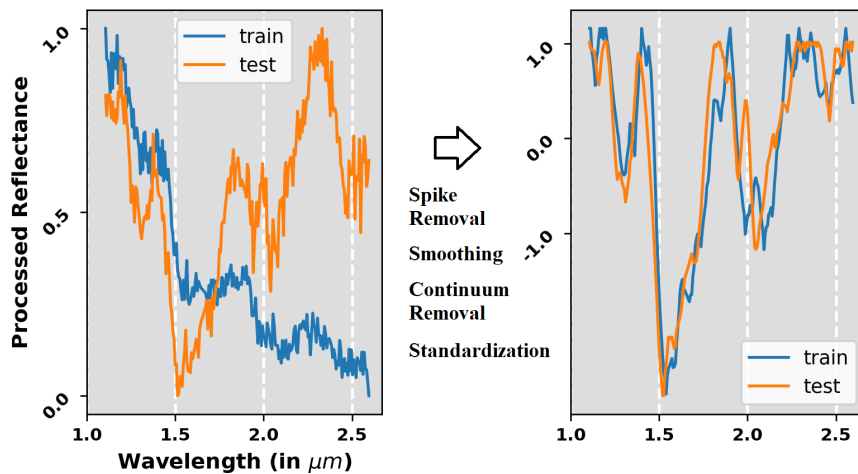


Figure 6.1: A preprocessing pipeline that includes SCF as the continuum removal operation can translate the two H₂O-Ice spectrum (from MICA spectral library and CRISM TRDR dataset Plebani et al. (2022)) in the left image to the right image.

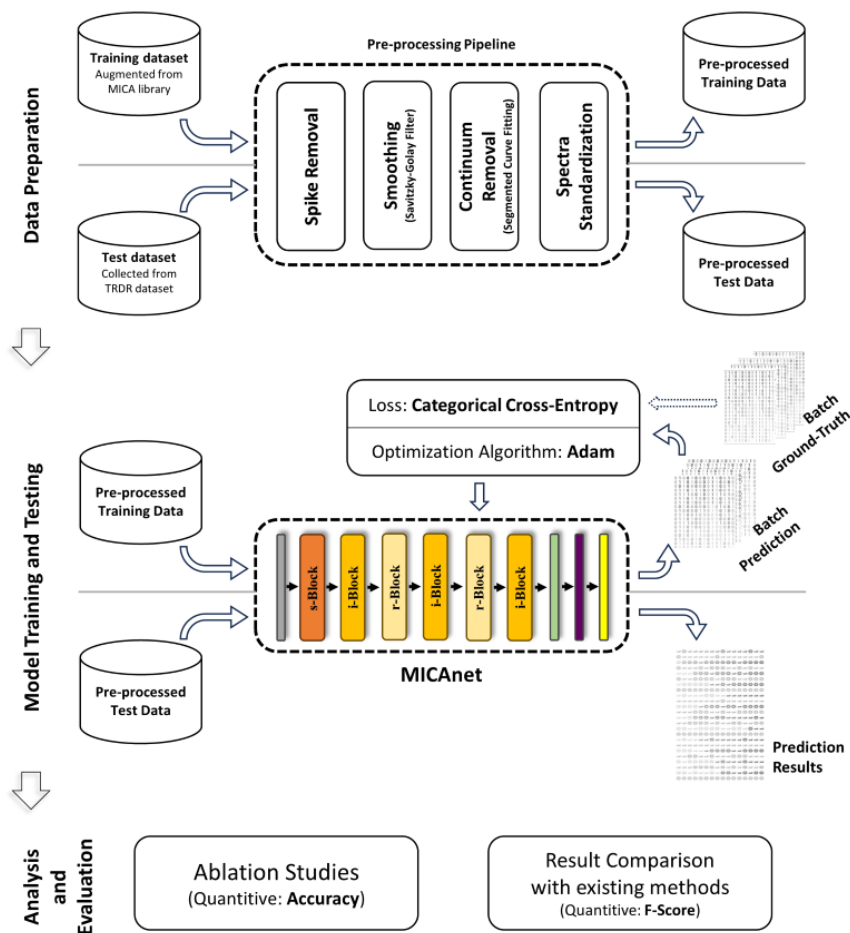


Figure 6.2: Workflow of the study

input of the CNN model described in chapter 4.

The evaluation process in this study focused only on the mineral classes that are common to both Plebani et al. (2022) dataset and the MICA library. The test dataset comprised of 200 samples per mineral class, whereas the training dataset has 1000 augmented spectra for each mineral in MICA library. Both the training dataset, which is the augmented dataset from the MICA library, and the testing dataset, which is the Plebani dataset, undergo the same preprocessing pipeline. Figure 6.1 depicts the effect of the preprocessing steps on the H₂O-Ice spectra taken from from the MICA library and dataset created in Plebani et al. (2022), and figure 6.2 presents the complete workflow of this work. For this experiment, same as 4, only the bands within the 1-2.64 μm wavelength range were considered, selected from the available bands spanning the 1-3.47 μm range. It is important to note that the term "accuracy" used while analyzing the performance of the proposed DCNN architecture in section 6.3, refers to the number of correct predictions that align with the labels provided by the model in Plebani et al. (2022).

6.2 Model Architecture

The MICANet architecture is a fusion of the design principles from Inception-v3 and InceptionResNetv1, two influential models in the field of image classification. Inception-v1 introduced Inception modules, which consist of parallel convolutional layers of different filter sizes to capture spatial features at various scales. Inception-v2 further optimized the model by using smaller convolutions sequentially to capture the effect of larger convolutions in a computationally efficient hierarchical way and incorporating batch normalization for improved convergence. Inception-v3 introduced reduction layers and a robust stem architecture to enhance pooling operations and feature extraction. InceptionResNetv1 combined Inception blocks with residual connections to address the vanishing gradient problem during training. In the context of MICANet, the architecture incorporates s-blocks, i-Blocks, and r-blocks (fig. 6.3), inspired by the stem block, reduction block, and InceptionResNet block, respectively. However, since MICANet operates on 1D spectra inputs, it utilizes 1D convolutions instead of 2D convolutions found in image-based architectures.

- **s-Block:** The s-block in the MICAnet architecture begins with an average pooling layer of 2 kernel-size and 2 strides, which helps to minimize existing noise in the input spectra. This is followed by two convolution layers, one with 1 kernel-size and the other with 3 kernel-size. The first convolution layer has 1 stride, while the second convolution layer has 2 strides, allowing for downsampling. After the convolution layers, a batch normalization layer is applied to normalize the output. The output of the batch normalization layer is then split into two separate channels. The first channel includes a max pooling layer with 2 strides, which further reduces the spatial dimensions of the features. The second channel consists of two consecutive convolution layers, one with 1 kernel-size and the other with 3 kernel-size. The last convolution layer in this channel has 2 strides, enabling downsampling. Finally, the outputs of both channels are concatenated together, creating a combined output for further processing in the network. All the convolution layers in s-Block have 32 kernels. If x is the input of an s-Block and the layers are named and indexed as given in 6.3, each s-Block can be formulated as below.

$$\begin{aligned}
O_1 &= f^b(f^{C_{i+2}}(f^{C_{i+1}}((f^{A_{i+1}}(x)), W^{i+1}, b^{i+1}), W^{i+2}, b^{i+2})) \\
O_{sChannel_1} &= f^b(f^{C_{i+4}}(f^{C_{i+3}}(O_1, W^{i+3}, b^{i+3}), W^{i+4}, b^{i+4})) \\
O_{sChannel_2} &= f^{M_{i+1}}(O_1) \\
O_{sConcat} &= O_{sChannel_1} \odot O_{sChannel_2} \\
\text{s-Block}(x) &= f^b(f^{C_{i+5}}(O_{sConcat}, W^{i+5}, b^{i+5}))
\end{aligned}$$

where f^{C_i} , f^b and \odot represent the operations of i -indexed convolution layer with ReLU activation, batch-normalization layer and concatenation layer respectively. W^i and b^i are the weights and bias of the i -indexed convolution layer.

- **i-Block:** The i-Block consists of a total of 6 channels, one of which is the residual connection from the previous layer which is added to the concatenated output of the other 5 channels. Of the 5 channels, one channel has a max pooling layer followed by a convolution layer of 1 kernel-size. In all the other channels, the convolution layers with 1 kernel-size are followed by increasing number of convolution layers with 3 kernel-size to capture different sizes of spectral patterns. These channels are termed as '*ConvChannel*'s in this paper. The concatenated output is then passed through another convolution layer with 1 kernel-size. Except for this last convolution layer, all the convolution layers have 32 kernels, whereas this last convolution has a varying number of kernels depending on this i-Block's position

in the MICAnet in order to match the dimensions. In each channel, the convolution layers of 1 kernel-size and the last convolution layers of 3 kernel-size are followed by batch normalization layers. The i-Block can be formulated as follows.

$$\begin{aligned}
O_{iChannel_1} &= f^b(f^{C_{i+1}}(f^{M_{i+1}}(x), W^{i+1}, b^{i+1})) \\
O_{iChannel_2} &= f^b(f^{C_{i+3}}(f^b(f^{C_{i+2}}(x, W^{i+2}, b^{i+2})), W^{i+3}, b^{i+3})) \\
O_{iChannel_3} &= f^b(f^{C_{i+6}}(f^{C_{i+5}}(f^b(f^{C_{i+4}}(x, W^{i+4}, b^{i+4})), W^{i+5}, b^{i+5}), W^{i+6}, b^{i+6})) \\
O_{iChannel_4} &= f^b(f^{C_{i+10}}(f^{C_{i+9}}(f^{C_{i+8}}(f^b(f^{C_{i+7}}(x, W^{i+7}, b^{i+7})), \\
&\quad W^{i+8}, b^{i+8}), W^{i+9}, b^{i+9}), W^{i+10}, b^{i+10})) \\
O_{iChannel_5} &= f^b(f^{C_{i+15}}(f^{C_{i+14}}(f^{C_{i+13}}(f^{C_{i+12}}(f^b(f^{C_{i+11}}(x, \\
&\quad W^{i+11}, b^{i+11}))), W^{i+12}, b^{i+12}), W^{i+13}, \\
&\quad b^{i+13}), W^{i+14}, b^{i+14}), W^{i+15}, b^{i+15})) \\
O_{iConcat} &= O_{iChannel_1} \odot O_{iChannel_2} \odot O_{iChannel_3} \odot O_{iChannel_4} \odot O_{iChannel_5} \\
\text{i-Block}(x) &= f^b(f^{C_{i+5}}(O_{iConcat}, W^{i+15}, b^{i+15})) \oplus x
\end{aligned}$$

where \oplus represents the layer addition operation.

- **r-Block:** The r-Block reduces computational complexity by decreasing spatial dimensions while preserving important features. It consists of three channels: one with max-pooling, one with 3 kernel-size convolution layer, and the last channel with three convolution layers aimed at capturing spatial features of size 5. The last layers in every channel operate on kernels with 2 strides. All convolution layers in these three channels have 32 kernels. The outputs of these channels are concatenated and passed through another convolution layer with a variable size to match the network's dimensionality. The following expression represents an r-block.

$$\begin{aligned}
O_{rChannel_1} &= f^{M_{i+1}}(x) \\
O_{rChannel_2} &= f^{C_{i+1}}(x) \\
O_{rChannel_3} &= f^{C_{i+4}}(f^{C_{i+3}}(f^{C_{i+2}}(x, W^{i+2}, b^{i+2}), W^{i+3}, b^{i+3}), W^{i+4}, b^{i+4}) \\
O_{rConcat} &= O_{rChannel_1} \odot O_{rChannel_2} \odot O_{rChannel_3} \\
\text{r-Block}(x) &= f^b(f^{C_{i+5}}(O_{rConcat}, W^{i+5}, b^{i+5}))
\end{aligned}$$

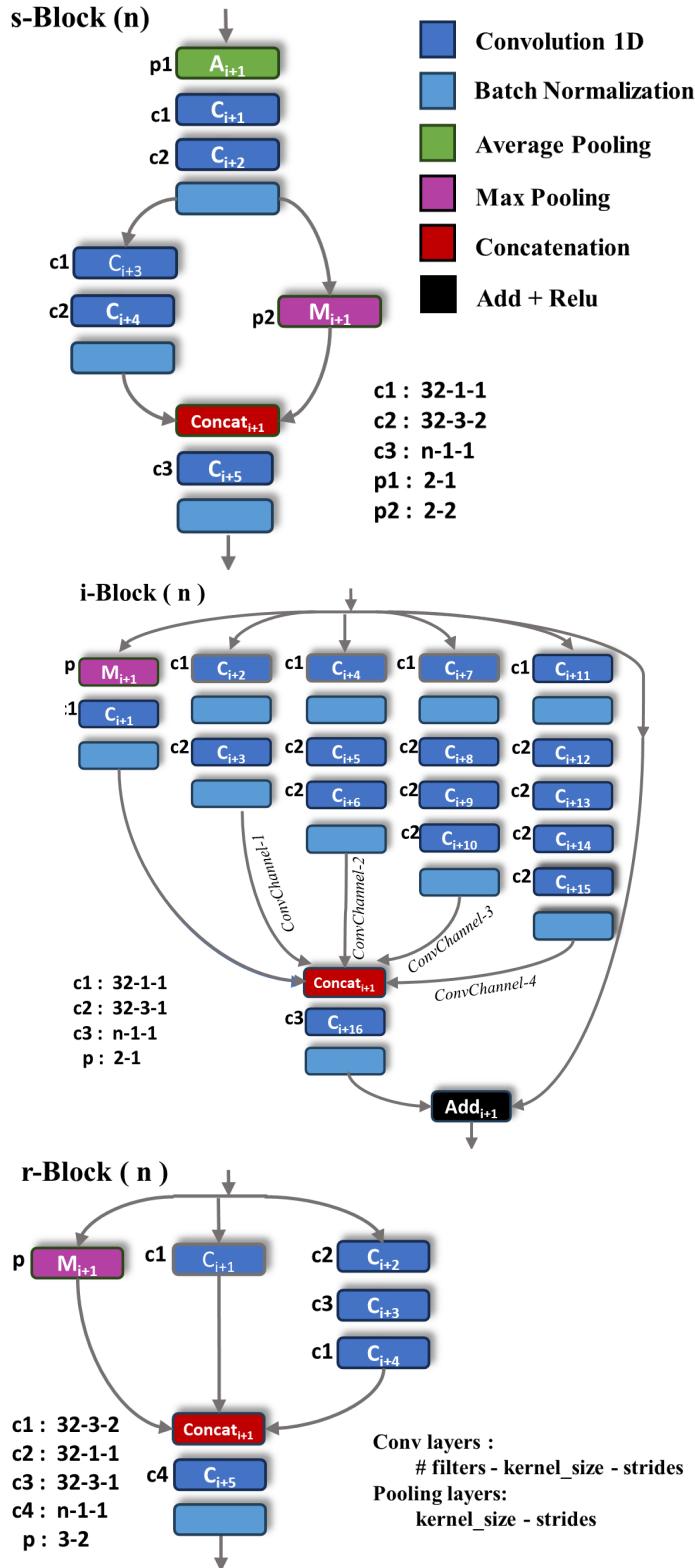


Figure 6.3: Designs of s-Block, i-Block (with #ConvChannels=4) and r-block of MICAnet with layer specifications. To ensure uniqueness, each layer in the blocks is associated with an index, where i represents the number of layers preceding the block.

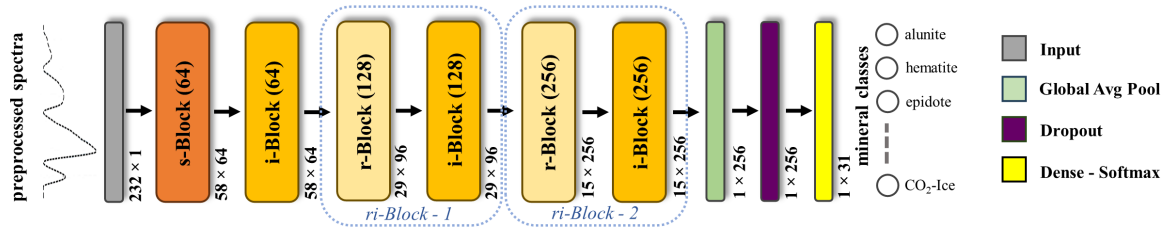


Figure 6.4: The architecture of MICANet with the output shapes of the layers and blocks

6.2.1 Experimental Setup

The experiments are conducted on a Windows 10 laptop equipped with an Intel Core i5-9300H CPU running at 2.40 GHz, 8 GB of RAM, and an NVIDIA GeForce GTX 1650 GPU with 4.0 GB of dedicated memory. The system was configured with the CUDA version 10.0.130 Toolkit and CuDNN version 7.6.5 to leverage GPU acceleration. Coding is done in Python 3.8 with TensorFlow 2.9.0 package Abadi et al. (2015).

The complete MICANet architecture consists of several layers arranged in a specific order. It starts with an input layer, followed by an s-Block and an i-Block. This is followed by a few repetitions of consecutive r-block and i-block combinations, which are termed as '*ri-Block*'s in this paper. The ri-block sequences efficiently extract local to global spatial information while minimizing computational complexity. Similar to the InceptionResNet-v1 model the output shapes of the i-Blocks are increased towards the bottom and the same is adjusted accordingly for the r-Blocks also. Next, there is a global-average-pooling layer to reduce the number of trainable parameters. A dropout layer with a drop-rate of 0.5 is then added to prevent overfitting. Finally, a dense layer with softmax activation is included to capture the class probabilities. Throughout the network, convolution layers use the ReLU activation function. In this study, the hyperparameters of the model were fine-tuned by multiple trials. After experimenting with various optimization algorithms, it was determined that the architecture achieved the best performance on both the train and test datasets when trained with the Adam Optimizer with 1×10^{-5} initial learning rate, for 100 epochs on 15 batch-size. To prevent overfitting, an early stopping was applied on the validation loss with a patience of 20. Table 6.1 provides an overview of the hyperparameters and specifications of the model.

An ablation study was conducted to determine the optimal configuration for the MICANet architecture. The study focused on two key aspects: fixing the number

Table 6.1: Hyper-parameters and training specifications for MICAnet

Optimizer	Adam, initial learning rate: 1×10^{-5}			
Activation Function	Output layer (dense): SoftMax, Other layers (1D convolution): ReLU			
Loss Function	categorical cross-entropy			
epochs	batch-size	earlyStop monitor	earlyStop patience	checkpoint monitor
100	15	val_loss	20	val_loss

Table 6.2: Ablation study of the proposed architecture

#ri-Blocks	#ConvChannels=3		#ConvChannels=4		#ConvChannels=5	
	FLOPs	OA	FLOPs	OA	FLOPs	OA
1	5.96M	78.14%	7.88M	80.09%	10.2M	83.95%
2	11.1M	83.50%	14.2M	86.45%	17.9M	86.0%
3	16.0M	84.32%	20.0M	85.82%	24.6M	86.23%
4	21.9M	85.68%	26.6M	80.59%	32.0M	82.55%

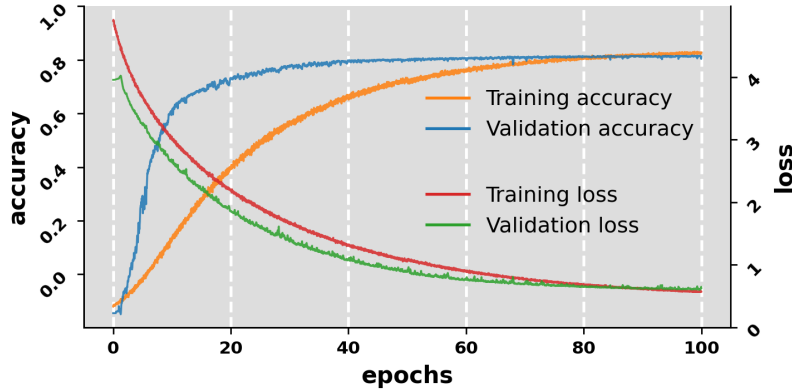


Figure 6.5: Training and validation accuracy-loss plots of MICAnet through the training process

of ConvChannels in the i-Blocks and finding the optimal number of ri-Blocks in the network. These factors directly influenced the model’s size in terms of FLOPs (floating-point operations) and trainable parameters. The results of the experiments, as shown in Table 6.2, revealed that the overall accuracy (OA) for identifying mineral classes in the test data varied with different numbers of ConvChannels and ri-Blocks. For each of the experimental architectures, the trained model with the lowest validation loss in the training process was considered for testing. Increasing the number of ri-Blocks initially improved the OA until reaching a threshold (2 or 3 blocks), after which it started to decline. On the other hand, increasing the number of ConvChannels led to a rapid increase in OA, particularly up to 4 channels in most cases. However, the subsequent increase in ConvChannels had minimal impact on OA. Considering the

trade-off between model size and accuracy, the MICAnet architecture was set with 4 ConvChannels in the i-Blocks and 2 ri-Blocks. This configuration achieved a balance between model complexity and effective accuracy. The complete structure of MICAnet can be seen in figure 6.4, while figure 6.5 presents the accuracy-loss plot of its training, confirming the good fit of the model.

6.2.2 Overall Architecture

MICAnet, as depicted in figure 6.4, in total has 86 layers, including 45 convolution layers, 25 batch normalization layers, 5 concatenation layers, 4 max-pooling layers, and 2 add layers. Additionally, there is one each of input, average pooling, global-average-pooling, dropout, and dense layers. The number of kernels in specific convolution layers of the blocks is determined by the input dimensions of the blocks, as shown in figure 6.4, the output shapes of each layer/block are also provided for convenience. The model has a total of 14.2 million FLOPs, with approximately 0.173 million trainable parameters and 2.43 thousand non-trainable parameters.

6.3 Performance Analysis

The performance of the proposed MICAnet model is evaluated based on its match with the dataset presented by Plebani et al. Plebani et al. (2022), as discussed in section-6.1. Figure 6.6 presents the confusion matrices and ROC curves for different mineral classes and mineral groups. The class confusion matrix shows that while most minerals within a group are correctly identified, there are a few minerals within certain groups that exhibit lower accuracy. Upon analyzing the group confusion matrix, it becomes apparent that despite some mineral classes not being classified with high effectiveness, they are consistently recognized as alternative mineral classes within their corresponding groups, for example, Fe/Ca Carbonate and Mg-Smectite are often labelled as Mg-Carbonate (Carbonate group) and Chlorite (Phyllosilicate group) respectively. However, the group confusion matrix demonstrates high accuracies across the mineral groups, with the lowest being 0.76 for the Carbonate group. This indicates that even if some mineral classes are not classified effectively, they are still identified as other mineral classes within their respective groups. From these results, we can

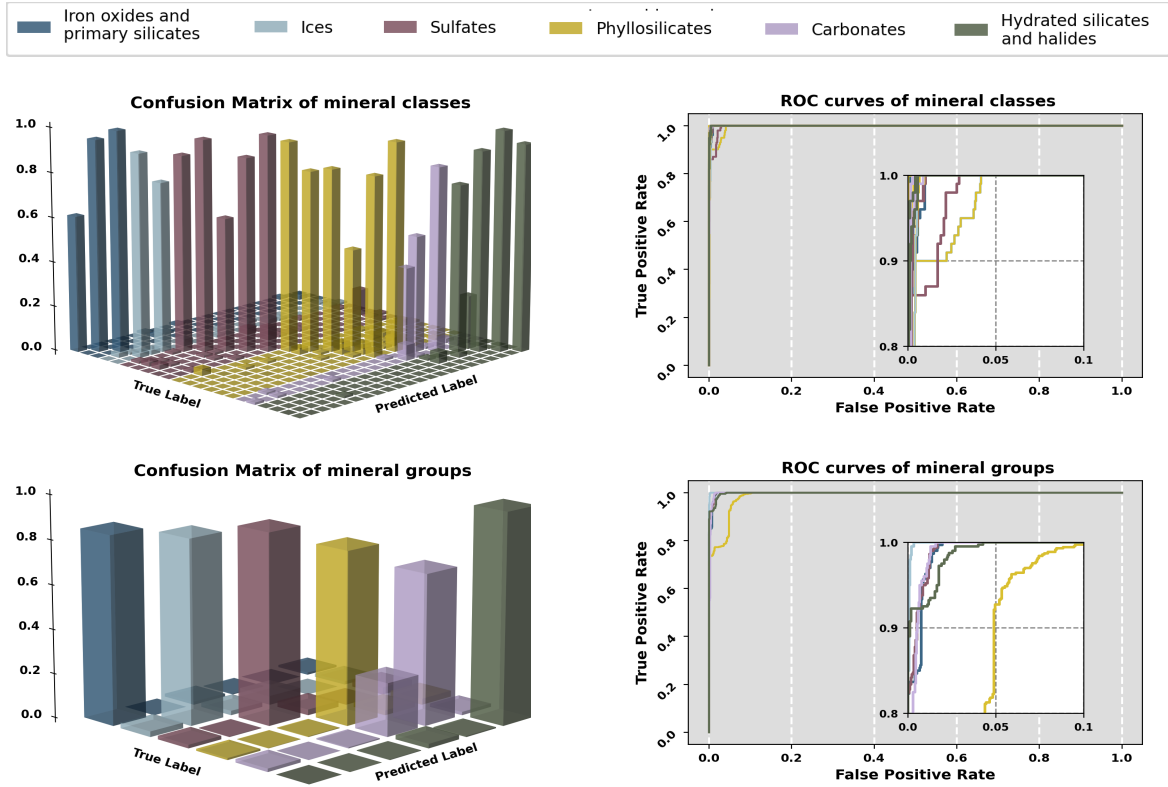


Figure 6.6: Confusion Matrix and ROC curves for different mineral classes and groups

Table 6.3: group wise Mean Accuracy comparison

Mineral Group	MICAnet	SCF - FE - ANN (chapter 5)	SCF - CNN in (chapter 5)
Sulfates	0.874	0.887	0.915
Phyllosilicates	0.936	0.912	0.927
Hydrated silicates	0.890	0.817	0.913
Ices	0.983	0.962	0.901
Carbonates	0.791	0.745	0.810
Primary silicates	0.903	0.832	0.869

conclude that the MICAnet architecture demonstrates a greater ability to learn the collective absorption features of a mineral group, which encompasses the combined absorption signatures of their constituent elements, rather than solely focusing on the individual signatures of each element.

In MICAnet, a test spectrum is evaluated using categorical cross-entropy as the loss and softmax activation function at the final layer. This yields probabilities for each available class. For mineral groups, the probabilities of all minerals within a group are summed to obtain the probability of the test spectrum belonging to that group. The ROC curves for the test mineral classes are generated using an one-vs-others approach, where the probability values of true predictions serve as thresholds.

The ROC curves presented in figure 6.6 shows similar characteristics as the confusion matrices in most cases, while providing a few more insights about the test dataset and the model. Some phyllosilicate minerals show lower accuracy in the class confusion matrix, but their high area-under-the-curve (AUC) values in the ROC curves suggest that some test samples were misclassified even with low similarity to the wrong class. This indicates either the absorption signatures of those true classes are very similar to a few other classes, or the preprocessing pipeline did not sufficiently enhance the signatures of those test samples for accurate classification.

MICAnet's performance is compared with the models described in chapter 4 and 5 in Table 6.3, where the mean accuracies are computed for successful mineral-group classification, which are calculated across multiple runs using different test sample sets. The overall performance of MICAnet is similar or slightly improved compared to these previously employed methods.

6.4 Chapter Summary

- **Designing a 1-D DCNN architecture, MICAnet:** MICAnet, a 1-Dimensional DCNN architecture, inspired from the Inception-v3 and InceptionResnet-v1 architectures, is designed. This specialized design enables in detecting the absorption patterns within spectra data more accurately.
- **Impressive Performance Metrics:** This lightweight architecture exhibits considerably good performance, achieving a minimum accuracy of 0.79. This score was obtained when evaluating different mineral groups in the MICA library using the test data used in this research. MICAnet outperforms the previously utilized sequential neural network model, as well as SVC and RFC.
- **Efficiency and Stability:** The model's efficiency and stability are affirmed through high Area-Under-the-Curve (AUC) values in the ROC curve. These values are consistent across various minerals and individual mineral types, underscoring the reliability and effectiveness of MICAnet.

Chapter 7

Conclusion and Future Perspectives

This research explores a comprehensive framework for accurate mineral identification on Martian surface, integrating a supervised learning model trained with augmented data from the MICA spectral library. A comprehensive preprocessing pipeline, featuring innovative feature extraction compatible with advanced models, ensures robustness in diverse Martian regions. Rigorous uncertainty analysis validates each step's necessity, affirming their essential role. The proposed continuum removal method Segmented Curve-Fitting outperforms the traditional methods in absorption feature detection. Furthermore, MICAnet, a specialized 1-Dimensional DCNN architecture is proposed, that achieves high accuracy and stability across diverse mineral groups and classes, showcasing its effectiveness in mineral identification on Martian surfaces. In this chapter the key findings of this research are summarized along with providing some concluding remarks. Additionally, some perspectives to extend this research are outlined.

7.1 Conclusion

The research finds that, overcoming the challenge of insufficient ground truth data for Martian mineral identification is feasible through augmented datasets created by augmenting mineral spectra from various spectral libraries. The key absorption features should be preserved while adding adequate variability. This approach significantly improves the effectiveness of supervised learning models for mineral identification using CRISM hyperspectral data.

The study highlights the importance of preprocessing steps for both training and testing data to address the persistent noise in CRISM MTRDR data, even after noise correction. These preprocessing steps are essential for enhancing the performance of mineral identification frameworks in the presence of noisy data.

The research identifies that objective-specific preprocessing techniques, such as SCF for continuum removal in the objective of mineral identification, significantly contribute to enhance the performance. SCF, by detecting a greater number of absorption features distinctly, improves the identification process, emphasizing the importance of tailored feature extraction steps.

The research also directs that employing a deep convolutional neural net architecture based on Inception-v3 and InceptionResnet-v1 enhances the framework's performance. This indicates that leveraging powerful learning models capable of accurately recognizing spectral signatures significantly boosts the efficiency and accuracy of mineral identification processes, showcasing the potential of advanced neural network architectures in this context.

7.2 Contributions of the thesis

- **Robust Automated Framework for Mineral Identification on Martian Surface:** The research contributes a robust automated framework that addresses the lack of such systems in mineral identification on Mars. By combining a supervised learning model with meticulous preprocessing techniques, the framework ensures accurate and efficient mineral identification, fulfilling the research gap related to the absence of an automated system in this domain.
- **Innovative Augmentation Approach:** The introduction of an innovative augmentation approach, utilizing spectra from the MICA spectral library, fills the gap due to the scarcity of training data. This method enriches the training dataset, enabling the model to learn from augmented data, compensating for the limited ground-truth information and manual labour for data-collection, and enhancing the framework's accuracy and reliability in mineral identification tasks.
- **Effective Preprocessing Techniques:** The research proposes a few effective preprocessing techniques, including a novel feature extraction method based on the

features of absorptions present in the spectra and the continuum removal method, Segmented Curve Fitting (SCF). These techniques effectively tackle the complexities inherent in CRISM data, filling the gap related to data intricacies. The SCF method, in particular, outperforms traditional continuum removal approaches, ensuring more precise spectral analysis and mineral identification.

- **Specialized Deep Learning Architecture (MICAnet):** The development and implementation of MICAnet, a specialized 1-Dimensional DCNN architecture, inspired by the advanced DCNN architectures like Inception-v3 and InceptionResnetv1, which excels in accurately detecting absorption patterns within spectra data. This innovation addresses the research gap related to the absence of sophisticated models, significantly enhancing the accuracy and stability of mineral identification processes on Martian surfaces.

7.3 Future Extension of the Research

The future extensions of this research are diverse and promising. Each of the aspects explored in this study presents avenues for individual research, aiming to enhance overall performance. Firstly, the augmentation method itself can be further refined. While this study imposed variability to the pure spectra in the library, the real-life data is far more complex, featuring unpredictability and mixed material signatures within the pixel-level of the hyperspectral images. These nuances were not explicitly addressed in the augmentation process. Considering the upcoming NASA 2020 mission on Mars, which aims to bring back a large quantity of rocks and materials from the Martian surface, incorporating these material spectra into the augmentation process could significantly enhance its robustness.

Furthermore, future research could delve into each preprocessing step within the pipeline individually. One significant challenge lies in smoothing the spuriousness of CRISM hyperspectral data while preserving the local maxima, minima, and small absorption features. Also the proposed continuum removal method, SCF, can be extended and explored from various angles. For instance, condition-based selected points for curve fitting and applying the process iteratively could enhance its effectiveness. Another area of research could focus on the limitations of SCF, particularly concerning

the detection of broad bands. Addressing this limitation becomes crucial, especially when dealing with mixed spectra, to accurately identify distinct endmembers in data of this much spectral resolution. Additionally, the feature extraction technique described in Chapter 4 presents an opportunity for extension, aiming for a higher degree of generalization and adaptability to diverse datasets.

Future research endeavors could explore the adaptation and extension of the proposed DCNN architecture, MICAnet, to analyze hyperspectral data from other planetary bodies, such as the Moon, asteroids, or the moons of other planets. This would involve leveraging spectral libraries or ground-truth data specific to the target celestial body to create augmented training datasets, employing transfer learning techniques, and investigating architectural modifications to capture the unique spectral complexities and mineral compositions prevalent on those surfaces.

Additionally, the third avenue for extending this work involves exploring different models for classifying the data. Various models like Recurrent Neural Network (RNN), Graph Neural Network (GNN), and Vision Transformer-based models have demonstrated remarkable success in classification tasks across different application domains. Assessing the framework's performance by integrating these advanced models can be crucial. Furthermore, it's worth noting that in this study, classification is conducted at the spectral level. In contrast, researchers working with hyperspectral data of the Earth's surface have successfully employed similar classifiers at the image level. Extending this approach to CRISM data could be explored.

I express my heartfelt gratitude for your time and interest in this thesis. Your engagement with the research presented here is deeply appreciated. The exploration of Mars and the unraveling of its mysteries remain an ongoing endeavor, and I am humbled by the opportunity to contribute to this collective pursuit of scientific discovery. I sincerely hope that the findings, methodologies, and insights shared within these pages will contribute to the collective pursuit of scientific knowledge and inspire future explorations into the mysteries of the Martian realm.

Bibliography

- Abadi, M., Agarwal, A., Barham, P., Brevdo, E., Chen, Z., Citro, C., Corrado, G. S., Davis, A., Dean, J., Devin, M., Ghemawat, S., Goodfellow, I., Harp, A., Irving, G., Isard, M., Jia, Y., Jozefowicz, R., Kaiser, L., Kudlur, M., Levenberg, J., Mané, D., Monga, R., Moore, S., Murray, D., Olah, C., Schuster, M., Shlens, J., Steiner, B., Sutskever, I., Talwar, K., Tucker, P., Vanhoucke, V., Vasudevan, V., Viégas, F., Vinyals, O., Warden, P., Wattenberg, M., Wicke, M., Yu, Y., and Zheng, X. (2015). TensorFlow: Large-scale machine learning on heterogeneous systems. Software available from tensorflow.org.
- Adams, J. B. (1974). Visible and near-infrared diffuse reflectance spectra of pyroxenes as applied to remote sensing of solid objects in the solar system. *Journal of Geophysical Research*, 79(32):4829–4836.
- Alhayani, B. and Ilhan, H. (2017). Hyper spectral image classification using dimensionality reduction techniques. *International Journal of Innovative Research in Electrical, Electronics, Instrumentation and Control Engineering*, 5(4):71–74.
- Allenby, G. M. and Rossi, P. E. (2006). Hierarchical bayes models. *The handbook of marketing research: Uses, misuses, and future advances*, pages 418–440.
- Allender, E. and Stepinski, T. F. (2017a). Automatic, exploratory mineralogical mapping of crism imagery using summary product signatures. *Icarus*, 281:151–161.
- Allender, E. and Stepinski, T. F. (2017b). Automatic, exploratory mineralogical mapping of crism imagery using summary product signatures. *Icarus*, 281:151–161.
- Amador, E. S., Bandfield, J. L., and Thomas, N. H. (2018). A search for minerals associated with serpentinization across mars using crism spectral data. *Icarus*, 311:113–134.
- Ankerst, M., Breunig, M. M., Kriegel, H.-P., and Sander, J. (1999). Optics: Ordering points to identify the clustering structure. *ACM Sigmod record*, 28(2):49–60.

- Atkinson, P. M., Pardo-Iguzquiza, E., and Chica-Olmo, M. (2008). Downscaling cokriging for super-resolution mapping of continua in remotely sensed images. *IEEE Transactions on Geoscience and Remote Sensing*, 46(2):573–580.
- Boesche, N. K., Rogass, C., Lubitz, C., Brell, M., Herrmann, S., Mielke, C., Tonn, S., Appelt, O., Altenberger, U., and Kaufmann, H. (2015). Hyperspectral rare (rare earth element) mapping of outcrops—applications for neodymium detection. *Remote Sensing*, 7(5):5160–5186.
- Brown, A. (2006). Spectral curve fitting for automatic hyperspectral data analysis. *IEEE Transactions on Geoscience and Remote Sensing*, 44(6):1601–1608.
- Bue, B. D. (2014). An evaluation of low-rank mahalanobis metric learning techniques for hyperspectral image classification. *IEEE Journal of Selected Topics in Applied Earth Observations and Remote Sensing*, 7(4):1079–1088.
- Bue, B. D., Thompson, D. R., Gilmore, M. S., and Castano, R. (2011a). Metric learning for hyperspectral image segmentation. In *2011 3rd Workshop on Hyperspectral Image and Signal Processing: Evolution in Remote Sensing (WHISPERS)*, pages 1–4. IEEE.
- Bue, B. D., Thompson, D. R., Gilmore, M. S., and Castano, R. (2011b). Metric learning for hyperspectral image segmentation. In *2011 3rd Workshop on Hyperspectral Image and Signal Processing: Evolution in Remote Sensing (WHISPERS)*, pages 1–4. IEEE.
- Burns, R. G. (1993). Rates and mechanisms of chemical weathering of ferromagnesian silicate minerals on mars. *Geochimica et Cosmochimica Acta*, 57(19):4555–4574.
- Caggiano, J., Sessa, A., Wray, J., and Paty, C. (2019). Application of machine learning to identify surface minerals in crism imagery. *Lunar Planet. Sci.*, 50.
- Calvin, W. M. and King, T. V. (1997). Spectral characteristics of iron-bearing phyllosilicates: Comparison to orgueil (ci1), murchison and murray (cm2). *Meteoritics & Planetary Science*, 32(5):693–701.
- Carlé M. Pieters¹, . (2004). Relab library citation. <https://www.planetary.brown.edu/relab/>.
- Carter, J., Poulet, F., Bibring, J.-P., Mangold, N., and Murchie, S. (2013a). Hydrous minerals on mars as seen by the crism and omega imaging spectrometers: Updated global view. *Journal of Geophysical Research: Planets*, 118(4):831–858.

- Carter, J., Poulet, F., Murchie, S., and Bibring, J. (2013b). Automated processing of planetary hyperspectral datasets for the extraction of weak mineral signatures and applications to crism observations of hydrated silicates on mars. *Planetary and Space Science*, 76:53–67.
- Carter, J., Poulet, F., Murchie, S., and Bibring, J. (2013c). Automated processing of planetary hyperspectral datasets for the extraction of weak mineral signatures and applications to crism observations of hydrated silicates on mars. *Planetary and Space Science*, 76:53–67.
- Chabrilat, S., Goetz, A. F., Krosley, L., and Olsen, H. W. (2002). Use of hyperspectral images in the identification and mapping of expansive clay soils and the role of spatial resolution. *Remote sensing of Environment*, 82(2-3):431–445.
- Chaves, L., Horgan, B., Lynch, K., Kimbrough, L., Hanley, J., and Wray, J. (2018). Acidic environments in columbus crater, mars: Implications for habitability. In *49th Annual Lunar and Planetary Science Conference*, number 2083, page 1744.
- Clark, R. N. and King, T. V. (1987). Automatic continuum analysis of reflectance spectra. In *JPL proceedings of the 3rd airborne imaging spectrometer data analysis workshop*.
- Clark, R. N. and Lucey, P. G. (1984). Spectral properties of ice-particulate mixtures and implications for remote sensing: 1. intimate mixtures. *Journal of Geophysical Research: Solid Earth*, 89(B7):6341–6348.
- Clark, R. N. and Roush, T. L. (1984a). Reflectance spectroscopy: Quantitative analysis techniques for remote sensing applications. *Journal of Geophysical Research: Solid Earth*, 89(B7):6329–6340.
- Clark, R. N. and Roush, T. L. (1984b). Reflectance spectroscopy: Quantitative analysis techniques for remote sensing applications. *Journal of Geophysical Research: Solid Earth*, 89(B7):6329–6340.
- Clark, R. N., Swayze, G. A., Livo, K. E., Kokaly, R. F., Sutley, S. J., Dalton, J. B., McDougal, R. R., and Gent, C. A. (2003). Imaging spectroscopy: Earth and planetary remote sensing with the usgs tetracorder and expert systems. *Journal of Geophysical Research: Planets*, 108(E12).
- Clenet, H., Pinet, P., Ceuleneer, G., Daydou, Y., Heuripeau, F., Rosemberg, C., Bibring, J.-P., Bellucci, G., Altieri, F., and Gondet, B. (2013). A systematic mapping procedure based on the modified gaussian model to characterize magmatic units from

- olivine/pyroxenes mixtures: Application to the syrtis major volcanic shield on mars. *Journal of Geophysical Research: Planets*, 118(8):1632–1655.
- Craig, M., Cloutis, E., Kaletzke, L., McCormack, K., and Stewart, L. (2006). Alteration of hydration absorption features in reflectance spectra of selected sulfates in a low pressure environment: 0.45-4.3 μm . In *37th Annual Lunar and Planetary Science Conference*, page 2112.
- Craig, M., Cloutis, E., Reddy, V., Bailey, D., and Gaffey, M. (2008). The effects of grain size, $10 \mu\text{m}$ -4.75 mm, on the reflectance spectrum of planetary analogs from 0.35-2.5 μm . In *39th Annual Lunar and Planetary Science Conference*, number 1391, page 2082.
- Dalton, J. B., Bove, D. J., Mladinich, C. S., and Rockwell, B. W. (2004). Identification of spectrally similar materials using the usgs tetracorder algorithm: The calcite-epidote-chlorite problem. *Remote Sensing of Environment*, 89(4):455–466.
- Danielsson, P.-E. (1980). Euclidean distance mapping. *Computer Graphics and image processing*, 14(3):227–248.
- de Berg, M., van Kreveld, M., Overmars, M., and Schwarzkopf, O. C. (2000). *Computational Geometry*. Springer Berlin Heidelberg.
- Dundar, M. and Ehlmann, B. L. (2016). Rare jarosite detection in crism imagery by non-parametric bayesian clustering. In *2016 8th Workshop on Hyperspectral Image and Signal Processing: Evolution in Remote Sensing (WHISPERS)*, pages 1–5. IEEE.
- Dundar, M., Li, L., and Rajwa, B. (2013a). Partially-observed models for classifying minerals on mars. In *2013 5th Workshop on Hyperspectral Image and Signal Processing: Evolution in Remote Sensing (WHISPERS)*, pages 1–4. IEEE.
- Dundar, M., Li, L., and Rajwa, B. (2013b). Partially-observed models for classifying minerals on mars. In *2013 5th Workshop on Hyperspectral Image and Signal Processing: Evolution in Remote Sensing (WHISPERS)*, pages 1–4. IEEE.
- Dunn, T. L., McCoy, T. J., Sunshine, J., and McSween Jr, H. Y. (2010). A coordinated spectral, mineralogical, and compositional study of ordinary chondrites. *Icarus*, 208(2):789–797.
- Edwards, C. S. and Ehlmann, B. L. (2015). Carbon sequestration on mars. *Geology*, 43(10):863–866.

- Ehlmann, B., Mustard, J., and Murchie, S. (2009a). Detection of serpentine on mars by mro-crisp and possible relationship with olivine and magnesium carbonate in nili fossae. In *40th Annual Lunar and Planetary Science Conference*, page 1787.
- Ehlmann, B. L., Edwards, C. S., et al. (2014). Mineralogy of the martian surface. *Annual Review of Earth and Planetary Sciences*, 42(1):291–315.
- Ehlmann, B. L. and Mustard, J. F. (2012). An in-situ record of major environmental transitions on early mars at northeast syrtis major. *Geophysical research letters*, 39(11).
- Ehlmann, B. L., Mustard, J. F., Clark, R. N., Swayze, G. A., and Murchie, S. L. (2011). Evidence for low-grade metamorphism, hydrothermal alteration, and diagenesis on mars from phyllosilicate mineral assemblages. *Clays and Clay Minerals*, 59(4):359–377.
- Ehlmann, B. L., Mustard, J. F., Swayze, G. A., Clark, R. N., Bishop, J. L., Poulet, F., Des Marais, D. J., Roach, L. H., Milliken, R. E., Wray, J. J., et al. (2009b). Identification of hydrated silicate minerals on mars using mro-crisp: Geologic context near nili fossae and implications for aqueous alteration. *Journal of Geophysical Research: Planets*, 114(E2).
- Farrand, W. H., Glotch, T. D., Rice Jr, J. W., Hurowitz, J. A., and Swayze, G. A. (2009a). Discovery of jarosite within the mawrth vallis region of mars: Implications for the geologic history of the region. *Icarus*, 204(2):478–488.
- Farrand, W. H., Glotch, T. D., Rice Jr, J. W., Hurowitz, J. A., and Swayze, G. A. (2009b). Discovery of jarosite within the mawrth vallis region of mars: Implications for the geologic history of the region. *Icarus*, 204(2):478–488.
- Fassett, C. I. and Head III, J. W. (2005). Fluvial sedimentary deposits on mars: Ancient deltas in a crater lake in the nili fossae region. *Geophysical Research Letters*, 32(14).
- Ferguson, R., Hare, T., and Laura, J. (2018). Hrsr and mola blended digital elevation model at 200m v2, astrogeology pds annex. *US Geological Survey*.
- Filippi, A. M. and Jensen, J. R. (2007). Effect of continuum removal on hyperspectral coastal vegetation classification using a fuzzy learning vector quantizer. *IEEE Transactions on Geoscience and Remote Sensing*, 45(6):1857–1869.

- Fink, U. and Sill, G. (1982). The infrared spectral properties of frozen volatiles. In *IAU Colloq. 61: Comet Discoveries, Statistics, and Observational Selection*, pages 164–202.
- Fishbaugh, K. E., Poulet, F., Chevrier, V., Langevin, Y., and Bibring, J.-P. (2007). On the origin of gypsum in the mars north polar region. *Journal of Geophysical Research: Planets*, 112(E7).
- Gendrin, A., Mangold, N., Bibring, J.-P., Langevin, Y., Gondet, B., Poulet, F., Bonello, G., Quantin, C., Mustard, J., Arvidson, R., et al. (2005). Sulfates in martian layered terrains: the omega/mars express view. *Science*, 307(5715):1587–1591.
- Glotch, T. D. and Christensen, P. R. (2005). Geologic and mineralogic mapping of aram chaos: Evidence for a water-rich history. *Journal of Geophysical Research: Planets*, 110(E9).
- Glotch, T. D. and Rogers, A. D. (2013). Evidence for magma-carbonate interaction beneath syrtis major, mars. *Journal of Geophysical Research: Planets*, 118(1):126–137.
- Gorry, P. A. (1990). General least-squares smoothing and differentiation by the convolution (savitzky-golay) method. *Analytical Chemistry*, 62(6):570–573.
- Goudge, T. A., Mustard, J. F., Head, J. W., Fassett, C. I., and Wiseman, S. M. (2015a). Assessing the mineralogy of the watershed and fan deposits of the jezero crater paleolake system, mars. *Journal of Geophysical Research: Planets*, 120(4):775–808.
- Goudge, T. A., Mustard, J. F., Head, J. W., Salvatore, M. R., and Wiseman, S. M. (2015b). Integrating crism and tes hyperspectral data to characterize a halloysite-bearing deposit in kashira crater, mars. *Icarus*, 250:165–187.
- Gruninger, J. H., Ratkowski, A. J., and Hoke, M. L. (2004). The sequential maximum angle convex cone (smacc) endmember model. In *Algorithms and technologies for multispectral, hyperspectral, and ultraspectral imagery X*, volume 5425, pages 1–14. SPIE.
- Guo, Y., Yin, X., Zhao, X., Yang, D., and Bai, Y. (2019). Hyperspectral image classification with svm and guided filter. *EURASIP Journal on Wireless Communications and Networking*, 2019(1):1–9.

- Han, D., Liu, Q., and Fan, W. (2018). A new image classification method using cnn transfer learning and web data augmentation. *Expert Systems with Applications*, 95:43–56.
- Hoefen, T. M., Clark, R. N., Bandfield, J. L., Smith, M. D., Pearl, J. C., and Christensen, P. R. (2003). Discovery of olivine in the nili fossae region of mars. *Science*, 302(5645):627–630.
- Imanian, A., Tangestani, M., and Asadi, A. (2019). Investigation of spectral characteristics of carbonate rocks—a case study on posht moleh mount in iran.
- Jain, N. and Chauhan, P. (2016). Elorza crater on mars: identification of phyllosilicate-bearing minerals by mro-cris. In *Multispectral, Hyperspectral, and Ultraspectral Remote Sensing Technology, Techniques and Applications VI*, volume 9880, pages 322–335. SPIE.
- Kruse, F. A., Lefkoff, A., Boardman, J., Heidebrecht, K., Shapiro, A., Barloon, P., and Goetz, A. (1993). The spectral image processing system (sips)—interactive visualization and analysis of imaging spectrometer data. *Remote sensing of environment*, 44(2-3):145–163.
- Kumari, P., Soor, S., Shetty, A., and Koolagudi, S. G. (2023a). A fully-automated framework for mineral identification on martian surface using supervised learning models. *IEEE Access*, 11:13121–13137.
- Kumari, P., Soor, S., Shetty, A., and Koolagudi, S. G. (2023b). Mineral classification on martian surface using crism hyperspectral data: a survey. *Journal of Applied Remote Sensing*, 17(4):041501–041501.
- LeCun, Y., Bengio, Y., and Hinton, G. (2015). Deep learning. *nature*, 521(7553):436–444.
- Lichtenberg, K. A., Arvidson, R. E., Morris, R. V., Murchie, S. L., Bishop, J. L., Fernandez Remolar, D., Glotch, T. D., Noe Dobrea, E., Mustard, J. F., Andrews-Hanna, J., et al. (2010). Stratigraphy of hydrated sulfates in the sedimentary deposits of aram chaos, mars. *Journal of Geophysical Research: Planets*, 115(E6).
- Lin, H., Tarnas, J., Mustard, J., Zhang, X., and Wu, X. (2018). Dynamic aperture target transformation (datt): A novel and valuable method for mineral detection on mars. In *Lunar and Planetary Science Conference*, number 2083, page 1835.

- Malin, M. C., Bell III, J. F., Cantor, B. A., Caplinger, M. A., Calvin, W. M., Clancy, R. T., Edgett, K. S., Edwards, L., Haberle, R. M., James, P. B., et al. (2007). Context camera investigation on board the mars reconnaissance orbiter. *Journal of Geophysical Research: Planets*, 112(E5).
- McCleese, D., Schofield, J., Taylor, F., Calcutt, S., Foote, M., Kass, D., Leovy, C., Paige, D., Read, P., and Zurek, R. (2007). Mars climate sounder: An investigation of thermal and water vapor structure, dust and condensate distributions in the atmosphere, and energy balance of the polar regions. *Journal of Geophysical Research: Planets*, 112(E5).
- McCraig, M. A., Osinski, G. R., Cloutis, E. A., Flemming, R. L., Izawa, M. R., Reddy, V., Fieber-Beyer, S. K., Pompilio, L., van der Meer, F., Berger, J. A., et al. (2017). Fitting the curve in excel®: Systematic curve fitting of laboratory and remotely sensed planetary spectra. *Computers & geosciences*, 100:103–114.
- McEwen, A. S., Eliason, E. M., Bergstrom, J. W., Bridges, N. T., Hansen, C. J., Delamere, W. A., Grant, J. A., Gulick, V. C., Herkenhoff, K. E., Keszthelyi, L., et al. (2007). Mars reconnaissance orbiter’s high resolution imaging science experiment (hirise). *Journal of Geophysical Research: Planets*, 112(E5).
- McGuire, P. C., Bishop, J. L., Brown, A. J., Fraeman, A. A., Marzo, G. A., Morgan, M. F., Murchie, S. L., Mustard, J. F., Parente, M., Pelkey, S. M., et al. (2009). An improvement to the volcano-scan algorithm for atmospheric correction of crism and omega spectral data. *Planetary and Space Science*, 57(7):809–815.
- McKeown, N. K., Bishop, J. L., Noe Dobrea, E. Z., Ehlmann, B. L., Parente, M., Mustard, J. F., Murchie, S. L., Swayze, G. A., Bibring, J.-P., and Silver, E. A. (2009). Characterization of phyllosilicates observed in the central mawrth vallis region, mars, their potential formational processes, and implications for past climate. *Journal of Geophysical Research: Planets*, 114(E2).
- McLachlan, G. J. (1999). Mahalanobis distance. *Resonance*, 4(6):20–26.
- Michalski, J. R., Bibring, J.-P., Poulet, F., Loizeau, D., Mangold, N., Dobrea, E. N., Bishop, J. L., Wray, J. J., McKeown, N. K., Parente, M., et al. (2010). The mawrth vallis region of mars: A potential landing site for the mars science laboratory (msl) mission. *Astrobiology*, 10(7):687–703.
- Mielke, C., Boesche, N. K., Rogass, C., Kaufmann, H., and Gauert, C. (2015). New geometric hull continuum removal algorithm for automatic absorption band detection from spectroscopic data. *Remote Sensing Letters*, 6(2):97–105.

- Milliken, R. E. and Mustard, J. F. (2005). Quantifying absolute water content of minerals using near-infrared reflectance spectroscopy. *Journal of Geophysical Research*, 110(E12).
- Morris, R. V., Golden, D., Bell III, J. F., Shelfer, T. D., Scheinost, A. C., Hinman, N. W., Furniss, G., Mertzman, S. A., Bishop, J. L., Ming, D. W., et al. (2000). Mineralogy, composition, and alteration of mars pathfinder rocks and soils: Evidence from multispectral, elemental, and magnetic data on terrestrial analogue, snc meteorite, and pathfinder samples. *Journal of Geophysical Research: Planets*, 105(E1):1757–1817.
- Murchie, S., Arvidson, R., Bedini, P., Beisser, K., Bibring, J.-P., Bishop, J., Boldt, J., Cavender, P., Choo, T., Clancy, R., et al. (2007). Compact reconnaissance imaging spectrometer for mars (crism) on mars reconnaissance orbiter (mro). *Journal of Geophysical Research: Planets*, 112(E5).
- Murchie, S. L., Mustard, J. F., Ehlmann, B. L., Milliken, R. E., Bishop, J. L., McKeown, N. K., Noe Dobrea, E. Z., Seelos, F. P., Buczkowski, D. L., Wiseman, S. M., et al. (2009). A synthesis of martian aqueous mineralogy after 1 mars year of observations from the mars reconnaissance orbiter. *Journal of Geophysical Research: Planets*, 114(E2).
- Mustard, J. F., Murchie, S. L., Pelkey, S., Ehlmann, B., Milliken, R., Grant, J. A., Bibring, J.-P., Poulet, F., Bishop, J., Dobrea, E. N., et al. (2008). Hydrated silicate minerals on mars observed by the mars reconnaissance orbiter crism instrument. *Nature*, 454(7202):305–309.
- Neave, D. A., Black, M., Riley, T. R., Gibson, S. A., Ferrier, G., Wall, F., and Broom-Fendley, S. (2016). On the feasibility of imaging carbonatite-hosted rare earth element deposits using remote sensing. *Economic Geology*, 111(3):641–665.
- Noe Dobrea, E., Bishop, J., McKeown, N., Fu, R., Rossi, C., Michalski, J., Heinlein, C., Hanus, V., Poulet, F., Mustard, R., et al. (2010). Mineralogy and stratigraphy of phyllosilicate-bearing and dark mantling units in the greater mawrth vallis/west arabia terra area: Constraints on geological origin. *Journal of Geophysical Research: Planets*, 115(E7).
- Ojha, V. K., Abraham, A., and Snášel, V. (2017). Metaheuristic design of feedforward neural networks: A review of two decades of research. *Engineering Applications of Artificial Intelligence*, 60:97–116.

- Parente, M., Makarewicz, H. D., and Bishop, J. L. (2011). Decomposition of mineral absorption bands using nonlinear least squares curve fitting: Application to martian meteorites and crism data. *Planetary and Space Science*, 59(5-6):423–442.
- Pedregosa, F., Varoquaux, G., Gramfort, A., Michel, V., Thirion, B., Grisel, O., Blondel, M., Prettenhofer, P., Weiss, R., Dubourg, V., Vanderplas, J., Passos, A., Cournapeau, D., Brucher, M., Perrot, M., and Duchesnay, E. (2011). Scikit-learn: Machine learning in Python. *Journal of Machine Learning Research*, 12:2825–2830.
- Pelkey, S., Mustard, J., Murchie, S., Clancy, R., Wolff, M., Smith, M., Milliken, R., Bibring, J.-P., Gendrin, A., Poulet, F., et al. (2007). Crism multispectral summary products: Parameterizing mineral diversity on mars from reflectance. *Journal of Geophysical Research: Planets*, 112(E8).
- Peretyazhko, T., Ming, D., Rampe, E., Morris, R., and Agresti, D. (2018). Effect of solution ph and chloride concentration on akaganeite precipitation: Implications for akaganeite formation on mars. *Journal of Geophysical Research: Planets*, 123(8):2211–2222.
- Plebani, E., Ehlmann, B. L., Leask, E. K., Fox, V. K., and Dunder, M. M. (2022). A machine learning toolkit for crism image analysis. *Icarus*, 376:114849.
- Reynolds, D. A. et al. (2009). Gaussian mixture models. *Encyclopedia of biometrics*, 741(659-663).
- Rice, M., Cloutis, E., Bell Iii, J., Bish, D., Horgan, B., Mertzman, S., Craig, M., Renaut, R., Gautason, B., and Mountain, B. (2013). Reflectance spectra diversity of silica-rich materials: Sensitivity to environment and implications for detections on mars. *Icarus*, 223(1):499–533.
- Roach, L. H., Mustard, J. F., Swayze, G., Milliken, R. E., Bishop, J. L., Murchie, S. L., and Lichtenberg, K. (2010). Hydrated mineral stratigraphy of ius chasma, valles marineris. *Icarus*, 206(1):253–268.
- Salvatore, M., Goudge, T., Bramble, M., Edwards, C., Bandfield, J., Amador, E., Mustard, J., and Christensen, P. (2018). Bulk mineralogy of the ne syrtis and jezero crater regions of mars derived through thermal infrared spectral analyses. *Icarus*, 301:76–96.
- Saranathan, A. and Parente, M. (2017). Active classification of neutral spectra for crism images. In *48th Annual Lunar and Planetary Science Conference*, number 1964, page 2866.

- Saranathan, A. M. and Parente, M. (2021a). Adversarial feature learning for improved mineral mapping of crism data. *Icarus*, 355:114107.
- Saranathan, A. M. and Parente, M. (2021b). Adversarial feature learning for improved mineral mapping of crism data. *Icarus*, 355:114107.
- Scheller, E. L. and Ehlmann, B. L. (2020). Composition, stratigraphy, and geological history of the noachian basement surrounding the isidis impact basin. *Journal of Geophysical Research: Planets*, 125(7):e2019JE006190.
- Seelos, K. D., Seelos, F. P., Viviano-Beck, C. E., Murchie, S. L., Arvidson, R. E., Ehlmann, B. L., and Fraeman, A. A. (2014). Mineralogy of the msl curiosity landing site in gale crater as observed by mro/crism. *Geophysical Research Letters*, 41(14):4880–4887.
- Sessa, A., Wray, J., and Bishop, J. (2018). Discovery of alunite in candidate exomars landing site, mawrth vallis: Evidence for localized evaporative environments. In *49th Annual Lunar and Planetary Science Conference*, number 2083, page 2983.
- Seu, R., Biccari, D., Cartacci, M., Cicchetti, A., Fuga, O., Giuppi, S., Masdea, A., Noschese, R., Picardi, G., Federico, C., et al. (2007). The shallow radar (sharad) experiment, a subsurface sounding radar for mro. *Memorie della Societa Astronomica Italiana Supplementi*, 11:26.
- Sivasankari, T. and Arivazhagan, S. (2019). An overview of morphological and composition investigation of melas chasma of valles marineris. In *Ninth International Conference on Mars*, volume 2089, page 6145.
- Skok, J., Mustard, J., Tornabene, L., Pan, C., Rogers, D., and Murchie, S. (2012). A spectroscopic analysis of martian crater central peaks: Formation of the ancient crust. *Journal of Geophysical Research: Planets*, 117(E11).
- Smith, D. E., Zuber, M. T., Frey, H. V., Garvin, J. B., Head, J. W., Muhleman, D. O., Pettengill, G. H., Phillips, R. J., Solomon, S. C., Zwally, H. J., et al. (2001). Mars orbiter laser altimeter: Experiment summary after the first year of global mapping of mars. *Journal of Geophysical Research: Planets*, 106(E10):23689–23722.
- Soor, S. (2023a). Continuum removal. <https://github.com/SampritiSoor/continuumRemoval>. [Online].
- Soor, S. (2023b). mineral-mapping in crism data. https://github.com/SampritiSoor/CRISM_mineralMapping. [Online].

- Swayze, G., Ehlmann, B., Milliken, R., Poulet, F., Wray, J., Rye, R., Clark, R., Desborough, G., Crowley, J., Gondet, B., et al. (2008). Discovery of the acid-sulfate mineral alunite in terra sirenum, mars, using mro crism: Possible evidence for acid-saline lacustrine deposits? In *AGU Fall Meeting Abstracts*, volume 2008, pages P44A–04.
- Thompson, D. R., Mandrake, L., Gilmore, M. S., and Castano, R. (2010). Superpixel endmember detection. *IEEE Transactions on Geoscience and Remote Sensing*, 48(11):4023–4033.
- Turin, G. (1960). An introduction to matched filters. *IRE transactions on Information theory*, 6(3):311–329.
- Vaniman, D., Bish, D., Ming, D., Bristow, T., Morris, R., Blake, D., Chipera, S., Morrison, S., Treiman, A., Rampe, E., et al. (2014). Mineralogy of a mudstone at yellowknife bay, gale crater, mars. *science*, 343(6169).
- Viviano, C. E., Moersch, J. E., and McSween, H. Y. (2013). Implications for early hydrothermal environments on mars through the spectral evidence for carbonation and chloritization reactions in the nili fossae region. *Journal of Geophysical Research: Planets*, 118(9):1858–1872.
- Viviano, C. E., Seelos, F. P., Murchie, S. L., Kahn, E. G., Seelos, K. D., Taylor, H. W., Taylor, K., Ehlmann, B. L., Wiseman, S. M., Mustard, J. F., et al. (2014a). Revised crism spectral parameters and summary products based on the currently detected mineral diversity on mars. *Journal of Geophysical Research: Planets*, 119(6):1403–1431.
- Viviano, C. E., Seelos, F. P., Murchie, S. L., Kahn, E. G., Seelos, K. D., Taylor, H. W., Taylor, K., Ehlmann, B. L., Wiseman, S. M., Mustard, J. F., and Morgan, M. F. (2014b). Revised CRISM spectral parameters and summary products based on the currently detected mineral diversity on mars. *Journal of Geophysical Research: Planets*, 119(6):1403–1431.
- Viviano-Beck, C. E., Seelos, F. P., Murchie, S. L., Kahn, E. G., Seelos, K. D., Taylor, H. W., Taylor, K., Ehlmann, B. L., Wiseman, S. M., Mustard, J. F., et al. (2014). Revised crism spectral parameters and summary products based on the currently detected mineral diversity on mars. *Journal of Geophysical Research: Planets*, 119(6):1403–1431.

- Walker, J. C., Hays, P., and Kasting, J. F. (1981). A negative feedback mechanism for the long-term stabilization of earth's surface temperature. *Journal of Geophysical Research: Oceans*, 86(C10):9776–9782.
- Wang, C., Paisley, J., and Blei, D. M. (2011). Online variational inference for the hierarchical dirichlet process. In *Proceedings of the fourteenth international conference on artificial intelligence and statistics*, pages 752–760. JMLR Workshop and Conference Proceedings.
- Weitz, C. M., Dobreá, E. N., and Wray, J. J. (2015). Mixtures of clays and sulfates within deposits in western melas chasma, mars. *Icarus*, 251:291–314.
- Wendt, L., Gross, C., Kneissl, T., Sowe, M., Combe, J.-P., LeDeit, L., McGuire, P. C., and Neukum, G. (2011). Sulfates and iron oxides in ophir chasma, mars, based on omega and crism observations. *Icarus*, 213(1):86–103.
- Winter, M. E. (1999). N-findr: An algorithm for fast autonomous spectral end-member determination in hyperspectral data. In *Imaging Spectrometry V*, volume 3753, pages 266–275. SPIE.
- Wiseman, S., Arvidson, R., Wolff, M., Smith, M., Seelos, F., Morgan, F., Murchie, S., Mustard, J., Morris, R., Humm, D., et al. (2016). Characterization of artifacts introduced by the empirical volcano-scan atmospheric correction commonly applied to crism and omega near-infrared spectra. *Icarus*, 269:111–121.
- Woodcock, C. E. and Strahler, A. H. (1987). The factor of scale in remote sensing. *Remote sensing of Environment*, 21(3):311–332.
- Wray, J., Milliken, R., Dundas, C. M., Swayze, G. A., Andrews-Hanna, J., Baldrige, A., Chojnacki, M., Bishop, J., Ehlmann, B., Murchie, S. L., et al. (2011). Columbus crater and other possible groundwater-fed paleolakes of terra sirenum, mars. *Journal of Geophysical Research: Planets*, 116(E1).
- Wray, J., Milliken, R., Swayze, G., Dundas, C., Bishop, J., Murchie, S., Seelos, F., and Squyres, S. (2009). Columbus crater and other possible paleolakes in terra sirenum, mars. In *40th Annual Lunar and Planetary Science Conference*, page 1896.
- Wray, J. J. (2013). Gale crater: the mars science laboratory/curiosity rover landing site. *International Journal of Astrobiology*, 12(1):25–38.
- Wray, J. J., Hansen, S. T., Dufek, J., Swayze, G. A., Murchie, S. L., Seelos, F. P., Skok, J. R., Irwin, R. P., and Ghiorso, M. S. (2013). Prolonged magmatic activity on mars inferred from the detection of felsic rocks. *Nature Geoscience*, 6(12):1013–1017.

- Wray, J. J., Squyres, S. W., Roach, L. H., Bishop, J. L., Mustard, J. F., and Dobre, E. Z. N. (2010). Identification of the ca-sulfate bassanite in mawrth vallis, mars. *Icarus*, 209(2):416–421.
- Wu, X., Mustard, J., Tarnas, J., Zhang, X., Das, E., and Liu, Y. (2021a). Imaging mars analog minerals’ reflectance spectra and testing mineral detection algorithms. *Icarus*, 369:114644.
- Wu, X., Zhang, X., Mustard, J., Tarnas, J., Lin, H., and Liu, Y. (2021b). Joint hapke model and spatial adaptive sparse representation with iterative background purification for martian serpentine detection. *Remote Sensing*, 13(3):500.
- Xu, B., Wang, N., Chen, T., and Li, M. (2015). Empirical evaluation of rectified activations in convolutional network. *arXiv preprint arXiv:1505.00853*.
- Xue, Y. and Jin, S. (2013). Martian minerals components at gale crater detected by mro crism hyperspectral images. In *2013 2nd International Symposium on Instrumentation and Measurement, Sensor Network and Automation (IMSNA)*, pages 1067–1070. IEEE.
- Xue, Y., Yang, Y., and Yu, L. (2018). Mineral composition of the martian gale and nili fossae regions from mars reconnaissance orbiter crism images. *Planetary and Space Science*, 163:97–105.
- Yanbin, P. and Zhijun, Z. (2020). Hyperspectral image classification based on intelligent optimization feature selection. *International Journal of Research-GRANTHAALAYAH*, 8(4):104–111.
- Yang, Y., Jin, S., and Xue, Y. (2014). Identification of minerals at martian jezero crater using mro crism images. In *2014 XXXIth URSI General Assembly and Scientific Symposium (URSI GASS)*, pages 1–4. IEEE.
- Yerebakan, H. Z., Rajwa, B., and Dundar, M. (2014). The infinite mixture of infinite gaussian mixtures. *Advances in neural information processing systems*, 27.
- Zhang, J., Rivard, B., and Sanchez-Azofeifa, A. (2004). Derivative spectral unmixing of hyperspectral data applied to mixtures of lichen and rock. *IEEE Transactions on Geoscience and Remote Sensing*, 42(9):1934–1940.
- Zhao, H., Zhang, L., Zhang, X., Liu, J., Wu, T., and Wang, S. (2015). Hyperspectral feature extraction based on the reference spectral background removal method. *IEEE Journal of Selected Topics in Applied Earth Observations and Remote Sensing*, 8(6):2832–2844.

List of publications

Journals (Published)

- **P. Kumari**, S. Soor, A. Shetty and S. G. Koolagudi "A Fully-Automated Framework for Mineral Identification on Martian Surface Using Supervised Learning Models" in IEEE Access, vol. 11, pp. 13121-13137, 2023 DOI: 10.1109/ACCESS.2023.32430617
- **P. Kumari**, S. Soor, A. Shetty and S. G. Koolagudi "Mineral Classification on Martian Surface Using CRISM Hyperspectral Data: A Survey" Journal of Applied Remote Sensing, 17(4), 041501–041501, 2023 DOI:10.1117/1.JRS.17.041501

Journals (Under Revision)

- **P. Kumari**, S. Soor, A. Shetty and S. G. Koolagudi "Segmented Curve-Fitting for Continuum Removal in Hyperspectral Images"
- **P. Kumari**, S. Soor, A. Shetty and S. G. Koolagudi "MICAnet: A Deep Convolutional Neural Network for Mineral Identification on Martian Surface"

Priyanka Kumari

🏠 4C-A, symphony Tower, Hansh vihar colony,

Dhanbad, Jharkhand 826001, India

★ 10-06-1990 🇮🇳 Indian

✉️ singh.priyanka854@gmail.com 📞 +91 7488655255

🌐 priyanka-singh-80b278a4

Education

- 2018 – 23 📖 **Ph.D. in Remote Sensing** from *National Institute of Technology, Karnataka*
Thesis title: *Mineral Identification on Martian Surface Using Supervised Learning Approach from CRISM Hyperspectral Data*
- 2013 – 15 📖 **M.Tech. in Remote Sensing** from *Birla Institute of Technology - Mesra*
- 2009 – 13 📖 **B.Tech. in Electrical and Electronics Engineering** from *BPUT*

Skills

- Subjects 📖 Remote Sensing, Image Processing, Hyperspectral and Multispectral imagery, Machine Learning, Minerology
- Coding 📖 Python, C, Matlab
- Software 📖 ArcGIS, QGIS, ENVI, GEE, Erdas.

Achievements

- 2013 📖 **GATE Electrical Engineering** qualified. All India Rank: 5052

Employment History

- 2017 – 18 📖 **Central University of Jharkhand, Ranchi** as Assistant Professor (temp)
- 2016 – 17 📖 **Indian Institute of Technology, Dhanbad** as a Junior Research Fellow
project title: *“Geospatial Fusion of Parameters Controlling Orogenic Gold Mineralization and Delineation of Gold prospective Zones within Chandil Formation, North Singhbhum Mobile belt, Eastern Indian Craton. A Regional Scale Analytical Approach through the Integrated Applications of GIS, GPS and Remote Sensing Technology”*
- 2016 – 16 📖 **Indian Statistical Institute, Bangalore** as a Project Linked Personnel
project title: *“Land Use/Cover Classification of Remote Sensing Images Using Granular Computing Methodologies”*
- 2015 – 16 📖 **Jharkhand Space Application Centre, Ranchi** as a System Engineer

Referees

Amba Shetty 🧑

Professor

WROE, NIT-Karnataka

✉️ amba@nitk.edu.in

Shashidhar G. Koolagudi 🧑

Associate Professor

CSE, NIT-Karnataka

✉️ koolagudi@nitk.edu.in

Research Publications

Journals (Published)

- 1 **Kumari, P.**, Soor, S., Shetty, A., & Koolagudi, S. G. (2023a). A fully-automated framework for mineral identification on martian surface using supervised learning models. *IEEE Access*. [🔗 doi:10.1109/ACCESS.2023.3243061](https://doi.org/10.1109/ACCESS.2023.3243061)
- 2 **Kumari, P.**, Soor, S., Shetty, A., & Koolagudi, S. G. (2023c). Mineral classification on martian surface using crism hyperspectral data: A survey. *Journal of Applied Remote Sensing*, 17(4), 041501–041501. [🔗 doi:10.1117/1.JRS.17.041501](https://doi.org/10.1117/1.JRS.17.041501)

Journals (Under Revision)

- 1 **Kumari, P.**, Soor, S., Shetty, A., & Koolagudi, S. G. (2023b). *Micanet: A deep convolutional neural network for mineral identification on martian surface*.
[🔗 Available here.](#)
- 2 **Kumari, P.**, Soor, S., Shetty, A., & Koolagudi, S. G. (2023d). *Segmented curve-fitting method for continuum removal in hyperspectral images*.
[🔗 Available here.](#)